SCUOLA DI DOTTORATO
UNIVERSITÀ DEGLI STUDI DI MILANO-BICOCCA

Dipartimento di / Department of

Fisica Giuseppe Occhialini

Dottorato di Ricerca in / PhD program Fisica e Astronomia Ciclo / Cycle XXXI

Curriculum in (se presente / if it is) Fisica

Boosting scintillation based detection

Cognome / Surname Salomoni Nome / Name Matteo

Matricola / Registration number 786926

Tutore / Tutor: Paganoni Marco

Cotutore / Co-tutor: Auffray Etiennette
(se presente / if there is one)

Supervisor: (se presente / if there is one)

Coordinatore / Coordinator: Calvi marta

ANNO ACCADEMICO / ACADEMIC YEAR 2017/2018

Università degli studi di
Milano-Bicocca

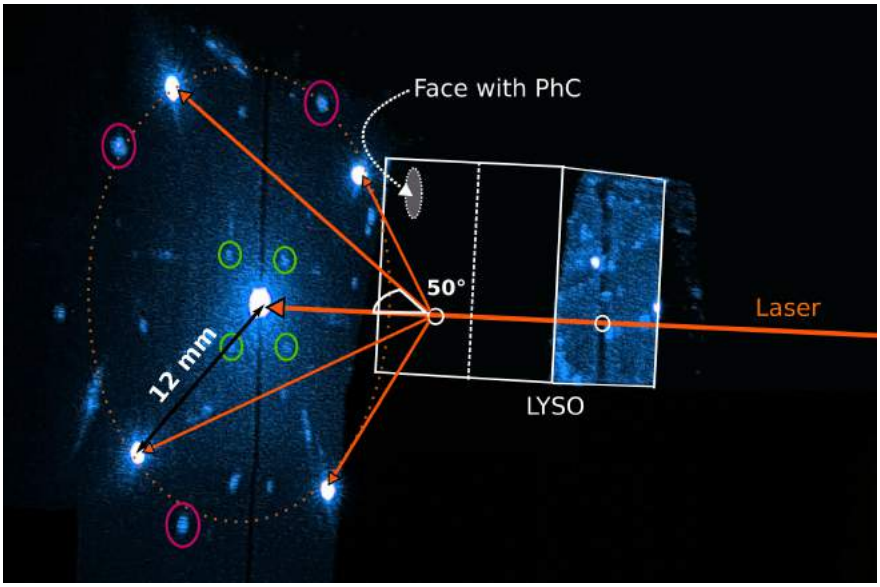

Boosting scintillation based detection

The route towards better timing and energy resolution

PhD's thesis in Physics and Astronomy

MATTEO SALOMONI

Department of Physics Giuseppe Occhialini
UNIVERSITY OF MILANO-BICOCCA
Milano, Italy 2019

PhD thesis 2019

Boosting scintillation based detection

The route towards better timing and energy resolution

MATTEO SALOMONI

Dipartimento Giuseppe Occhialini
Fisica e Astronomia
Crystal Clear Collaboration
University of Milano-Bicocca
Milano, Italia 2019

Boosting scintillation based detection
The route towards better timing and energy resolution
MATTEO SALOMONI

Supervisor: Marco Paganoni, University of Milano-Bicocca

PhD's Thesis 2019
Dipartimento Giuseppe Occhialini
Fisica e Astronomia
Crystal Clear Collaboration
University of Milano-Bicocca

Cover: Photonic crystal diffraction effect: green laser beam impinging from the inside of an LYSO scintillator.

Typeset in LaTeX
Milano, Italy 2019

Keywords: Particle detectors, scintillators, energy resolution, time resolution, photonic crystals, nano-crystals, meta-materials, crystal growth, optical couplings, photo-detectors, simulations, Geant4, CAMFR.

Boosting scintillation based detection
The route towards better timing and energy resolution
MATTEO SALOMONI
Fisica e Astronomia
University of Milano Bicocca

Abstract

During this PhD, state-of-the-art scintillating materials have been intensively studied with several constraints found regarding their light emission, optical properties and chemical stability. Different characterization benches were developed specifically for the measurements presented in the thesis and extensive work has been dedicated to fine tune the simulations framework that describes scintillators and photo-detectors.
Classical approaches were found to be already at a good trade-off between performances and costs while to really boost scintillation detection a shift in paradigm was needed, moving away from classical ray tracing concepts and scintillation mechanism. This PhD work explored the use of diffraction and quantum dots to break the limit of critical angle and classical e-h recombination, respectively.
Photonic crystals were used as diffracting layer deposited on the read-out face of inorganic scintillators and showed promising results from the point of view the crystal's time and energy resolution. The additional modes provided by the periodical nano-structuration of the read-out face add several degrees of freedom where simulations could find new optimal solutions. An enhanced extraction of scintillation light was demonstrated in different crystal configurations.
Nanocrystals, on the other hand, pushed the state-of-the-art of scintillation timing properties down to the ps scale, bringing innovative ideas for future fast detectors. The use of quantum dots allowed to tune the recombination mechanism of scintillating semiconductors leading to inhibited non-radiative channels and enhance dipole emission from the emitting centers.

Mais ce qui me contentait le plus de cette méthode était que,
par elle, j'étais assuré d'user en tout de ma raison,
si non parfaitement, au moins le mieux, qui fut en mon pouvoir;
outre que je sentais, en la pratiquant, que mon esprit s'accoutumait
peu à peu à concevoir plus nettement et plus distinctement ses objets,
et que, ne l'ayant point assujettie à aucune matière particulière,
je me promettais de l'appliquer aussi utilement aux difficultés des autres sciences.

Discourse on the Method, René Descartes.

Acknowledgements

I would first like to thank my thesis tutors Marco Paganoni of the University of Milano-Bicocca and Etiennette Auffray of the European Organization for Nuclear Research (CERN), who gave me the possibility to work in the crystal clear collaboration, starting from my master thesis. I would like to thank the experts who were involved in the *R&D* for the research project followed during this PhD: Radiation Monitoring Device Inc (RMD), Silsef and Napa Technologies and the university of Lyon and Wroclaw for the photonic crystal production, the university of Troyes, Oncovision and the university of Lausanne (CHUV) for the expertise related to the TurboPET project, the engineering department at CERN for their wonderful work with my non conductive samples and the mechanical experts Dominique Deyrail and Sauce Herve Emile, the University of Prague for their halides production, the University of Milano-Bicocca for the support provided during this entire PhD and finally the crystal clear group at CERN, who was always ready to discuss any problem one could encounter. Without the passionate participation and input from all this people I would have not been able to successfully conduct my work during this 3 years Finally, I must express my very profound gratitude to my parents and to my girlfriend: you are my strength, my passion and my determination.
Author
Matteo Salomoni

Matteo Salomoni, Milano, February 2019

Contents

List of Figures

List of Tables

Glossary

Acronyms

PET: Positron Emission Tomography.
FWHM: Full Width Half Maximum.
LY: Light yield.
RI: Refractive index.
PMT: Photomultiplier Tube.
SPECT: Single-Photon Emission Computed Tomography.
HEP: High Energy Physics
HL-LHC: High Luminosity Large Hadron Collider.
TOF-PET: Time Of Flight PET.
SNR: Signal to Noise Ratio.
LOR: Line Of Response.
QE: Quantum Efficiency.
SiPM: Silicon PMT.
SE: Single Electron.
LED: Light emitting diode.
PET: Single-Photon Avalanche Diode.
CTR: Coincidence Time Resolution.
CERN: European Organization for Nuclear Research.
CCD: Charge-Coupled Device.
XRT: X-Ray Tube.
MCP: Micro-Channel Plate.
CMOS: Complementary Metal–Oxide–Semiconductor.
IRF: Instrument Response Function.
PL: Photo-Luminescence.
PDE: Photo-Detection Efficiency.
PhC: Photonic Crystal
TIR: Total Internal Reflection.
EFC: Equi-Frequency Countour.
RCWA: Rigourous Coupled-Wave Analysis.
MCP: CAvity Modeling FRamework.
FDTD: Finite-Difference Time-Domain.
MPB: MIT Photonic Bandgap.

FEM: Finite Element Domain.
TE: Transverse Electric.
TM: Transverse Magnetic.
ALD: Atomic Layer Deposition.
RIE: Reactive Ion Etching.
EUV: Extreme UV.
ADC: Analog to Digital Converter.
PSPMT: Position Sensitive PMT.
WP: Work Package.
NIL: Nano-Imprint Lithography.
SA: Self-Assembly.
GRIN: GRadient INdex matching.
LTE: Light Transport Efficiency.
NC: Nano-Crystal.
NPL: Nano-PLatelet.
QD: Quantum Dot.
GS QD: Giant Shell Quantum Dot.
CM: Carrier Multiplication.
AR: Auger Recombination.

1

Introduction

Radiation is the transmission of energy in the form of moving mass or wave and carries information about fundamental particles dynamics and atomic processes. Extracting this information is of central interest in nowadays science, being that R&D, R&D&I or industrial application. The more precise the information we can extract from this radiating energy or mass, the more we can extrapolate about the process that generated it, the environment condition during its generation and transport losses. If radiation can create ionized atoms, molecules or chemical bonds, it is called ionizing radiation: a local charge will be released in the ionized material and this charge carries information. If the dynamics that created the charge are well understood, the energy associated to each charge generation can be reconstructed, as well as the time on which the interaction happened. This is the working principle of ionizing radiation detector, and many different devices were created trying to precisely determine time of the particle crossing the material and energy deposited during the process.
When the energy of the incident particle is totally absorbed in the detection process, the detector is called calorimeter. This doctoral thesis will focus on inorganic scintillators, that are an example of electromagnetic calorimeter. In the following, an introduction on how inorganic scintillators works will be given, together with a description of the state-of-the-art and how to challenge the limits sets by the current technology.

1.1 Inorganic Scintillators

Inorganic scintillators are transparent dielectric media which emits light (UV-optical) following the energy deposition of ionizing radiation. Inorganic scintillators are usually found in a crystalline structure and show high stopping power for gamma rays, can be reasonably fast and bright and are relatively inexpensive to manufacture. They are nowadays used as detectors in various applications such as high energy physics, medical imaging, homeland security, material research, and thermal neutron detection. The characteristic parameters of inorganic scintillators are density (stopping power), light yield, energy resolution, rise time and decay time, emission wavelength, radiation hardness, and production costs. These parameters can be partially tuned depending on the requirements that the different applications have with regard to one or many of them. Since a perfect scintillator matching all requirements does not exist, a trade-off between various parameters has, in general, to be found to best match the needs of such applications. The performance of scintillators in terms of light yield, energy and time resolution is, however, intrinsically limited by fundamental physical effects as explained in the next sections.

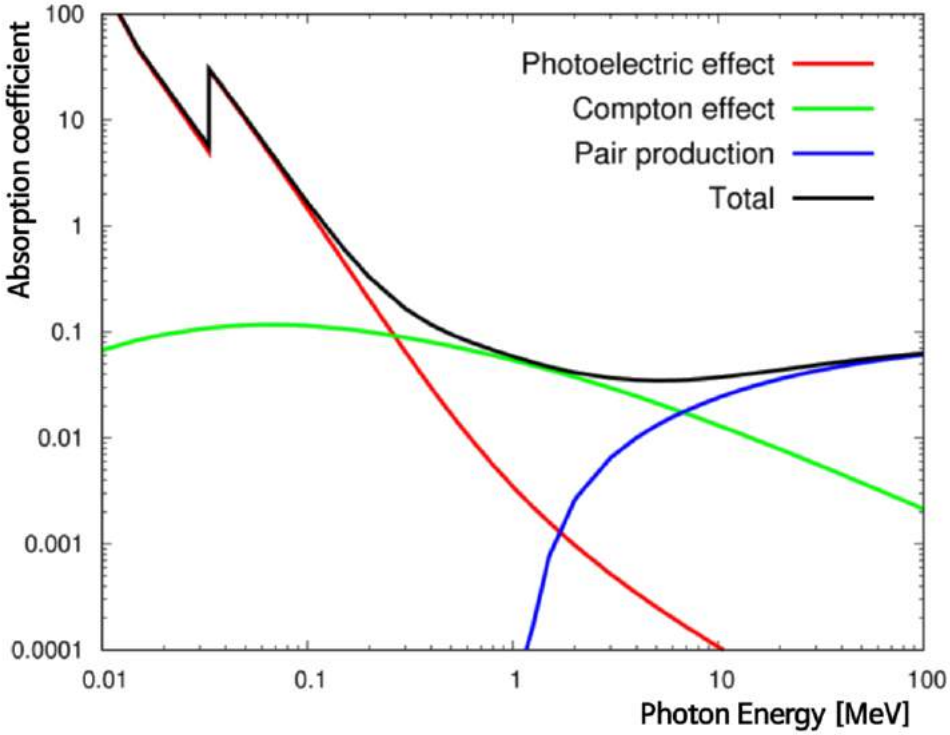

Figure 1.1: γ-ray linear attenuation coefficients.

1.2 Scintillation detection

1.2.1 Scintillator output

Scintillation light pulses analyses provide information needed for energy and time identification of the interaction of ionizing radiation. This thesis aims at boosting time and energy resolution of inorganic scintillators, and an introduction on the basic quantities of scintillation based detection is given in the following.
Let's suppose that the objective is to characterize a scintillator response using a ^{22}Na source. This particular isotope of Sodium decays with β^+ emission on a metastable state of Neon [^{22}Ne*] which then subsequently relax on its stable state with the emission of a γ-ray, with a delay of 3.7 ps compared to the positron emission. As a result, 3 γ-ray will be emitted by the source for each decay: two 511 keV in back to back from the β^+ annihilation and the 1.274 MeV from the excited Neon.
The response of a scintillator detector exposed to this source will be the emission of optical light for each γ-ray interacting with the volume. The probability for a photon interaction depends on the scintillator compound and on the type of interaction. Figure 1.1 shows the 3 different processes probability as a function of the incoming photon energy. For ^{22}Na emission, the 511 keV photons will undergo mostly photoelectric effect, depositing all the energy in one interaction. This is the main reason for choosing a source with this emission energy, since photo-electric effect will generate a clear mark in the spectrum, which carries many information about the scintillation dynamics. The 1.274 photon has energy enough to produce a couple e^+e^-, or to undergo either Compton or photoelectric effect. Couple production will results in another pair of 511 keV annihilation photons and a background of Bremsstrahlung radiation during electron and positron thermalization. Compton effect will deposit only a fraction of the initial photon energy.
Integrating each scintillation pulse coming from the crystal and making a histogram

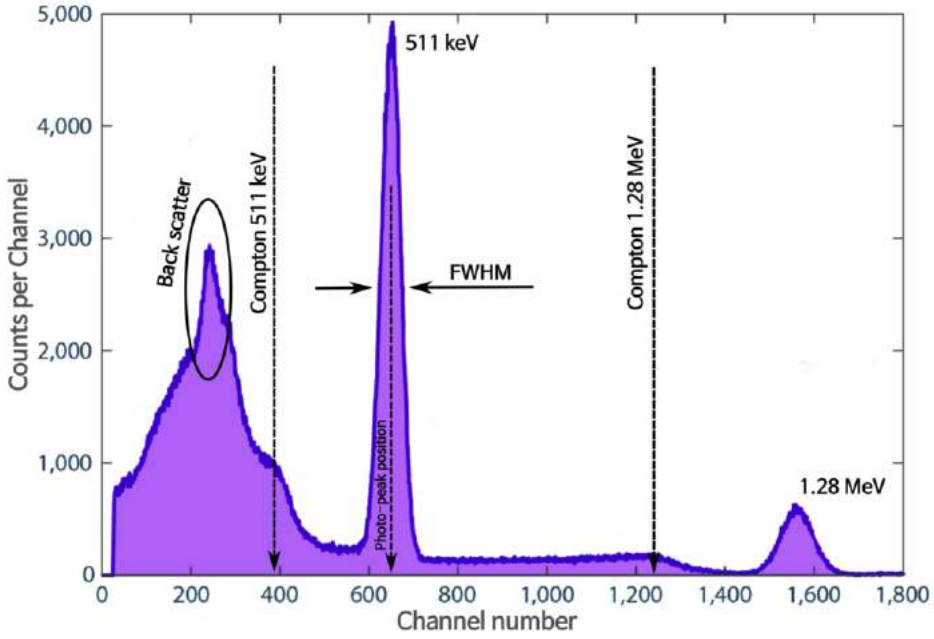

Figure 1.2: Example of non calibrated histogram obtained with a scintillator and ^{22}Na is shown. The photo-peaks position for the γ-rays emitted are shown, as well as the Full Width Half Maximum (FWHM) of the 511 keV photo-peak and the position of the Compton "shoulders" (maximum energy theoretically deposited by Compton effect).

of the values obtained, a plot similar to the one shown in Figure 1.2 is obtained. The photo-peak events are usually Gaussian distributed: the centroid is directly proportional to the incoming γ-ray energy and is used to characterize brightness of the scintillator, classically expressed by the number of optical photons emitted per incident MeV; the Full Width Half Maximum = FWHM = 2.355 x σ_{gauss} represent the energy resolution of the system. More details on the photo-peak spectrum analysis will be presented in section 2.
The back scattering peak is built by contribution from external element, such as metals in the vicinity of the detection chain.

1.2.2 Light yield

The signal-to-noise ratio is an important parameter in all radiation detection devices using scintillators. While the noise remains constant, the strength of the signal depends on the number of photoelectrons generated in the photodetector used to readout the scintillator, which change the photo-peak position described in the previous section. This is proportional to the light yield (LY_{out}), defined as the number of scintillation photons generated per unit of energy deposited by the incoming particle, collected in the photo-cathode and that can be converted into photoelectrons.
This LY_{out} depends on the number of photons N_{Php} produced in the crystal by the incoming particle interaction and the light collection efficiency η_{coll}, which is a measure of all kinds of light losses along its way to the photodetector, such as reflection, absorption and diffusion in the crystal competing with extraction at the exit surface of the crystal.
N_{Php} is determined by the overall conversion efficiency of the energy of the incident particle (gamma or X-ray) to light emission (UV or visible) and given by the

following formula:

$$N_{Php} = \frac{E_i}{\beta E_g} SQ \tag{1.1}$$

with E_i the energy of incident particle, E_g the band gap energy, S the transfer efficiency from ionization to the luminescence center and Q the efficiency of luminescence [1]. β is a parameter varying from 2–3 for a wide range of scintillators [2].
The light collection efficiency η_{coll} depends on the optical properties of the crystal. The generally high refractive index (RI) of the scintillators and the consequently small critical angle will lower this efficiency. Several studies ([3, 4, 5]) demonstrated also that the surface state, the edge quality and the type of wrapping used for the crystal play an important role in the efficiency of light collection η_{coll}.
The light yield of the crystal can, therefore, be expressed by the following equation:

$$LY_{out} = \eta_{coll} \frac{N_{Php}}{E_i} = \eta_{coll} \frac{SQ}{\beta E_g} \tag{1.2}$$

showing that the light yield is governed by the band gap energy, the transfer efficiency from ionization to luminescence and light collection efficiency. The Q factor is usually a constant close to one. It was shown that the optimal energy band gap to obtain high light yield materials varies with the type of activator [6].
Maximizing the light yield not only requires selecting materials with an optimal band gap energy, but also optimizing the transport of the light such that the maximum photons reach the photodetector.

1.2.3 Energy Resolution

The factors impacting the energy resolution of a scintillator-based detector system are in general classified into three different categories:

- Statistical fluctuations in the generation of scintillation photons and the conversion in photoelectrons in the photodetector, expressed by σ_{stat};
- Inhomogeneity in the bulk material (impurities, scattering centers) and the surface of the crystal (polishing, wrapping) leading to fluctuations of the amount of light transported to the photodetector, expressed by σ_{def};
- Non-linearity of the scintillation photon yield as a function of the energy deposited by the incoming particle, due to statistical fluctuations of the ionization process and a non-uniform ionization density, expressed by σ_{np}.

Statistical fluctuations in the generation and detection of scintillation photons can be minimized by maximizing the light yield. The impact of inhomogeneity in the bulk and at the surface of the scintillator can be minimized by improving the purity of the raw material, controlling the crystal growth process parameters, optimizing the surface treatment and choosing appropriate reflector materials. Contributions from the non-linearity in the scintillation photon yield are more challenging to optimize and therefore constitute the main limitation for the optimization of the energy resolution. Extensive R&D has been carried out in the past by several groups [7] to better understand these contributions.
Once the scintillator is part of a detection chain, such as the one presented in section 2, defining $\sigma_{stat} \oplus \sigma_{def} \oplus \sigma_{np} = \delta_{sc}$ as the intrinsic contribution of the crystal, a more general description of energy resolution can be given, considering that for such system is defined by the FWHM of the photo-peak registered and by its position:

$$Eres = FWHM/Pe_{pos} = (2.355 \cdot \sigma_E)/E \tag{1.3}$$

$$\frac{\sigma_E}{E} \propto \delta_{sc} \oplus \frac{\Delta N}{N} \oplus \delta_n \tag{1.4}$$

Where the second term in equation 1.4 is the statistical component, which depends on the Poisson distributed photo-electrons generated (N) at the photo-cathode of the Photomultiplier Tube (PMT), and the third corresponding to contributions external to the crystal, mostly dominated by the noise component related to the acquisition chain.

1.2.4 Time Resolution

The intensity of the scintillation light as a function of time is in general described using a bi-exponential expression:

$$I(t) = I(0)e^{-t/\tau_d}(1 - e^{-t/\tau_r}), \tag{1.5}$$

with τ_r and τ_d being the scintillation rise time and the scintillation decay time, respectively.
In the case of several different luminescence centers, expression (1.5) becomes a sum of exponentials. The decay time of a scintillator is related to the depopulation rate of the excited state: it is the result of radiative (τ_{drad}) and non-radiative (τ_{dnrad}) processes. For electrical dipole emission, the radiative process rate is inversely proportional to the oscillator strength *f*, with a coefficient depending on the coordination of the emitting ions in the crystal lattice. It is typically expressed as:

$$\tau_{drad} = 1.35 \cdot 10^5 \frac{\lambda^2}{f \cdot n(1 + n^2)^2} \tag{1.6}$$

with λ the emission wavelength and nthe refractive index [1]. Therefore, a shorter emission wavelength and a higher index of refraction favor a shorter decay time.
The time resolution of a scintillator-based detection system is a measure for the precision of the time stamp that can be attributed to the detection of a particle. The time resolution depends on the rate of photoelectrons above the detection threshold, which in turn depends on the time distribution of photons being converted in the photodetector. The main crystal parameters influencing the time resolution of a scintillator detector are the light yield and the rise and decay time of the scintillation process as illustrated by the following formula, derived by the Hyman theory:

$$\Delta t \propto \sqrt{\frac{\tau_d \tau_r}{LY_{out}}} \tag{1.7}$$

The time resolution Δt can hence be improved by using scintillators with high light yield and short decay and rise time constants [8, 9].

1.3 Rationale for a boosted scintillator detector

Improving the extraction efficiency and timing properties of the scintillation light from inorganic scintillators remains an important concern for improving the performance of scintillator-based ionization radiation detectors. Indeed, the goal for these detectors is to record the maximum information about the event at the origin of the ionizing radiation, and in particular:

- its spatial localization
- the precise determination of its energy
- the time of the event

If the spatial localization is generally achieved by the choice of a dense material and the combination of a number of individual detectors, finely segmented and distributed around the region of interest, the energy and time resolution are directly

related to the amount of collected light.
The high Z materials used in these detectors, to ensure a high stopping power and a good localization for the ionizing radiation, generally have a high density of electrons and are characterized by a high index of refraction. For instance, LYSO:Ce ($LuYSiO$), the most widely used crystal in Positron Emission Tomography (PET) systems, has an index of refraction of 1.82. This limits by the total internal reflection the amount of light collected by the photodetector, as the coupling material to the photodetector is usually an optical grease or glue with an index of refraction no higher than 1.5. As a consequence, the performance of the scintillator can be severely affected by the transit of the photons from the interaction point to the photodetector, where they will be converted into an electronic signal, leading to delays and absorption losses. For crystals with high aspect ratios, as the ones used in PET scanners, up to 50% of the scintillation light will not be collected [10], even if Teflon wrapping and optical coupling are used, and a large fraction of the collected photons will be delayed by multiple bouncing in the crystal. A higher light output, combined with a reduction of the average path length of the photons in the crystal before their extraction, leads to a better energy and time resolution.

1.3.1 Increasing the Light Output

In the case of the light output, the parameter of interest is the number of photoelectrons N_{pe} registered after a particle has deposited its energy in the scintillator. Typically, N_{pe} is expressed as: $N_{pe}[pe/MeV] = q_{eff} \cdot LY_{out} = q_{eff} \cdot \eta_{coll} \cdot LY_{abs}$, where q_{eff} is the effective quantum efficiency of the photodetector: $LY_{abs} = N_{Php}/E_i$. As already introduced in Section 1, η_{coll} is the light collection efficiency of the scintillation detector and summarizes the impact of all processes leading to losses during the transport of the scintillation photons from the production point to the active region of the photodetector. This includes absorption and scattering in the crystal bulk, absorption and diffusion at wrapping materials and reflection losses due to the mismatch of the refractive index of the scintillator, optical coupling and photodetector. These losses increase the statistical fluctuations of the light output and impact therefore the energy and time resolution.

1.3.2 Improving the Energy Resolution

A good energy resolution is a prerequisite for spectroscopic measurements and of particular interest for environmental conditions' analysis, as well as for homeland security and non-proliferation control. For medical imaging applications (PET and single-photon emission computed tomography (SPECT)), a better energy resolution allows a higher rejection of tissue-scattered events and Compton events in the crystals and improves therefore the spatial resolution and the sensitivity. The sensitivity is a critical parameter of nuclear medical imaging, as it reflects the number of useful events per unit of injected dose to the patient. A higher sensitivity means a smaller injected dose or a better image contrast. A good energy resolution requires a good linearity of the scintillator response as a function of the energy released in the detector, as well as the highest possible light yield. The energy resolution is indeed statistically determined by the number of photoelectrons produced in the photodetector, which is directly proportional to the number of photons extracted from the crystal. Therefore, a high light yield will improve this statistical factor as: $N_{pe}^{-1/2}$.

1.3.3 Improving the Time Resolution

In recent years, fast timing has emerged as a new requirement for scintillator-based detectors, generally related to the study of ultrafast phenomena, as well as to time-of-flight imaging techniques. It is mainly driven by high energy physics (HEP):

in the search for rare events in the planned High Luminosity Large Hadron Collider (HL-LHC) interaction point discrimination will require a sub-20 ps time resolution to mitigate pile-up events produced by particle bunch crossing at a rate $> 1 \times 10^{35} cm^{-2} s^{-1}$ [11]. Time-of-flight positron emission tomography (TOF-PET) applications could also improve, increasing the image signal-to-noise ratio (SNR) with the potential to target the annihilation point along the line of response (LOR) [12], [13], reducing the doses injected to the patients. Time resolutions in the 10-ps range are required in both cases, which boosts the research for scintillators with a high light yield and maximum collection efficiency of the scintillation photons.
The time resolution of a scintillator-based detector is directly driven by the density of photoelectrons generated in the photodetector at the leading edge of the signal. Increasing the light output and as a consequence the rate of photoelectrons produced in the photodetector at the early stage of the signal generation has a direct impact on the time resolution as previously illustrated by Relation (1.7).
The scintillator rise time (τ_r) plays a determinant role for the time resolution and requires a detailed analysis. It affects the photoelectron density in the early stage of the signal, which carries the ultimate timing information [14]. As we have shown in a previous paper [9], several factors contribute to the rise time of the signal produced by a scintillator. Among them, the light transport from the emission point in the crystal to the photodetector plays a significant role if we are aiming at time resolutions in the 100-ps FWHM range or better [15]. Properly-designed photonic crystals allow a redistribution of the scintillation photons to the fast propagation modes in the crystal, further improving the time resolution.

1.4 Inorganic scintillators application requirements

In the following a few of the most diffuse scintillator applications will be presented, each of them with special requirements on the scintillator properties.
For high energy physics, scintillators are used to detect high energy particles (up to a few hundred GeV) in a generally harsh radiation environment, leading to severe constraints in terms of stopping power and radiation hardness. Scintillators for future particle physics experiments are in addition required to have a good time resolution to improve the detection probability of rare events through pile up suppression. Furthermore, high energy physics experiments, in general, have large detection volumes, leading to additional constraints in terms of the cost-effective production and in a reasonable amount of time.
On the other side, for PET, the key performance parameters are the quality of the reconstructed image together with the possibility to detect small tumors and to access dynamically-different molecular pathways with the minimum radioactive dose injected to the patient. The main requirements for scintillators are thus to have a high sensitivity and a high spatial, energy and time resolution. High sensitivity is achieved through a high stopping power and high spatial resolution through crystal size. A good energy resolution enabling an efficient rejection of Compton and scattering events is achieved through a high light yield. A good time resolution is achieved through a high light yield and a very short rise and decay time for the scintillation light. A proper choice of these parameters allows for a significant dead time reduction and a much better coincidence time resolution, leading to an improved image quality and thus to a reduced dose delivered to the patient and a shortened duration of the exam.
In homeland security applications, scintillators are used to detect the presence of explosives and illicit nuclear material and, if possible, to identify their exact composition. A good energy resolution is thus required to identify the characteristic energies of the detected radiation and to precisely identify the radioisotopes present in the object under investigation. The capability to efficiently discriminate between neutrons and gammas also becomes an important feature of the detecting device.

In thermal neutron applications, scintillators are used to build diffractometers. Spallation neutron sources are expensive to build and to operate, and the hadronic interaction exploited by neutron diffraction instruments is inherently weak. The resulting strong requirements on detection efficiency and signal-to-noise ratio impose therefore the use of scintillators with the highest possible light output.

Bibliography

[1] Lempicki, A.; Wojtowicz, A.J.; Berman, E. Fundamental limits of scintillator performance. *Nucl. Instrum. Methods Phys. Res. Sect. A* **1993**, *333*, 304–311.

[2] Robbins, D.J. On Predicting the Maximum Efficiency of Phosphor Systems Excited by Ionizing Radiation. *J. Electrochem. Soc.* **1980**, *127*, 2694–2702.

[3] Knapitsch, A. Photonic Crystals: Enhancing the Light Output of Scintillation Based Detectors; Ph.D. Thesis, Vienna University of Technology, Wien, Austria, 2012.

[4] Pauwels, K.; Auffray, E.; Gundacker, S.; Knapitsch, A.; Lecoq, P. Effect of Aspect Ratio on the Light Output of Scintillators. *IEEE Trans. Nucl. Sci.* **2012**, *59*, 2340–2345.

[5] Auffray, E.; Frisch, B.; Geraci, F.; Ghezzi, A.; Gundacker, S.; Hillemanns, H.; Jarron, P.; Meyer, T.; Paganoni, M.; Pauwels, K.; et al. A Comprehensive & Systematic Study of Coincidence Time Resolution and Light Yield Using Scintillators of Different Size and Wrapping. *IEEE Trans. Nucl. Sci.* **2013**, *60*, 3163–3171.

[6] Dorenbos, P. Fundamental Limitations in the Performance of $rmCe^{3+}$, $rmPr^{3+}$, and $rmEu^{2+}$ Activated Scintillators. *IEEE Trans. Nucl. Sci.* **2010**, *57*, 1162–1167.

[7] Moses, W.W.; Bizarri, G.A.; Williams, R.T.; Payne, S.A.; Vasil'ev, A.N.; Singh, J.; Li, Q.; Grim, J.Q.; Choong, W.S. The Origins of Scintillator Non-Proportionality. *IEEE Trans. Nucl. Sci.* **2012**, *59*, 2038–2044.

[8] Gundacker, S. Time Resolution in Scintillator Based Detectors for Positron Emission Tomography; Ph.D. Thesis, Vienna University of Technology, Wien, Austria, 2014.

[9] Lecoq, P.; Auffray, E.; Brunner, S.; Hillemanns, H.; Jarron, P.; Knapitsch, A.; Meyer, T.; Powolny, F. Factors Influencing Time Resolution of Scintillators and Ways to Improve Them. *IEEE Trans. Nucl. Sci.* **2010**, *57*, 2411–2416.

[10] Gundacker, S.; Acerbi, F.; Auffray, E.; Ferri, A; Gola, A.; Nemallapudi, M.V.; Paternoster, G.; Piemonte, C.; Lecoq, P. State of the art timing in TOF-PET detectors with LuAG, GAGG and L(Y)SO scintillators of various sizes coupled to FBK-SiPMs. *J. Instrum.* **2016**, *11*, doi:10.1088/1748-0221/11/08/P08008.

[11] D. del Re, Timing performance of the cms ecal and prospects for the future. *J. Phys. Conf. Ser.*, **2015**, *587*, 012003.

[12] S. Gundacker et al., Time of flight positron emission tomography towards 100 ps resolution with l(y)so: an experimental and theoretical analysis. *JINST*, **2013**, *8*, P07014.

[13] E. Auffray et al., Characterization studies of silicon photomultipliers and crystals matrices for a novel time of flight pet detector. *JINST*, **2015**, *10*, P06009.

[14] Shao, Y. A new timing model for calculating the intrinsic timing résolution of a scintillator detector. *Phys. Med. Biol.* **2007**, *52*, 1103–1117.

[15] Lecoq, P. Progress on Photonic Crystals. In Proceedings of the Records of the IEEE Nuclear Science Symposium (NSS), Knoxville, TN, USA, 30 October–6 November 2010; Volume 57, pp. 2411–2416.

2

Experimental Methods

The physical properties of the scintillators were measured using several experimental benches. This chapter will describe in details the set up for measuring light extraction efficiency, coincidence time resolution (CTR), timing properties and energy distribution of the scintillation light. These benches are used to compare different configurations and optimize the detector performances.

2.1 Light Yield

As introduced in the previous chapter, the light yield of a crystal is one of the most important parameters, since it directly affects both energy and time resolution.
One precise way to measure the light yield is to make use of a photodetector. The sample is placed in contact (air contact or optically coupled) with the photodetector and excited with a radioactive source (Figure 2.1). The scintillation photons generated by incident ionizing radiation are partly totally internal reflected inside the crystal and a fraction is then extracted from the readout face and collected by the photo-detector. Photons are converted in electrons with a probability related to the instrument used and the emission spectrum of the scintillator: the probability as a function of the wavelength is usually provided with the photo-detector and is called quantum efficiency (QE). The electrical signal generated is amplified and then digitized. A histogram of the integrated signal is finally generated, as already explained in section 1

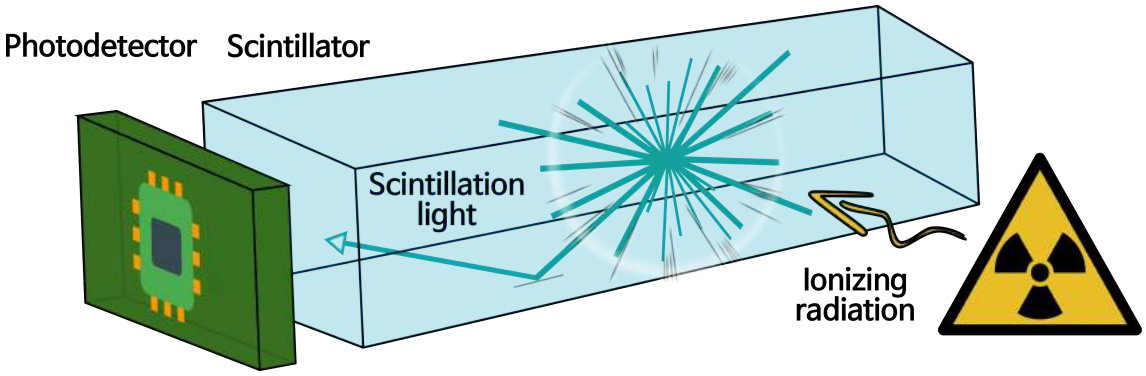

Figure 2.1: Schematic representation of the light yield bench. The radioactive source is placed close to the crystal; the light is collected at the photodetector and generates a voltage amplitude, then is digitized and analyzed in post-processing.

Two kinds of photodetector were used in this thesis with this purpose: photomultiplier tube (PMT) and silicon photo-multiplier (SiPM). Both devices can provide the information of how many optical photons were extracted from the scintillator, if properly calibrated.

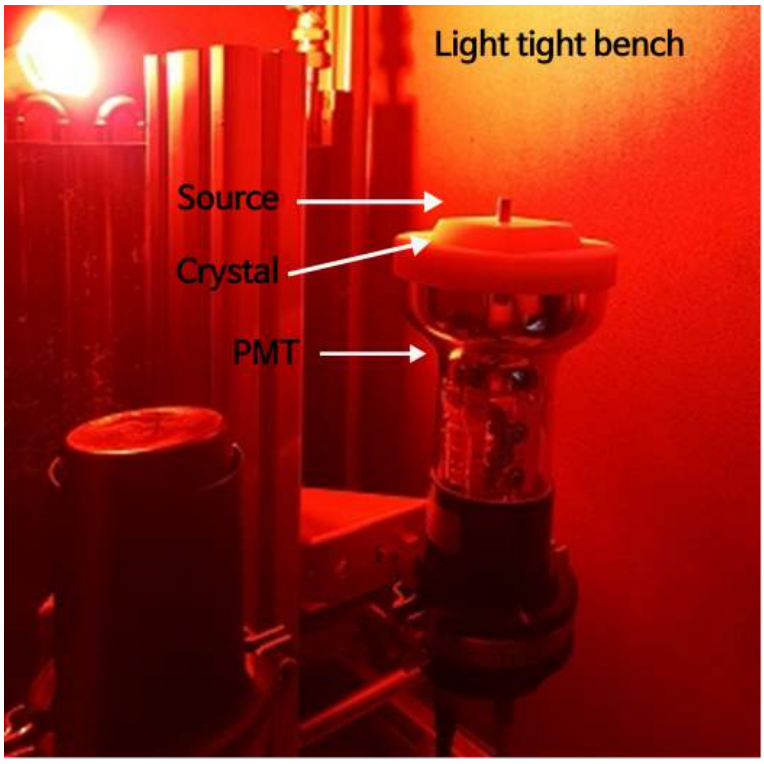

Figure 2.2: LY bench schematic representation. The read-out face of the scintillator is facing the PMT photo-cathode. Gamma source is used, together with digitizer (DT5720A).

When using the PMT (Figure 2.2), in order to calibrate we first evaluate the single electron peak (SE) position, which indicates the very small charge created by single electrons that reach the extraction energy of the photo-cathode due to their thermal energy. The photo-peak position correspond to the total charge collected when photo-electron events take place and a fraction of the scintillation photons are converted into electron by the photo-cathode. Dividing this total charge by the SE charge the number of electrons generated is obtained, and therefore the LY can be expressed as follows:

$$LY = (Pe_{pos} \cdot QE^{-1} \cdot 0.662^{-1})/SE \tag{2.1}$$

QE stands for quantum efficiency and is fixed by the PMT used. In our case the model is an Hamamatsu R10755 for which the QE was measured by our group (Figure 2.3). Using a reference crystal to keep track of the long-term instability of the PMT, for instance, the aging of the photocathode, allow us to keep the $\sigma_{LY} <$ 2%.

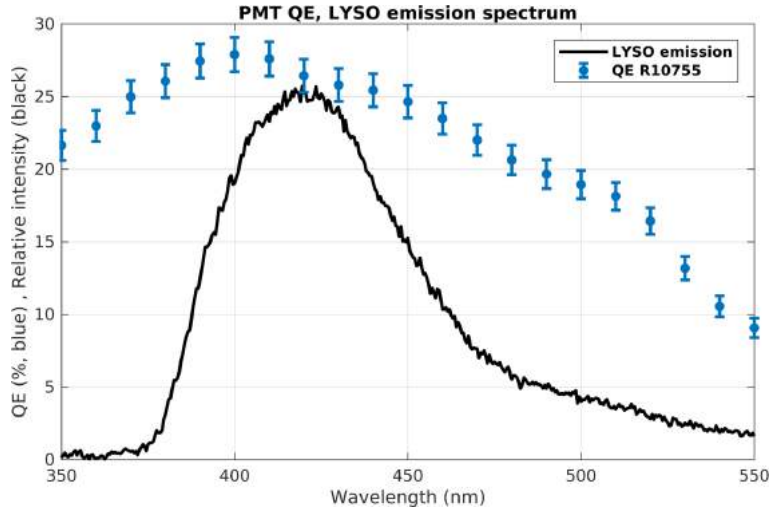

Figure 2.3: Measured QE of the PMT photocathode (blue dots). The superimposed black curve is the relative intensity of an LYSO emission spectrum..

For a SiPM (Figure 2.5), the calibration requires first to characterize the amplifier, since the single electron calibration will be done with maximum amplification while the measurements are usually performed with low amplification factors. In order to do that, a strong LED optical pulsed signal was sent to the SiPM and kept constant along different acquisitions, each one with a different amplification factor. 3 different configurations are available in the set up used. The LED pulses for each amplification gain were integrated and then histogrammed. The position of the peak generated is a precise measure of the signal intensity reaching the digitization step. Figure 2.4 show the different peak position for each amplification factor. The gain observed are 1 (no amplification), 9.91 (medium amplification), and 122.47 (maximum amplification).

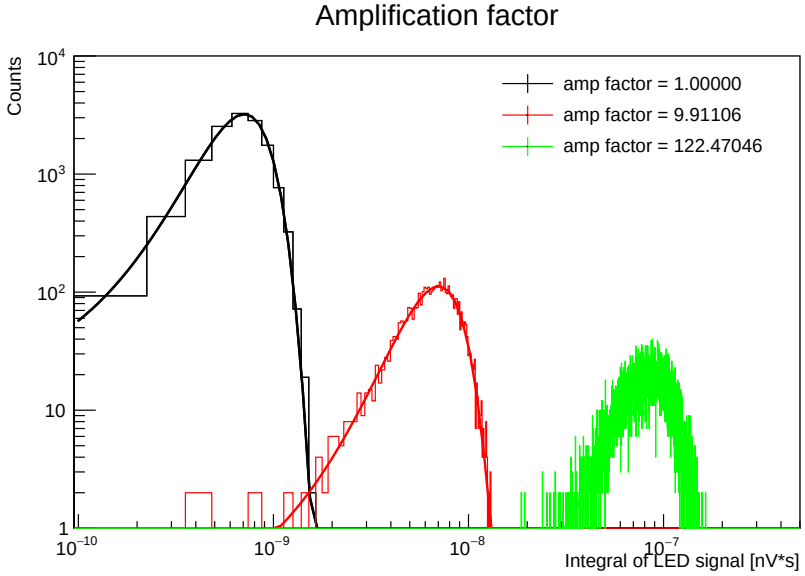

Figure 2.4: Amplifier response study. The gain factors are shown for the different configurations of the jumpers.

Once the amplifier is characterized, the entire system needs to be calibrated. The maximum amplification gain was used to measure low-intensity pulse of the LED.

Due to the low probability of optical photons interacting with the SiPM, integrating the SiPM signal using external trigger from the LED produces, in this case, a discrete Poisson distribution as the one shown in Figure 2.6, which correspond to the probability of a different number of photons of the same LED pulse interacting with the SIPM.

Figure 2.5: SiPM readout configuration. The positions on the PCB of the amplifiers, SiPm, and NINO timing chip (used for CTR measurements 2)are shown.

The distance between one peak and the subsequent is directly proportional to the charge generated by only one SPAD cell triggered. This quantity is the SE charge that one would need to use to calibrate the signal.

$$P_{1st} - P_{0th} = P_{1st} - P_{2nd} = const = SE_{charge} \tag{2.2}$$

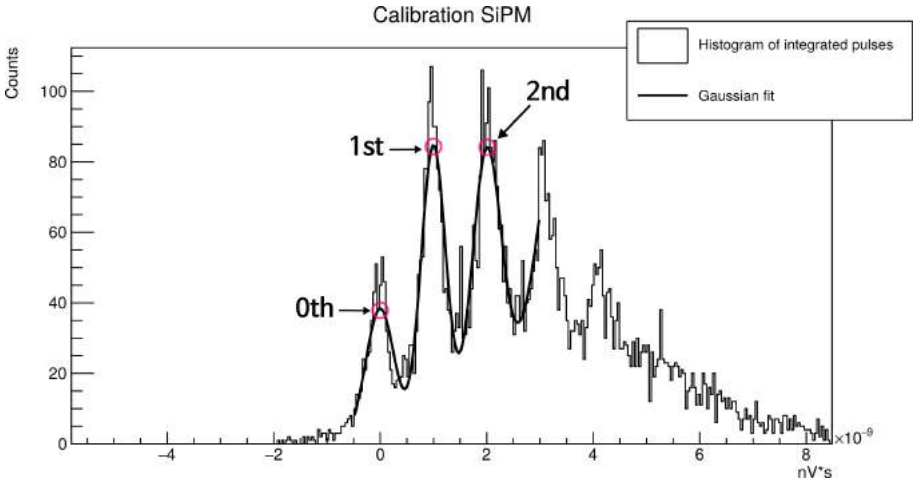

Figure 2.6: SiPM SE charge calibration. The positions on the PCB of the amplifiers, SiPm, and NINO timing chip (used for CTR measu 2)are shown.

Both SiPM and PMT are used to generate a photo-peak spectrum of the source (see chapter 1, section 1). The photo-peak position ($Peak_{pos}$) and full width at half maximum (FWHM) of the peak can be determined and the position of the photo-peak carries information about how many photons were extracted. The FWHM, together with the position of the photo-peak, defines the energy resolution of the crystal, which is given by the ratio between the two quantities $E_{res} = FWHM/Peak_{pos}$.

Part of the work presented in this thesis aim at increasing the LY_{out} of the system and therefore the statistical term of the energy resolution. This optimization uses LY_{gain} as goodness indicator and is defined as the ratio of the light extracted after the patterning and the one extracted before the treatment. Equivalently, the $E_{res-gain}$ is defined as the ratio E_{res} before and after patterning.
This characterization set-up extends to the other LY used during this Ph.D. Some of the work was not performed in situ but instead abroad from other collaborating groups, which follow the same calibration procedure but for a different equipment (PMT model, digitization chain).

2.2 Coincidence Time Resolution

The CTR can be measured using two coincident branches (see [2] for a detailed explanation). On one branch, the sample crystal is placed facing a silicon photo-multiplier (SiPM), which is then readout by a NINO chip, a fast and low noise discriminator developed for the ALICE experiment at CERN [3]. On the other branch, the detection and readout are the same, while the active material is a scintillator crystal with well-known time resolution (see Figure 2.7). Amplitude and timing information are extracted from the system, and a coincidence time resolution curve is obtained, similar to the one shown in Figure 2.8.

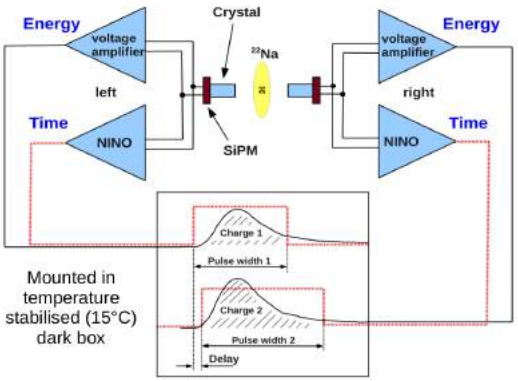

Figure 2.7: Schematic representation of the coincidence time resolution (CTR) bench [2]. SiPM, silicon photo-multiplier.

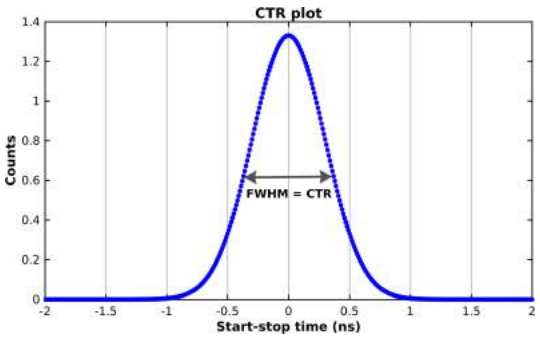

Figure 2.8: Example of a CTR histogram. The FWHM of the curve is the CTR of the coincident system [2]

The distribution of the time differences between start and stop events is a Gaussian (Figure 2.8), and its FWHM is the CTR of the entire system, i.e., the contribution from the sample crystal ($deltat_{sample}$) together with the reference crystal component

($deltat_{ref}$).

$$CTR = 2.36 \cdot \sqrt{\sigma^2_{sample} + \sigma^2_{ref}} \tag{2.3}$$

A deconvolution is needed to separate the contribution of the reference crystal: the value obtained has to be multiplied by $\sqrt{2}$ to simulate a system consisting of two crystals identical to the tested sample.
In the case of the CTR, the 'goodness' indicator is:

$$CTR_{gain} = CTR_{untreated}/CTR_{treated} \tag{2.4}$$

LY extracted and CTR are correlated by equation 1.7, therefore it is possible to define a proportionality between the CTR gain and LY gain:

$$CTR_{gain} \propto \frac{1}{\sqrt{LY_{out}}} \tag{2.5}$$

2.3 Time resolved spectroscopy

Energy and temporal distribution of the scintillation photons play a key role in scintillation detection, depending on how many photons are produced and how fast they are collected. The system described in this section is a fast and precise tool to measure both these properties at the same time. A spectrometer (energy distribution) and a streak camera (time distribution) were placed on the same optical path working at 90° shift between each other, providing time over one axes and energy on the other. The result is a 2-dimensional image collected by a CCD, perpendicular to the collimation direction.
A diagram of the set-up is shown in Fig 2.9.

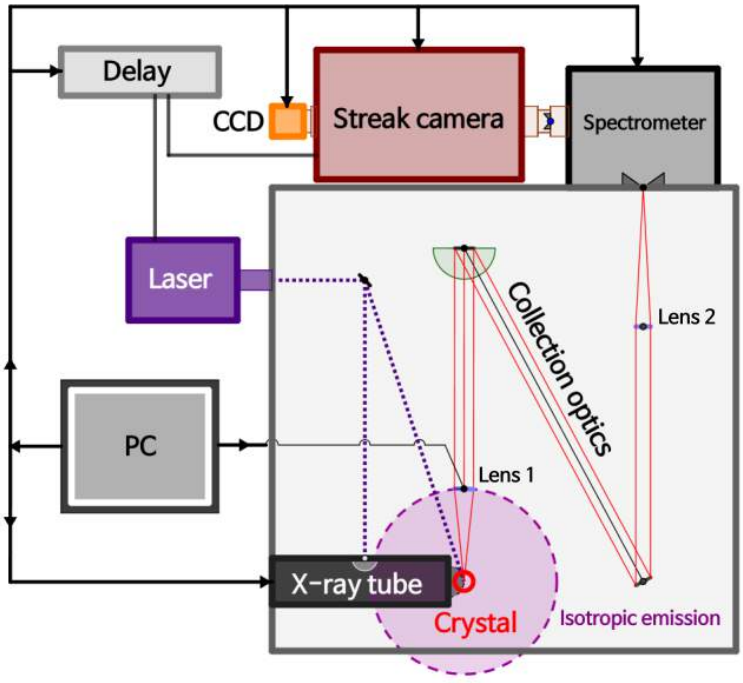

Figure 2.9: Schematic representation of the experimental bench for energy and time distribution measurements.

2.3.1 Radiation source

It is possible to excite the sample with two different pulsed sources: direct laser excitation for low energy and a high energy X-Ray tube (XRT), triggered by the laser itself. The first mirror in front of the laser in Fig. 2.9 select between the two path.
The laser is a PiLAS picosecond diode with 372 nm emission, with a spectral width of 1.51 nm. The x-ray tube is a Hamamatsu N5084, a high voltage device which accelerates electrons coming from the photocathode to a heavy metal ion, giving a directional emission of bremsstrahlung photons up to 40kV (bounded to the operating voltage).
The tube is vacuum sealed, the window interface toward the sample is made of beryllium while the excitation window is a photocathode covered by a protective glass. The glass was chosen in function of the energy of the triggering laser, in order to avoid browning of the material. This would create color centers that can absorb the laser light, therefore lowering the X-rays intensity. The QE of the glass used is 8% at 372 nm and it drops to 5% in 100 hours of work.
The position of the tube in the set up was chosen to minimize the damages that X-rays exposure can cause to the spectrometer. A set of lenses were used to guide and collect the light from the sample to the spectrometer input window.

2.3.2 Sample placing and light collection

The sample is placed on top of a motorized X-Y-Z stage. The isotropic light coming from the sample is collimated using a lens with focal length f = 6 cm and a diameter d = 5.08 cm(2 inches). The choice of a short f, although the aberrations, is to minimize the geometrical losses of scintillation light.
Fig. 2.9 show the path of the light collimated from the first to the second (focusing) lens. The two mirrors have the same dimension as the first lens. A loss of 10% has to be taken into account after each reflection. The second lens has an f= 15 cm and d= 5.08 cm and is placed on an X-Y stage.
All the optical elements were placed on the same horizontal plane of the spectrometer grating to avoid efficiency drop.

2.3.3 Spectrometer

The spectrometer 2300i Spectrograph is used to separate the spectral component of the light making use of interference pattern of a diffracting grating. It has three different gratings, with 50, 150 or 300 grating/mm. Each grating has a blaze wavelength of 500 nm, with an efficiency of 60,80,75% for 515 nm and 30,40,60% for 400 nm respectively. The selection is controlled by a computer (in Figure 2.9, PC). It is possible to move into different wavelength range and to manually change the intensity by adjusting the dimensions of the two slits.
The system needs to work in a clean environment, to avoid dust to deposit inside the spectrometer optics causing diffraction pattern inside the image.

2.3.4 Streak camera

The streak camera (Figure 2.10) allows studying the temporal shape of the photon emission. The different wavelength selected by the spectrometer pass through the second slit and a group of focusing optics, colliding to a stripe photocathode. Electrons are generated with an efficiency of 10% and guided between the electrodes of a sweeping unit, where a fast high voltage gradient is applied. The electrons arriving at different times are deflected at different angles in the perpendicular direction and are then collected by a micro-channel plate (MCP). The MCP multiply the electrons with a gain ranging from 6 to 7000, controlled by a high-voltage from

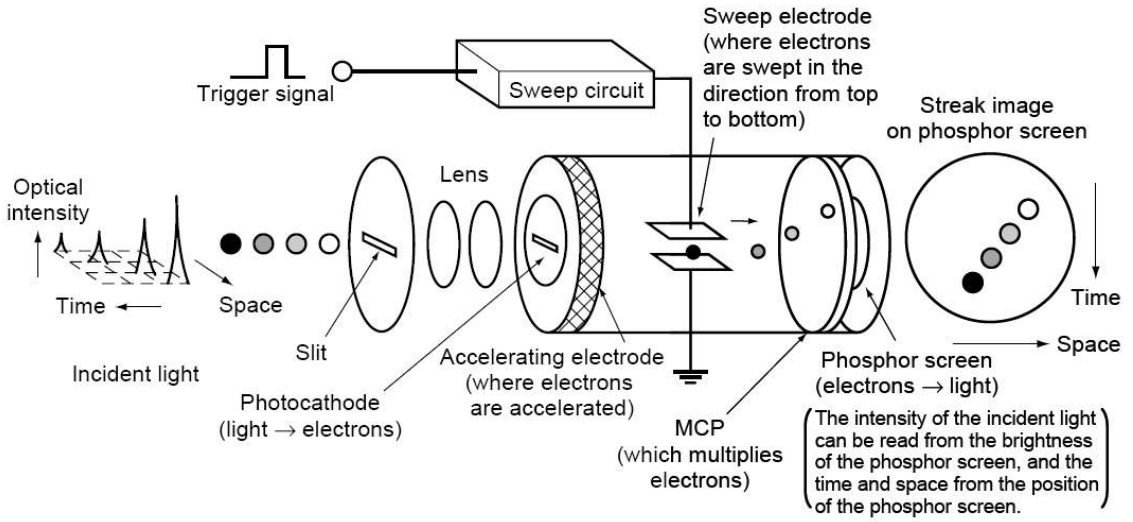

Figure 2.10: Schematic view of the instrumental setup main components.

400 to 900 V. The shower of electrons then collides on a phosphor screen, where they are re-converted in photons. The brightnesses of the various fluorescence images are proportional to the intensities of the corresponding incident light pulses. The positions in the horizontal direction on the phosphor screen correspond to the positions of the incident light in the horizontal direction, therefore the wavelength decomposition generated by the spectrometer.
The photon counting mode gives the possibility to register single electrons that reach the MCP. Those are multiplied at a high integration rate, and one photoelectron is counted as one intensity point on the phosphor screen. A threshold value used to reduce the noise: events in the photoelectron image which are above the threshold value are detected and integrated into one final image. This method allows achieving data measurements with a high dynamic range and high signal to noise ratio.

2.3.5 CCD

The CCD system is the last element of the system chain that measures the scintillation. It is a CMOS sensor of $13.3 \times 13.3 mm^2$, with 80% efficiency at 600 nm, fan cooled and with 100 f/sec resolution.
The camera is controlled by the software interface of the streak camera, and the available parameters are the exposure time, the shutter (close or open) and the threshold. This value will change the number of photons that need to be recorded on a restricted number of pixel (in the vicinity of a certain centroid), in order to count a single photon that had entered the MCP. The CCD ultimately record the energy and temporal component on a bi-dimensional matrix containing both the decomposition of the spectrometer and the streak camera.

2.3.6 Response of the system

The total instrument response function (IRF) was determined by measuring the temporal profile of the laser under the same measurement settings, i.e. sweeping range, optical path, and photocathode slit aperture. For a 100 μm slit aperture and 5 ns sweep range it is a Gaussian of 126 ps FWHM. The final IRF is the result of convolving the asymmetric tube time response (FWHM of 40 ps) with the laser response, resulting in an IRF of 134 ps FWHM. The total IRF used to analyse X-ray excited data is the convolution of the laser IRF and the X-ray IRF. In the case of a

2 ns sweeping range, the laser IRF reduces to 63 ps FWHM, and the total IRF has a FWHM of 74 ps. Measurements were done in single photon counting mode and calibrated by sweeping range non-linearities. Two different fit procedures were used depending on laser or X-ray excitation (laser IRF or total IRF). The laser-excited results were analyzed with the following formula [3] where the convolution using the laser IRF is done analytically:

$$F(t) = \sum_{i=1}^{N} \frac{y_i}{\tau_{d,i} - \tau_{r,i}} \cdot exp^{\frac{2\tau_{d,i}(\theta - t) + \sigma^2_{IRF}}{2\tau^2{}_{d,i}}} \cdot [1 - erf(\frac{\tau_{d,i}(\theta - t) + \sigma^2_{IRF}}{\sqrt{2}\sigma_{IRF} \cdot \tau_{d,i}})] \tag{2.6}$$

$$- \sum_{i=1}^{N} \frac{y_i}{\tau_{d,i} - \tau_{r,i}} \cdot exp^{\frac{2\tau_{r,i}(\theta - t) + \sigma^2_{IRF}}{2\tau^2{}_{r,i}}} \cdot [1 - erf(\frac{\tau_{r,i}(\theta - t) + \sigma^2_{IRF}}{\sqrt{2}\sigma_{IRF} \cdot \tau_{r,i}})] + C$$

Here, θ describes the start of the emission process and the electronic delay. The term C accounts for the background coming from the MCP noise. The sum stands for the number of components characterizing rise and decay times. For X-ray excited data, a fast Fourier transform convolution is done by building up a probability density function as a model to fit the data. Parameter errors are calculated using the Minos algorithm. The function used to convolve with the asymmetric IRF is the following [3]:

$$f(t) = \sum_{i=1}^{N} \frac{y_i}{\tau_{d,i} - \tau_{r,i}} \cdot exp^{\frac{(\theta - t)}{\tau d,i}} - \sum_{i=1}^{N} \frac{y_i}{\tau_{d,i} - \tau_{r,i}} \cdot exp^{\frac{(\theta - t)}{\tau r,i}} \tag{2.7}$$

Both functions are normalized to the total photon yield, therefore y_i represents the abundance of each component in terms of photons emitted. In order to minimize the degrees of freedom, the rise time for different components is set as one parameter, since the resolution does not allow a proper estimation of recombination times smaller than 18 ps. For both analyses, the fractional weights are P calculated as $Y_i = y_i \setminus \sum_i y_i$, which is the percentage of photons emitted with a lifetime component τ_i.

3

Testing the limit of the current technology

This chapter will present the studies performed in order to foster the limit of the current scintillation technology. Three classical approaches were investigated to improve the performances of the scintillators:

- explore new scintillating materials, trying to better match a specific or multiple requirements,
- change the geometry of an already known material to optimize light extraction,
- readout configuration, changing the coupling between the scintillator and the photo-detector.

This tests allowed also to better understand the scintillation process and tune simulations accordingly.

3.1 Material optimization with Cs_2HfCl_6

The first approach while researching for boosted scintillation properties of the materials is to change the performances of scintillator material itself, in order to obtain a faster and precise time and energy tag generated at the interaction point. This will improve the third term in 1.4, i.e. the intrinsic contribution of the photons generation and homogeneity of the scintillator volume. Ideally, if one could find a material that creates a small band gap with low thermal noise and be able to grow it homogeneously, that will generate a high light yield and good energy resolution crystal, constituting a breakthrough for particle physics detector. Research in this direction is still very active but finding the right balance between properties is made complicated by the high number of degrees of freedom: hygroscopicity, toxicity, costs, process stability and purity, Stokes shift and high density.
With the purpose of obtaining a high energy resolution crystal, the production and characterization of a relatively new intrinsic scintillator was investigated. Cs_2HfCl_6 single crystals appear to be very interesting for scintillator applications due to its high LY and good energy resolution, together with cubic structure of high symmetry and low hygroscopicity. Its cubic crystallographic structure could enable manufacturing of the transparent ceramics, already explored in other halides. It is a cost-effective crystal and highly proportional without the use of dopant, showing low reactivity as well at room temperature. A comparison of Cs_2HfCl_6 crystal properties with other popular halides is shown in table 3.1.
It can be noted how other halide scintillators are as good as Cs_2HfCl_6 in terms of energy resolution and in some case with faster decay time ($LaBr_3 : Ce$). These materials are on the other hand hygroscopic and more expansive to produce because of the encapsulation needed to protect them from air moisture as well as the additional costs of rare earth doping. Moreover, the use of moisture-free capsules is a disadvantage in applications where close packing is needed, such as HEP experiments. If properly grown, Cs_2HfCl_6 could offer a cost-effective and practical option.

Table 3.1: Properties of most widely used scintillating halides:

	Cs_2HfCl_6	$NaI:Tl$	$CsI:Tl$	$SrI_2:Eu$	$LaBr_3:Ce$
Density $[g/cm^3]$	3.8	3.4	4.5	4.6	5.3
Structure	Cubic	Cubic	Cubic	Orthonorm.	Hex.
E_g	6.3	5.8	6.1	5.5	5.9
Zeff	58	50	51	49	47
λ Max [nm]	380	410	540	430	360
τ [ns]	300, 4.4 (5%, 9.5%)	230	1100	600-2400	35
LY$[ph/MeV]$	54,000	38,000	66,000	100,000	61,000
E_{res} [%]	3-4	7	6	3-4	3
Higroscopicity	no	yes	yes	yes	yes

3.1.1 Experimental details

A sample of Cs_2HfCl_6 compound was prepared in collaboration with the FZU institute of the Czech Academy of Sciences, by the direct synthesis from cesium chloride ($CsCl$) and $HfCl_4$ raw materials mixed together with the stoichiometric ratio 2:1, as described in [4]. After synthesis, the material was purified using a combination of gaseous halogenation agents introduced into its melt and zone-melting technique. The growth environment was sealed quartz ampoules and the method used unseeded vertical Bridgman method at the pulling rate in the range of $0.3-0.4mmh$ and temperature gradient of $\sim 40K/cm$. The dimensions of the as-grown crystals defined by the shape of the ampule were 12 mm in diameter and $\sim 40mm$ in length. The crystals showed twining and contained several secondary grains in the tip of the ampule. Nevertheless, only a few of them were preferred and allowed growth of homogeneous grains of sufficient size, ranging from 5 to 15 mm. The Cs_2HfCl_6 samples for optical characterizations were cleaved from the grown crystals along the (111) plane. No cutting or polishing of specimens was required. The sample crystallizes in simple cubic structure with the lattice constant of 1.042 nm [1]. It is isostructural to K_2PtCl_6 and analogous to antifluorite CaF_2 structure in which Cs occupies all tetrahedral sites and Hf all face-centered cubic sites in the lattice. The Cl anions equally surround the Hf cation forming undistorted octahedron [3],[2]. The sample produced are shown in Figure 3.1.

3.1.2 Scintillating properties

Several tests were performed on the crystals produced in order to asses the quality of the production process. The photoluminescence (PL) and photoluminescence excitation spectra are shown in [4]: under excitation around the absorption edge, at 200 nm, the PL spectrum features a broad emission band with the maximum at $\sim 375nm$ at both room temperature and 8 K. Different samples were produced starting from the raw material (Figure 3.1). The X-ray decay time was measured using the streak camera set up described in section 2, therefore excited trough X-ray pulses. The resulting time dependent emission is shown in Figure 3.2. Two decay component are observed, with $\tau_1 = 340ns$ and $\tau_2 = 4.40\mu s$. This values are compatible with values stated in [1], which suggests a good material synthesis.
LY measurements were performed on the samples and compared with LYSO of similar shape and with the same wrapping/coupling configuration. The setup is described in the method section and the source used Na_{22}. The results are summarized in Table 3.2.
The samples with cubical shape (CHC1) presented in Figure 3.1c shows a LY comparable with the LYSO samples (40'000 ph/MeV intrinsic LY), which mean a lower LY than the one expected (54'000 ph/MeV). A factor ~ 2 higher LY were observed for

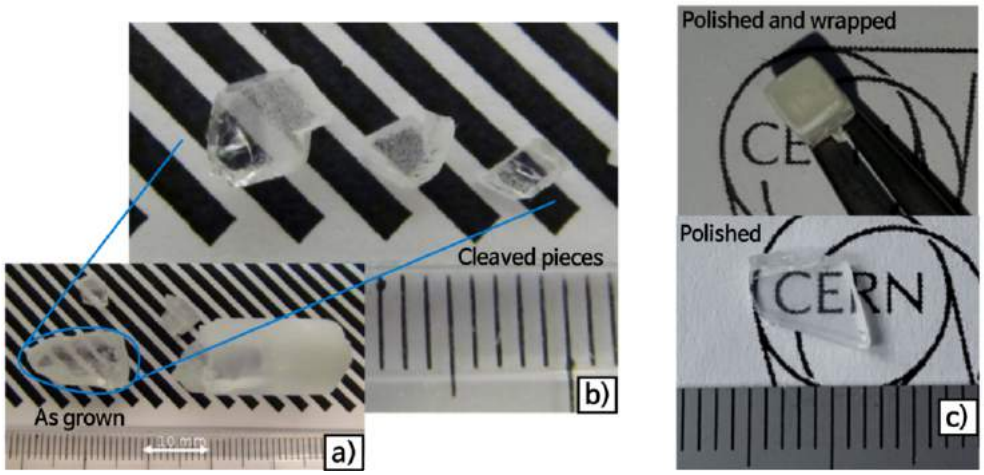

Figure 3.1: The sample history is shown: a) 'as grown' raw crystal, from which b) were selected and cleaved as highest quality region. c) shows a $3 \times 3 \times 5mm^3$ sample polished and wrapped and d) shows a plate configuration ($\sim 1 \times 1 \times 4mm^3$) of the same raw material, polished on the two biggest faces. The samples looks transparent from visual inspection.

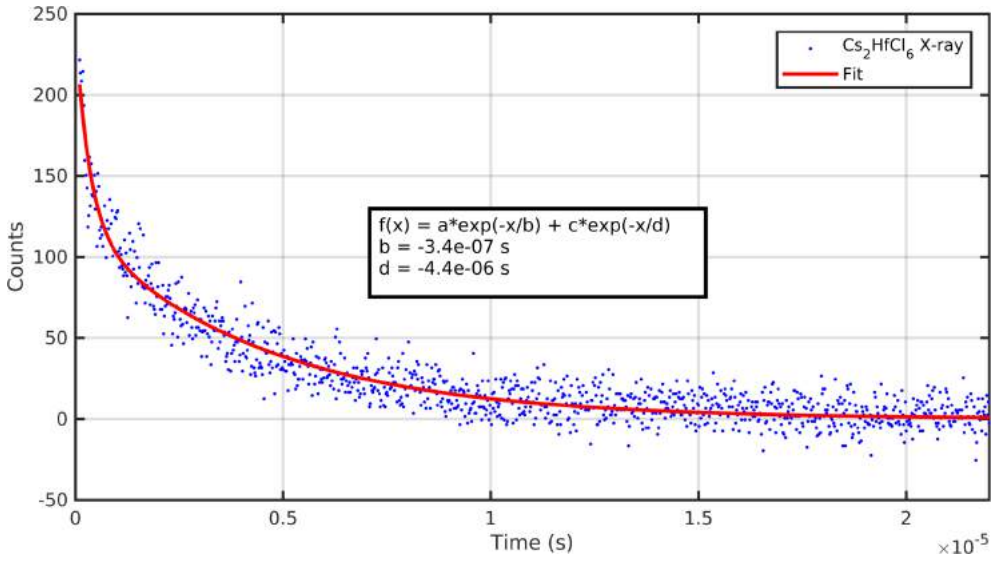

Figure 3.2: Decay time measurements of the $3 \times 3 \times 5mm^3$ Cs_2HfCl_6 sample.

Table 3.2: Sample produced from the Cs_2HfCl_6 raw material:

Sample configuration	Dimensions (mm)	Photopeak (ADC ch)	Energy res. %
CHC1 Teflon wrap, IR = 1.504	$3 \times 3 \times 3$	10780	17
LYSO Teflon wrap, IR = 1.504	$3 \times 3 \times 3$	12570	13
LYSO Teflon wrap, IR = 1.504	$3 \times 3 \times 5$	12070	13
CHC2 Teflon wrap, IR = 1.504	'plate' $4 \times 4 \times 1$	24860	12
CHC3 Teflon wrap, IR = 1	'plate' $4 \times 4 \times 1$	27440	17
CHC4 Teflon wrap, IR = 1	'plate' $3 \times 3 \times 1$	24960	14
CHC5 Teflon wrap, IR = 1	'plate' $3 \times 3 \times 1$	24960	14

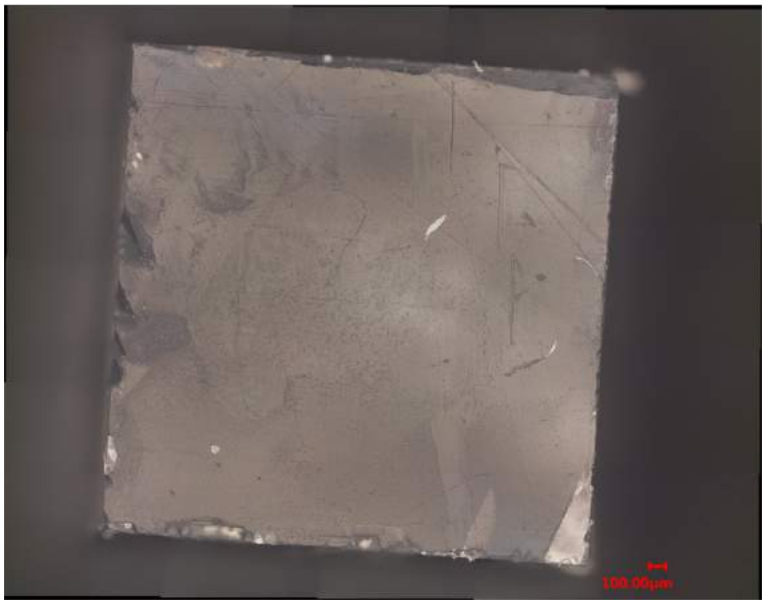

Figure 3.3: Read out $3 \times 3 \times 3mm^3$ surface of CHC1, Cs_2HfCl_6 scintillator, showing surface damages.

different aspect ratio (CHC2-3-4-5): the 'plate' configuration favors light extraction minimizing the travel inside the volume. This would suggest a source of absorption or scattering inside the material that will decrease the LY in the case of higher mean path inside the scintillator, such as in the $3 \times 3 \times 3$ crystal. Optical microscopy was used in order to evaluate the surface state and volume imperfections of the samples. Figure 3.3 shows the read out surface of the scintillator while Figure 3.4 shows the result of a volume defects investigation.
The optical analysis confirmed the presence of both surface defects and scattering centers inside the volume. These inhomogeneities could be the cause of LY degradation, especially when high aspect ratio geometries are used. Energy resolution is also affected by the defects: values between $3 - 4\%$ were measured for Cs_2HfCl_6, whereas the sample measured shows much higher values.
The LY of the sample was subsequently used as a marker for hygroscopicity test on the material since the sample is known to be moderately reactive to atmospheric moisture. The Cs_2HfCl_6 crystal with dimensions $3 \times 3 \times 5mm^3$ was wrapped and left is contact with air for 335 hours and measured for a long period of time. The result of this experiment is shown in Figure 3.5.
The sample was found to be reactive mostly to glycerin, used in this case as optical coupling with RI = 1.47. The prolongated contact with the hydrophilic glycerol produced degradation of the surface state on the readout face, causing a sudden drop in the LY measured. Using an inert silicon-based coupling will reduce this

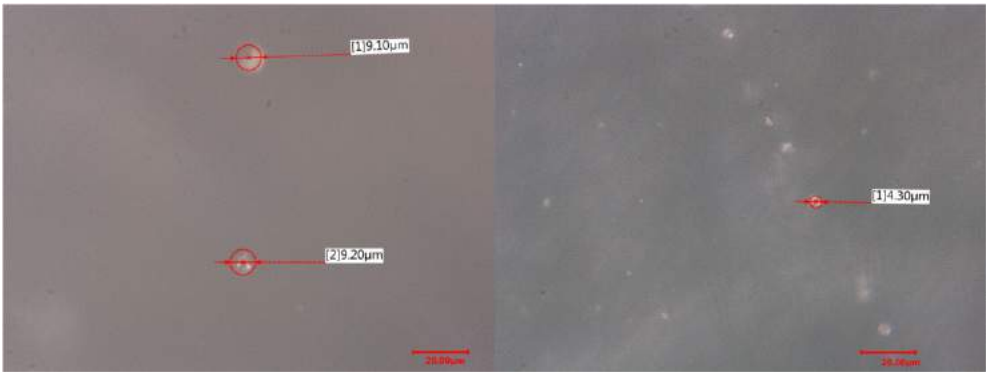

Figure 3.4: Volume defects were observed inside the crystal. The dimensions of the features suggests that the nature of the defects could be bubbles or impurity conglomerations.

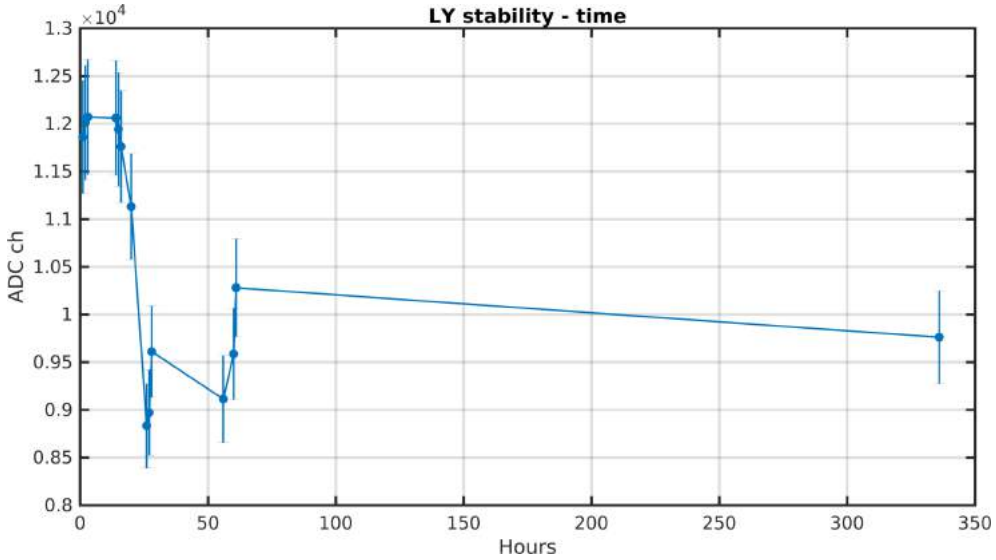

Figure 3.5: LY measurement performed in different moment during the sample exposure to air.

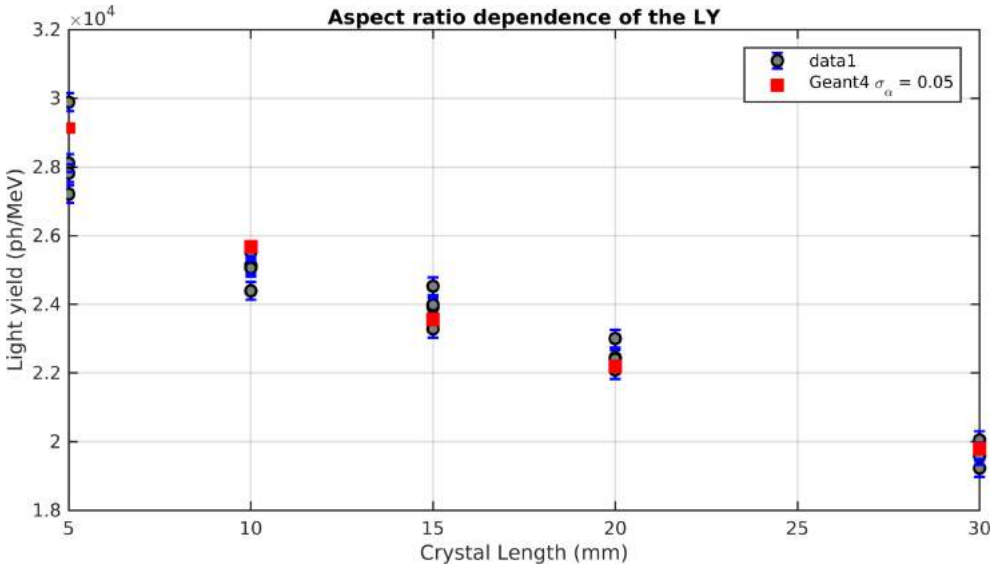

Figure 3.6: LY as a function of the LYSO crystal aspect ratio. The readout face dimension is kept fixed to $3 \times 3mm^2$, several crystals were measured with different length. The squares are Geant4 simulations while circles are LY measurements.

effect, leaving the crystal almost intact after the prolongated exposure.

3.1.3 Discussion

From the point of view of creating boosted scintillator detectors, *R&D* on new materials has the potential to tune the crystal properties on the required application and is still far to be fully explored. Halides are promising materials, offering powerful scintillating properties with a high level of homogeneity. Cs_2HfCl_6 could bring together the advantages of halides scintillator without the major drawback of hygroscopicity. The path to optimize the production process of this crystal requires a fine-tuning of the growth parameters and material composition and future work will continue in the direction of better homogeneity and surface treatment.

3.2 Geometry optimization of LYSO crystal

The geometry of a scintillator is known to influence light collection as well as the energy resolution of the detection. Lowering the aspect ratio of the crystal can increase the light extraction of the photons ([6],[7],[8],[9],[10]) while breaking the symmetry of a scintillation crystal was also found to be advantageous for high light output [11]. Depending on the RI of the scintillator, its Rayleigh length, polished finish and non-readout face wrapping, the optimal geometrical configuration changes. This section will investigate the optimal configuration for LYSO:Ce crystals produced by CPI, polished and Teflon wrapped, with readout face section $3 \times 3mm^2$. The measurements will be compared with simulated values. The LY setup used in this experiment is described in section 2, using a Hamamatsu R10755 PMT. Three crystal of each kind were available and each crystal has been measured three times. The error reported in the following data analysis is the standard deviation obtained within every crystal measurements. The measured LY as a function of the length of the crystal (the dimension perpendicular to the readout face) is shown in Figure 3.6. Lower the aspect ratio, smaller the path of the photons inside the crystal and higher the extraction probability: the LY increase for smaller length of the scintillator, go-

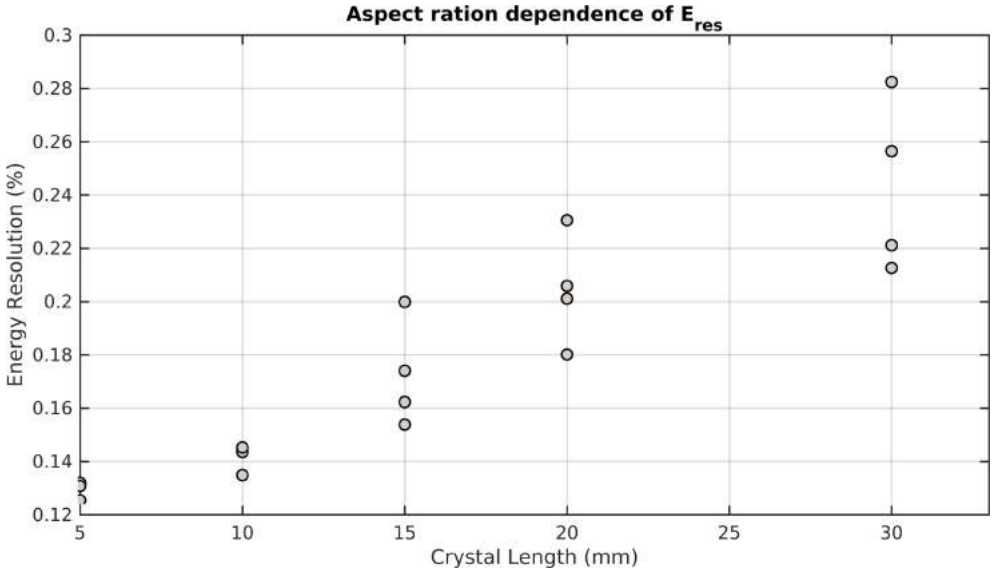

Figure 3.7: Energy resolution as a function of the LYSO crystal aspect ratio. The read out face dimension is kept fixed to $3 \times 3mm^2$, several crystals were measured with different length.

ing from an average value of $19'549ph/MeV$ for the 30 mm long to $28'124ph/MeV$ of the 5 mm. The simulations fits the measurements for a value of depolishing $\sigma_\alpha = 0.05$ (see section 4 for more details about the simulations parameters).

The E_{res} as well improves for smaller aspect ratio, as it can be seen from Figure 3.7. Following the increase in LY 1.4, the photostatistic component decreases and the E_{res} drops from a value of 28% for the 30 mm long crystal to the12.5% for 5 mm length.

3.2.1 Discussion

Smaller aspect ratios show better performances in LY and E_{res} because they minimize the path of the photons before extraction and this makes small crystals the best choice from the performances point of view. The same was observed in a similar work for CTR measurements as a function of the crystal aspect ratio, shown in [5]. A gain in CTR performances is observed moving to smaller aspect ratio, which confirms the higher light transport efficiency towards the photo-detector. Technological and practical constraint, on the other hand, often pushes towards higher volumes: given the detection surface to be covered, smaller the dimension of the crystal higher the number of readout channels and more complicated the system becomes. Too small crystals with small aspect ratios are difficult to scale in volume and have a smaller sensitivity: a trade-off is needed depending on the specific application.

3.3 Optical coupling optimization of LYSO and GaGG crystals

One of the big limitations of scintillator detection is related to transferring the scintillation photons from the high refractive index material to the usually low refractive index of the photo-detector. This mismatch is held by two limits. The high refractive index of the scintillator is a consequence because of the high density, which defines the stopping power of the material and the ability to detect high energy gamma-ray. On the other side the low refractive index of the photo-detector window (e.g. RI of

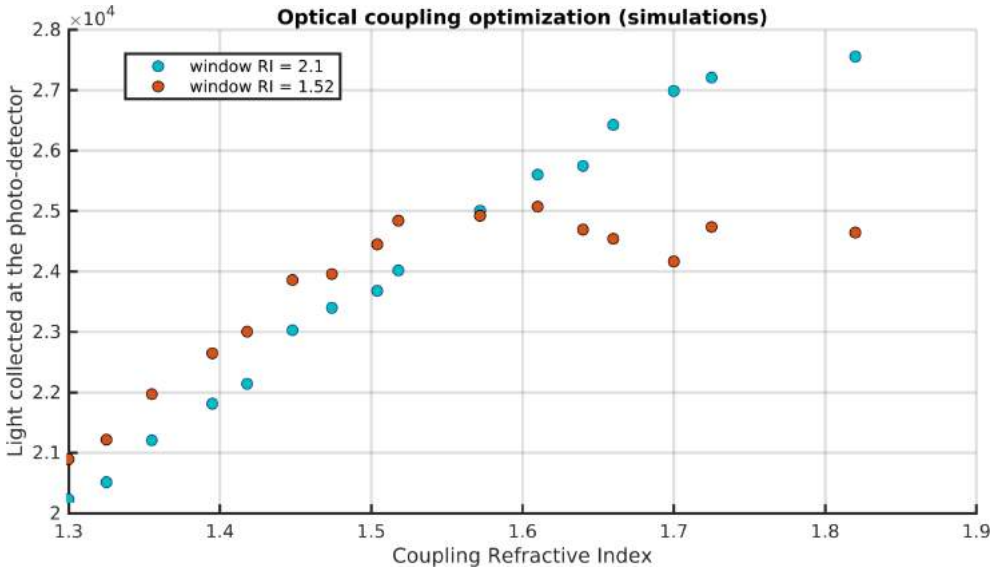

Figure 3.8: Simulated LY of a Teflon wrapped $2\times2\times10mm^3$ LYSO crystal, coupled with different optical agents to the photo-detector. The photo-detector is simulated as a volume with IR = 1.52 (orange dots) and with IR = 2.1 (blue dots).

epoxy glass $\tilde{1}.5$) is linked to the production, and therefore follows cost optimization: a wide range of applications does not require to couple to a high refractive index material such as a scintillator, therefore the R&D and industrial investment does not justify the potential gain.
We investigated several optical couplings with different refractive indexes to minimize Snell's and Fresnel reflection losses. In parallel, we studied the feasibility and critical aspects of an innovative way of thinking about the system scintillator-photodetector by mean of a minor adjustment in the production process of the SiPM, one of the most widely used photo-detectors. Thanks to the collaboration with Fondazione Bruno Kessler (FBK) we were able to test a modified version of the devices with a higher refractive index interface, which has the potential to increase the critical angle to values close to 90°. In this section simulations and measured data will be presented in order to underline the potential and critical aspects of boosting scintillation light detection through optical coupling optimization.

3.3.1 Results

The effect of different optical couplings, with different refractive indexes, was evaluated using the LY benches (both PMT and SiPM) and Geant4. Several configurations were tested using commercially available optical couplings, for both LYSO ($Lu_{1.8}Y_{.2}SiO_5 : Ce$) and GaGG ($Ga_3Al_2Ga_3O_{12} : Ce$) scintillators. The choice of the scintillator was driven by the wide use of scintillators for what concerns medical and HEP applications (LYSO) and homeland security (GaGG).
The simulated trends for the LY as a function of the optical coupling RI are shown in Figure 3.8 and Figure 3.9. Both the crystal have dimensions $2 \times 2 \times 10mm^3$ and Teflon wrapping on the non-readout faces (with $1\mu m$ estimated residual air gap between the scintillator surface and the wrapping). Two different configurations are displayed for each crystal: with a low RI of the optical window RI = 1.52 (borosilicate glass for PMT and epoxy window) and with high RI = 2.1. The plot for the GaGG shows a potential LY gain of 20.6% while for LYSO the maximum gain is expected to be 9.9%. For RI < 1.52, the high RI index window configuration always shows smaller LY than the RI = 1.52 case: this is probably due to higher Fresnel losses at the interface.

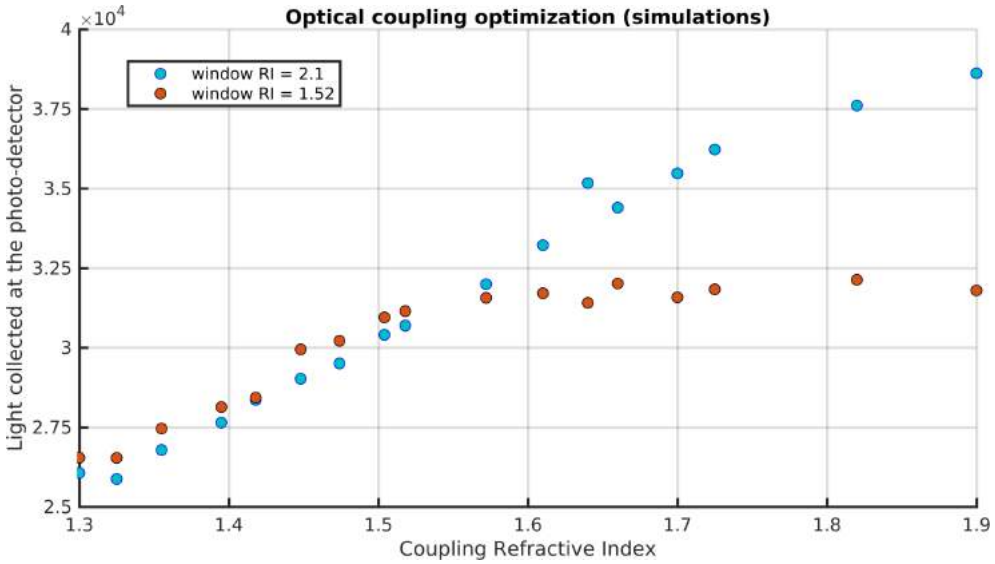

Figure 3.9: Simulated LY of a Teflon wrapped $2 \times 2 \times 10mm^3$ GaGG crystal, coupled with different optical agents to the photo-detector. The photo-detector is simulated as a volume with IR = 1.52 (orange dots) and with IR = 2.1 (blue dots).

The LY measurements setup is described in chapter 2. FBK NUV 20 μm cell pitch, $5 \times 5mm^2$ SiPM were used, with two different production layouts: one with an epoxy (RI = 1.52) protective layer and one without it, therefore with an RI = 2.1. The SiPM were fully characterized in terms of photo-detection efficiency (PDE), SE charge (needed for calibration) and saturation (Figure 3.10). The experimental results are shown in Figure 3.11, for a constant voltage of 29V, Na_{22} source and a $2 \times 2 \times 10mm^3$ LYSO:Ce crystal, Teflon wrapped: The configuration that performs the better in terms of LY is the SiPM with epoxy window, with an optical coupling of RI = 1.45, therefore close to the RI_{epoxy}. The drop which follows can be once again attributed to the Fresnel losses created in the interface between optical coupling and epoxy window (case of the blue data) while the difference in LY between the measurements (max value = $33640ph/MeV$) and the simulations (max value = $27553ph/MeV$) is mostly coming from crosstalk and after pulse generated in the SiPM device, for which no correction was calculated. From simulations, a linear increase of the LY as a function of the RI of the coupling was expected but is not observed in the red curve. This suggested a lower index of refraction at the interface between the optical coupling and the SiPM. An investigation of the SiPM structure revealed the possible presence of a SiO_2 layer of μm thickness, which would considerably lower the RI of the interface ($RI_{SiO_2} = 1.47$). This is a passivation layer deposited on the surface to prevent atmosphere to react with the Silicon, creating defects and impurities that could cause higher Dark Current in the device. This layer can be substituted during the SiPM production with a higher RI material such as Si_3N_4, RI = 2.1. Further work will investigate the performance of LYSO and GaGG with high RI coupling and Si_3N_4 passivation layer, in order to fully explore the potential gain of this new technological approach.

3.3.2 Discussion

Studying optical coupling between the scintillator and its photo-detector produced several outcomes. Simulations were run and a good match was found for several configurations, which constitute a solid validation of the code and the tools used (Geant4). We are now also aware that the RI of the coupling needs to be as high

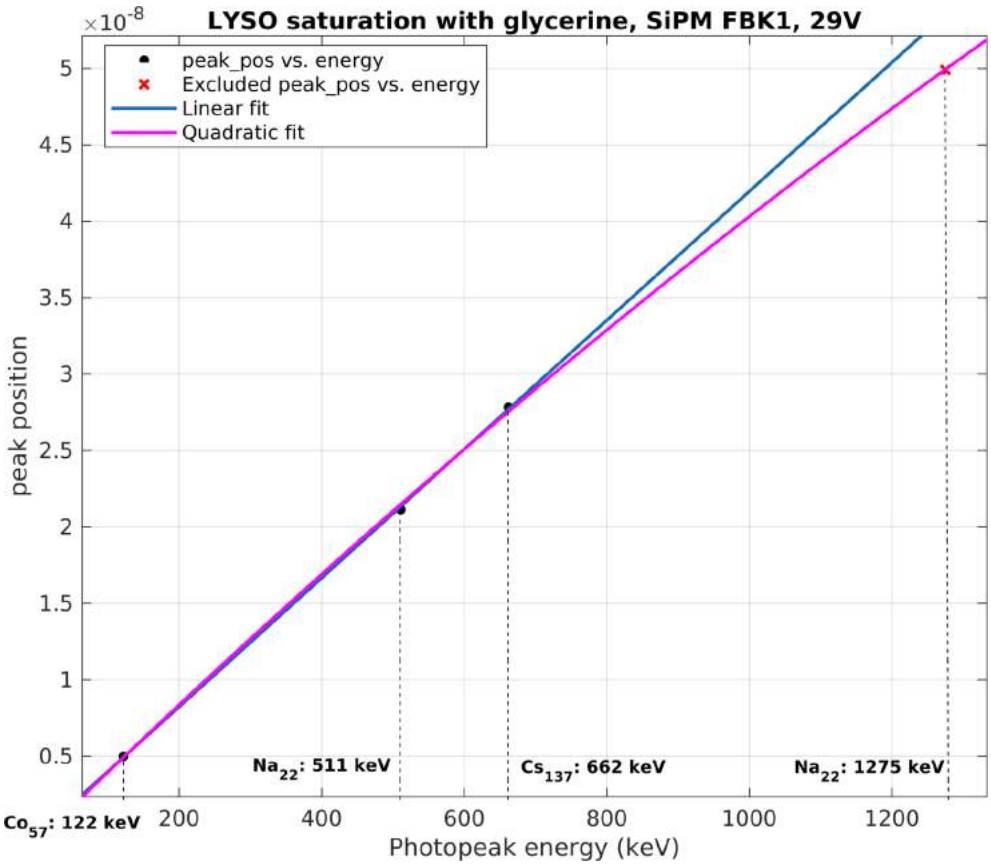

Figure 3.10: Saturation curve of the FBK NUV at 29V (∼2V overvoltage). Using this configuration with a Na_{22} source needs no saturation correction.

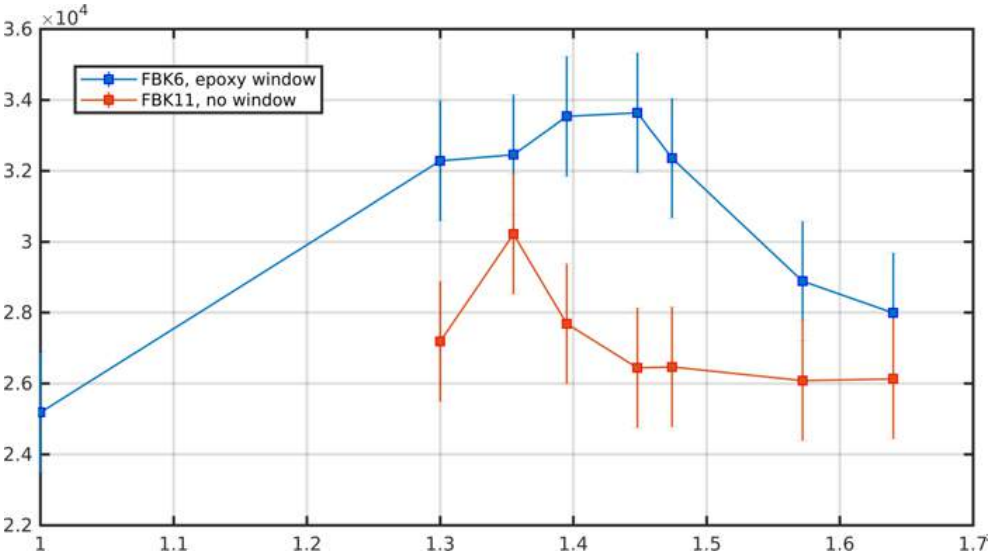

Figure 3.11: Measured and calibrated values of a Teflon wrapped $2 \times 2 \times 10mm^3$ LYSO crystal. The data were acquired with an FBK NUV at 29V.

as the smaller RI of all material in the detection chain before the photo-electron conversion. In our case, this was the optical window of the SiPM. Trying to remove this window, made of epoxy, did not improve the performance of the detection system because of a passivation layer deposited to protect the Silicon. Changing the material of this layer should improve the light extraction efficiency of the crystal but the potential gain is nevertheless marginal for LYSO crystals. GaGG crystals, with higher RI and longer emission wavelength, offers higher benefits: more light is trapped inside the scintillator and the yellow emission gives more flexibility when it comes to choosing an optical coupling with the suitable cut-off.
Future work will involve the tuning of the SiPM production towards higher RI coupling and test for GaGG crystals. Improvements of 20.6% are expected, which could lead to enhanced energy and time resolution.

3.4 Conclusions

The work presented in this chapter allowed to identify the limit of state of the art scintillator detector. Starting from the material production, it was demonstrated how new promising materials are being developed and, although further optimizations in the growth process are needed, shows powerful scintillation properties. Once the material is produced or selected from the wide range of scintillator available on the market, geometries and read out configuration (optical coupling) can be optimized in order to tune the scintillation properties: good energy resolution can be reached scarifying sensitivity while the optimal optical coupling is usually lying close to the RI of the photo-detector window. Further optimization of the system scintillator/photo-detector is possible making a joint effort with the photo-detector producer: higher performances could be reached with higher RI index of the interface between the scintillator and, for instance, SiPM, reaching the limit of no critical angle and total extraction of the scintillating photons (except Fresnel losses). Other methods to increase the extraction efficiency will be investigated in the next chapter. going to the read-out configuration.

Bibliography

[1] Burger, A.; Rowe, E.; Groza, M.; Morales Figueroa, K.; Cherepy, N. J.; Beck, P. R.; Hunter, S.; Payne, S. A. Cesium Hafnium Chloride: A High Light Yield, Non-Hygroscopic Cubic Crystal Scintillator for Gamma Spectroscopy. Appl. Phys. Lett. 2015, 107, 143505.

[2] (23) Maniv, S. Crystal Data for Cs 2 HfCl 6 . J. Appl. Crystallogr. 1976, 9, 245-245.

[3] (24) Ackerman, J. F. Preparation and Luminescence of Some K_2PtCl_6 Materials. Mater. Res. Bull. 1984, 19, 783-791.

[4] R. Král, V. Babin, E. Mihó ková , M. Buryi, V. V. Laguta, K. Nitsch, and M. Nikl: Luminescence and Charge Trapping in Cs 2 HfCl 6 Single Crystals: Optical and Magnetic Resonance Spectroscopy Study. JPCC. 2017.

[5] S. Gundacker, F. Acerbi, E. Auffray, A. Ferri, A. Gola, M.V. Nemallapudi, G. Paternoster, C. Piemonte and P. Lecoq: State of the art timing in TOF-PET detectors with LuAG, GAGG and L(Y)SO scintillators of various sizes coupled to FBK-SiPMs. JINST, 2016, doi:10.1088/1748-0221/11/08/P08008.

[6] S. Huber, W. W. Moses, M. S. Andreaco et al., "Geometry and surface treatment dependence of the light collection from LSO crystals," Nuclear Instruments and Methods in Physics Research A, vol. 437, pp. 374-380, 1999.

[7] K. Pauwels, E. Auffray, S. Gundacker et al., "Effect of aspect ratio on the light output of scintillators," IEEE Transactions on Nuclear Science, vol. 59, pp. 2340-2345, 2012.

[8] M. Sasano, H. Nishioka, S. Okuyama et al., "Geometry dependence of the light collection efficiency of BGO crystal scintillators read out by avalanche photo diodes,". Nuclear Instruments and Methods in Physics Research A, vol. 715, pp. 105–111, 2013.

[9] S. R. Cherry, Y. Shao, M. P. Tornai et al ., "Collection of scintillation light from small BGO crystals,". IEEE Transactions on Nuclear Science, vol. 42, pp. 1058- 1063, 1995.

[10] L. Bardelli, M. Bini, P.G. Bizzeti et al., "Pulse-shape discrimination with PbWO crystal scintillators," Nuclear Instruments and Methods in Physics Research A, vol. 584, pp. 129–134, 2008.

[11] C. Carrier and R. Lecomte, "Effect of geometrical modifications and crystal defects on light collection in ideal rectangular parallepipedic BGO scintillators,". Nuclear Instruments and Methods in Physics Research A, vol. 294, pp. 355-364, 1990.

4

Photonic crystals: Theory, simulations, production

4.1 Introduction

It was shown in the previous chapter how the number of photons trapped inside the crystal because of Snell's law can limit the energy and time resolution of the scintillation event detection. This chapter approaches the same problem making use of photonic crystals, which has the potential to decrease not only the critical angle but also the Fresnel losses at the interface between the scintillator and the photo-detector.
Since 1990, photonic crystals (PhCs) have been identified to be a versatile method to modify the way optical photons travel through a medium. The periodical structuring of the dielectric constant was found to offer control over the electromagnetic waves allowed to travel in the material, whenever the periodicity was on the same scale of the wavelength. The very first contribution to the underlying idea of PhCs was published by Yablonovitch [1], who formulated the theoretical basis of a forbidden band gap created by using a Fabry–Perot three-dimensional resonator with periodicity $\lambda/2$. Further studies led to an experimental probing of the photonic crystal band gap using microwaves [2]. The band structure was recorded performing a scan over different angles of incidence and frequencies impinging on the sample, and a band gap of unallowed wave vectors was observed. This knowledge opened the way toward a wide number of applications in the years to come:

- optical logic devices, using nonlinear effects that cause a dynamic shift in the location of the band gap. It was demonstrated first by Scalora in 1994 that this non-linear mechanism can induce intensity-dependent pulse transmission and reflection (optical switching, ON/OFF), together with pulse shape modulation [3]. This information can be used to build Boolean functions and perform logical operations.
- Sensors and biosensors that make use of shifts of the PhC micro-cavity resonant frequency [4].
- Photonic crystal fibers. Many unique properties are associated with a structured fiber, such as single-mode operations over a wide wavelength range [5] and over a very large mode area [6].
- Laser application; again micro-cavities, but filled with laser active material [7].
- Photonic crystal lasers for a single-photon source [8].
- Efficient photovoltaic devices with one-dimensional and two-dimensional photonic crystal patterns [9].
- Photonic crystal waveguides [10] and nanophotonic circuits [11].
- Light extraction from LEDs [12] and inorganic scintillators, making use of a PhC slab as a diffraction grating.

The work presented here will focus on the last application listed and more specifically on how PhC slabs can be applied to inorganic scintillators to improve energy and time resolution.

PhC slabs are defined as thin layers with 1D, 2D or 3D periodicity of the dielectric constant, which can increase the light extraction efficiency from high refractive index media. Joannopoulus first showed in 1997 how this principle could be applied to LEDs, and the method was considered a valuable and more efficient alternative to texturing the readout face. Following this work, Borodinsky [13] gave the experimental confirmation of an extraction efficiency enhancement up to a factor of four, using a triangular pattern of holes coupled to a glass substrate. The PhC slab was found to both enhance spontaneous emission through the Purcell effect and increasing the extraction efficiency of emitted photons, otherwise trapped due to total internal reflection (TIR).
The Crystal Clear group [14] at CERN was the first to explore the possibility to use the same technology applied to inorganic scintillators, knowing that the presence of a critical angle due to high refractive index crystals was similar to the problem encountered with LEDs. First with Kronberger [15], followed by Knapitsch [16, 17, 18], an experimental method was developed to obtain the best photonic crystal slab for each application. Several other groups started to put efforts toward the same field, and many collaborations started to grow with the common objective of increasing the light output of high refractive index crystals. In the following sections, we will explain in detail the theory, simulation tools and results obtained, summarizing what has been accomplished for those approaching the field for the first time, as well as the questions that remain open.

4.2 Theory of Photonic Crystal Slabs

As already mentioned, PhCs are nano- or microstructured materials with a periodic dielectric function over at least one dimension. The properties of an electromagnetic (EM) wave traveling through the PhC can be modified by the presence of this periodicity, if certain conditions are matched. In the first part of this section, the theoretical framework needed to understand these conditions will be introduced, together with a detailed explanation about why PhC slabs can increase the number of scintillation photons extracted from a crystal. The discussion will then move on to the different kinds of PhC slabs available.

4.2.1 Basic Principles of Photonic Crystals: Towards Diffraction

A description of the effects produced by a PhC can be obtained by treating it as a simple diffraction grating. Whenever the periodicity is higher than half the wavelength, EM waves traveling across a periodic arrangement of (thin) dielectric material will be split over different diffraction orders. Diffraction intensities over the different orders can be evaluated by considering a field passing through a volume V made of a periodic distribution of scattering centers. The higher the density of electrons inside these centers, the higher the number of dipoles that oscillate under the influence of the EM field. This causes the field to bend, resulting in a different propagation direction. The formula describing the amplitude of this phenomenon-caused by a certain scattering volume V is [20]:

$$F = \int dV n(\mathbf{r}) e^{-i\triangle \mathbf{k}\cdot\mathbf{r}} \tag{4.1}$$

which is a function of the phase shift $\triangle k$, the electron density $n(r)$ and the distance $\mathbf{r}$ between the origin of an arbitrary coordinate system and the scattering center dV. It can be demonstrated that this integral is non-negligible only for $\triangle k = G$, with the G reciprocal lattice vector of the system. All the photons passing through this PhC will have a modified k-vector direction and will therefore exit the interface with an angle dependent on the periodicity of the system and the diffraction order m. This conclusion comes out naturally from a more rigorous explanation, which

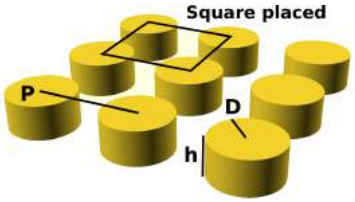

Figure 4.1: Example of a photonic crystal (PhC) slab with square-placed cylinders. The parameters defining such a geometry are the diameter of the cylinders D, the distance between the centers of consecutive cylinders P and the height of the structures h.

starts with the equation identifying the standing wave allowed to propagate inside a PhC:

$$\nabla \times \left(\frac{1}{\epsilon(\mathbf{r})} \nabla \times \mathbf{H}(\mathbf{r}) \right) = \widehat{\Theta}\mathbf{H} = \left(\frac{\omega}{c} \right)^2 \mathbf{H}(\mathbf{r}) \tag{4.2}$$

which is a reformulation of Maxwell equations called the master equation. ω is the frequency of the incident field; c is the speed of light; and ϵ the dielectric constant of the PhC material. For a detailed explanation about how to derive it, refer to [10, 20]. This eigen-value problem can be solved for a specific structure ϵ, which defines the theta operator ($\widehat{\Theta}$), in order to obtain the modes available $\mathbf{H}$. We can then insert $\mathbf{H}$ into:

$$\mathbf{E}(\mathbf{r}) = \frac{i}{\omega \epsilon_0 \epsilon(\mathbf{r})} \nabla \times \mathbf{H}(\mathbf{r}) \tag{4.3}$$

to obtain $\mathbf{E}$ [10] and have a complete description of the eigen-modes available in our system. These modes provide us with everything we need to know about the PhC, and the following will give an example about what we can do with this information.

4.2.2 Bloch Modes and Equi-Frequency Diagram

Consider a simple 2D grating of pillars placed in a square lattice, surrounded by air, as the one depicted in Figure 4.1. The symmetries of the system are the key to understand most of the PhC slabs' properties. Our system shows two main symmetries: discrete translational symmetry over x and over y for discrete steps of $\mathbf{R} = la\hat{\mathbf{x}}$ and $\mathbf{Q} = la\hat{\mathbf{y}}$, with l an integer number. Whenever a symmetry is found for the system, its operator commutes with the theta operator of the master equation, and this means that they share a common eigenspace: each simultaneous eigenfunction of the symmetry operators is, therefore, an eigenfunction of the theta operator. Solutions of the master equation using the translation operator are much easier to find than for the theta operator in Equation (4.2). These solutions are standing waves known as Bloch modes:

$$\mathbf{H}(\mathbf{r}) \propto e^{i\mathbf{k}\cdot\mathbf{r}} \mathbf{u}_\mathbf{k}(\mathbf{r}) \tag{4.4}$$

A Bloch state is an EM field inside the structures coherently scattering with itself. Because of the periodic form of Equation (4.4), Bloch modes with $k_b = k + bm$ have the same eigenvalue for Equation (4.2). These modes form a degenerate set of the system, which is the key factor for the diffraction orders to rise. The eigenfunctions of this degenerate set correspond to the same state, with the same eigenvalue and same frequency, and photons impinging on the PhC slab with an allowed $k_{||}$ can couple to any of the other $k_{||} \pm 2\pi/a$.

This periodicity implies also that we can confine our mode analysis to only the so-called irreducible Brillouin zone since we expect periodic solutions for the rest of the pattern area. We can describe the irreducible Brillouin zone as the smallest

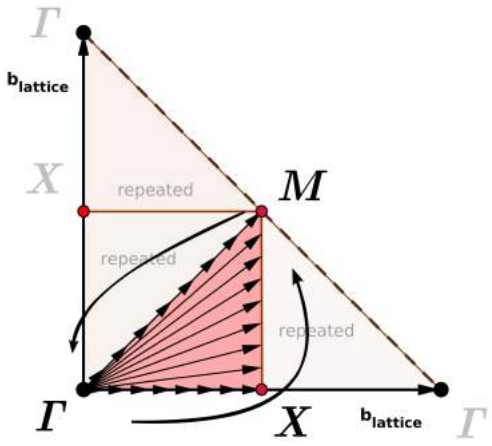

Figure 4.2: Irreducible Brillouin zone (pink area) of the square pattern shown in Figure 4.1. The arrows represent the k-vector projections in the plane of the PhC slab periodicity. For each k-vector, the allowed frequencies are calculated (there will be one frequency for each mode), obtaining the band diagram of the system (see Figure 4.3). The light pink areas, marked as "repeated", are just a replica of a rotated and translated irreducible zone; therefore, no additional information can be extracted examining these areas.

possible area over which solutions of the master equation are not redundant. We introduce here the concept of reciprocal space: a vector with component a_x, a_y, a_z becomes a reciprocal vector with components b_1, b_2 and b_3:

$$b_1 = 2\pi \frac{a_y \times a_z}{a_x \cdot a_y \times a_z}, \quad b_2 = 2\pi \frac{a_z \times a_x}{a_x \cdot a_y \times a_z}, \quad b_3 = 2\pi \frac{a_x \times a_y}{a_x \cdot a_y \times a_z} \tag{4.5}$$

For a square lattice, the new coordinates will be $k_x = 2\pi/x$ and $k_y = 2\pi/y$. We can cover the entire reciprocal space repeating the irreducible Brillouin zone, mirroring and translating it. Figure 4.2 shows the irreducible Brillouin zone for the simple geometry of Figure 4.1. To simplify the situation, even more, one could define a certain path of the $k_{||}$ vector over the irreducible Brillouin zone. It is a widely-used technique to follow the border of the irreducible Brillouin zone starting with a $k_{||} = 0$, following to M and then X, as indicated by the arrows in the picture. This method allows one to show much information using just one two-dimensional graph, similar to the one shown in Figure 4.3, called a band diagram. This amount of information is unfortunately not enough if working with a wavelength smaller than the periodicity, which is our field of application. In this case, an analysis extended to the region as big as the wave-vector of the incoming radiation is needed and spans over all the possible kx, ky, ω combinations. In the case of PhC slabs, there is no periodicity over k_z. We will, therefore, consider an iso-frequency diagram, or equi-frequency contour (EFC), like the one shown in Figure 4.4. This plot shows one single mode as a color map of the allowed ω in the $k_x - k_y$ plane. k_x and k_y are the components of the k-vector of the incident photon for which the symmetries explained at the beginning of the section apply. As already said, we can couple to any of the degenerate modes that have $k_{||} = k_i nc \pm mG$, with $G = 2\pi/a$ and $a = 1/Period$, so we will need to extend the region of interest to a few more reciprocal lattice points. An example of the area needed superimposed with the so-called Ewald construction is shown in Figure 4.5. The periodicity of the first mode is clearly visible over k_x and k_y.

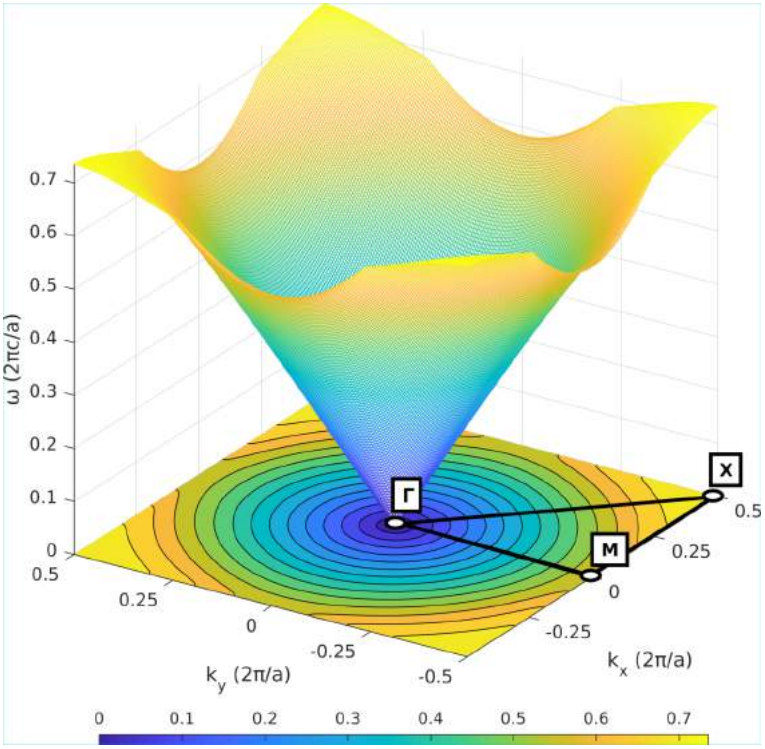

Figure 4.4: Equi-frequency contour (EFC) diagram of the structure depicted in Figure 4.1. The reciprocal lattice points show the position of the irreducible Brillouin zone, described in detail in Figure 4.2. The 3D curve shows the first Bloch mode of the system.

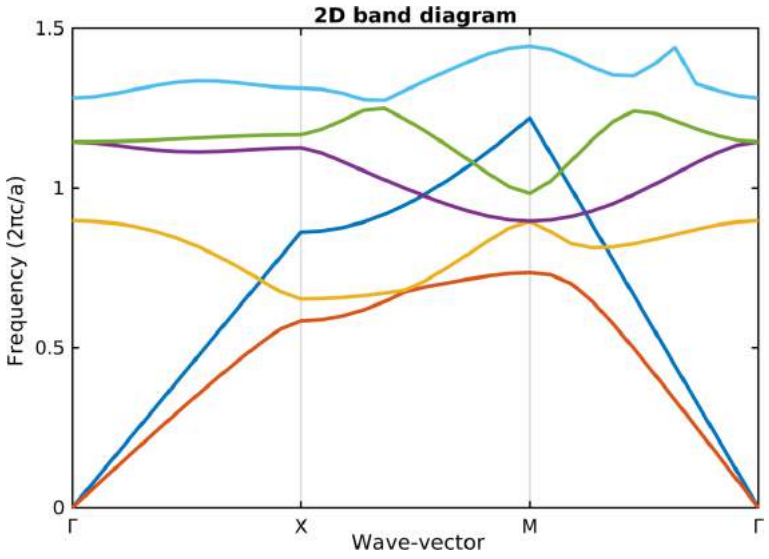

Figure 4.3: Band diagram of the structure depicted in Figure 4.1. Each color represents a different Bloch mode.

Each photon with defined direction and frequency may intercept one of these standing waves, being then able to couple to the modes of the degenerate set with a certain probability. These probabilities have a non-trivial evaluation, and simulation tools are needed to calculate them, as we will explain in the next section. Once the photon interacts with the PhC slab, the extraction parameters will be modified from the one expected using Snell's law. Consider a k-vector version of Snell's law

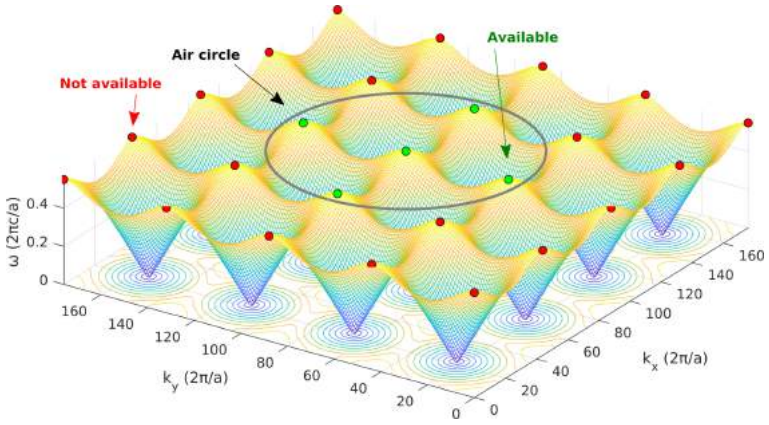

Figure 4.5: Ewald construction superimposed on the first Bloch mode of the system, shown for many periods of the system. For an incoming wave coupling to the central green point, several other degenerate states are created: those lying inside the air circle will be transmitted outside the medium (green point), while the others will be reflected back (red point), because of the too large $k_{||}$ (see the text and Figure 4.6).

(Figure 4.6):

$$n_{inc}k_0 \cdot sin(\theta_{inc}) = n_{out}k_0 \cdot sin(\theta_{out}) \tag{4.6}$$

This can be reinterpreted as a $k_{||}$ conservation rule: $k_{out||} = k_{inc||}$. The following notation is used: $k_{inc} = n_{inc}k_0$ and $k_{out} = n_{out}k_0$; the subscript $||$ will always indicate the vector component parallel to the interface. It is now possible to introduce the effect of the degenerate set $\pm mG$. Depending on the mode number, photons will be bent to an angle dependent on the initial properties of the incoming photons and the PhC slab parameters:

$$k_{out||} = k_{inc||} \pm mG \tag{4.7}$$

$$\theta_{out} = sin^{-1}\left(\frac{1}{k_0} \cdot |k_{inc||} \pm mG|\right) \tag{4.8}$$

where we have assumed $n_{out} = 1$ for air as the surrounding medium. This last equation is named after the physicist Von Laue, who first introduced the idea of wave vector coupling dependent on the reciprocal lattice point (Laue condition).
The length of the k-vector has to be constant for energy conservation. This is simply understood taking into account that the frequency of the dipole emission generated by the electrons should match the incident frequency. An additional formula is then required to redefine the component perpendicular to the surface:

$$k_{\perp} = \sqrt{n_{med}^2\omega^2/c^2 - (k_{in||}n_{sub} \pm mG)} \tag{4.9}$$

where n_{sub} is the refractive index of the substrate on which the PhC slab is applied and n_{med} the external medium. Notice that for negative values of m in the equation, photons with an angle bigger than the critical angle can be transmitted in the outside medium. This is the feature of PhC slabs that one would need to exploit in order to increase the extraction efficiency of inorganic scintillators. To visualize such an effect, a simple experiment was set up: Figure 4.7 shows the diffraction orders for a green laser impinging normal to an LYSO inorganic scintillator; the laser beam enters the flat, polished, back surface and reaches the front face where a PhC slab is imprinted. The main diffraction angle is shown in purple, while secondary orders coming from other symmetries of the system are shown in blue and red. Above the critical angle, half of these orders are still extracted from the scintillator.

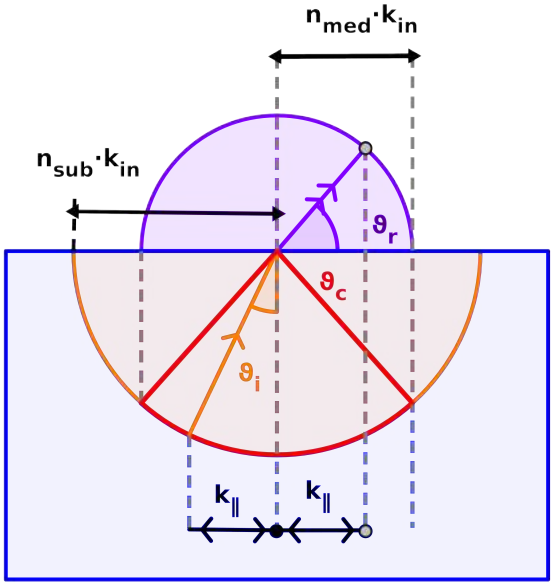

Figure 4.6: K-vector representation of Snell's law. The module of the incident wave vector is shown as an orange hemisphere, while the module of the outgoing wave is the purple one.

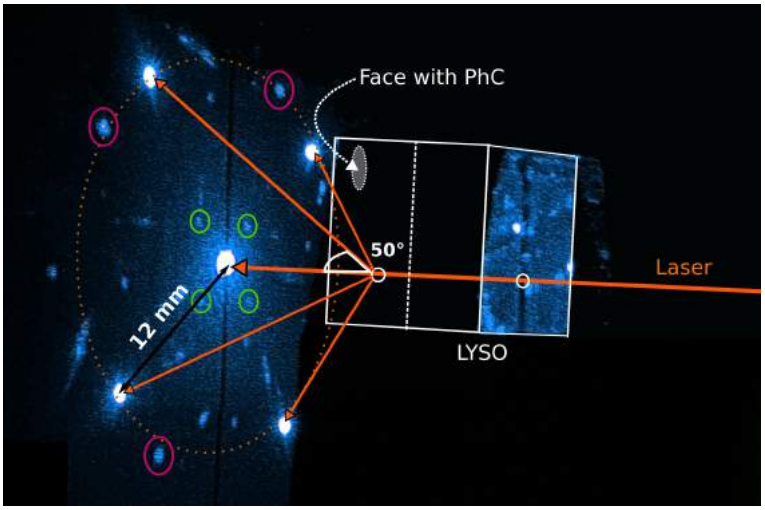

Figure 4.7: Experiment performed on an LYSO crystal with the PhC slab pattern on the readout face. A green laser is impinging from the face opposite the pattern, traveling inside the crystal and interacting with the PhC slab from the inside, as real scintillation photons would do. Diffraction orders are generated at an angle dependent on the periodicity of the pattern. The image is shown in false color to increase contrast.

4.2.3 Conical Structure: A Different Approach

Another method that can be used when trying to efficiently extract light from a high refractive index (RI) medium is to apply an anti-reflective coating. The purpose is to reduce Fresnel reflection under the critical angle, which can be achieved using sub-wavelength periodicity, $RI_{PhCslab} \sim RI_{cry}$, and high aspect ratio structures [21]. Unfortunately, working with periodicity smaller than the wavelength results in no degenerate states available inside the air circle (Figure 4.5), and this means that only the zeroth order will be transmitted outside the crystal: no diffraction will occur, and this can strongly limit the potential gain in light extraction. One possible way is to use conical PhC slabs in a regime of $P \sim \lambda$, with P period of the pattern, where diffraction still can take place, but also anti-reflection features show up. This particular topic will be treated in more detail in the Results Section 5.

4.2.4 Importance of the Refractive Index of PhC Slabs

Equation (4.1) shows the dependency of the amplitude on the electronic density. To fully exploit the diffraction behavior of PhC slabs, this amplitude has to be as high as possible, and besides the angular dependency (phase shift), this is dominated by the electron density. Materials that match this requirement are the ones with high RI. The formula describing the refractive index (n) is:

$$n = 1 + \frac{q_e^2}{2\epsilon_0 m} \sum_k \frac{n_k}{\omega_k^2 - \omega^2 + i\gamma_k\omega} \tag{4.10}$$

which shows a direct correlation between the RI and n_k, that is the density of electrons within a unit volume and with natural frequency ω_k. γ_k is the damping factor; q_e and m are respectively the charge and the mass of the electron, and ω is the frequency of the incoming EM field. Being able to use high RI materials for PhC slabs will then lead to stronger scattering amplitudes and therefore brighter diffraction orders.
Regarding the $i\gamma_k\omega$, when an EM wave of the form $E_{beforeSlab} = E_0 e^{i\omega(t-z/c)}$ travels through a non-patterned slab with damping factor γ_k and thickness Δz, the formula describing the field transmitted is:

$$E_{afterSlab} = \underbrace{e^{-\omega n"\Delta z/c}}_{\text{A}} \underbrace{e^{-i\omega(n'-1)\Delta z/c}}_{\text{B}} \underbrace{E_0 e^{i\omega(t-z/c)}}_{\text{C}} \tag{4.11}$$

where we have considered the RI to have the simplified form $n = n' - in''$, with real and imaginary independent components. The term C is the $E_{beforeSlab}$, modulated by a term B that just changes the phase of the wave. The term A describes a decrease in the amplitude of the field and increases with Δz and the damping factor γ, which is now hidden inside the n''.
This imaginary part of the index of refraction should be included in the simulations whenever absorbing materials are used to create PhC slabs. A widely-used instrument to measure the $n = n' + n''$ is the ellipsometer, and it has to be used in the case of non-perfectly transmitting materials.

4.3 Simulations

Different simulation tools were used to perform mode analysis of the structures (MPB), visualization of EM fields and diffraction orders' propagation directions (COMSOL), calculation of transmission efficiencies (CAMFR) and finally ray trace optical photons in the substrate, the PhC slab and the surrounding setup (Geant4). This section will introduce these software programs, giving a brief insight into how they work and explaining why they are useful in the PhC slab prototyping.
Some of these packages are freely available, and references are provided.

4.3.1 Cavity Modeling Framework

The cavity modeling framework (CAMFR, [22]) is a rigorous coupled-wave analysis tool (RCWA) that was developed by Peter Bienstmann during his Ph.D. It has a Python interface; therefore, it is easy to use and to modify, being a user-friendly programming language. It implements C, C++ and Fortran libraries to calculate EM field expansion: these libraries are fast and reliable and still are transparent to the user thanks to Python 'wrap' function.
The code is a frequency domain eigenvalue solver, which solves the master equation (Equation (4.2)) for source-free harmonic eigenfields. The volume of the system is discretized in a layered stack, and inside each layer, the scattering matrix method is applied for a given frequency [23] using the mode matching principle. This method was proven to be consistent with other finite-difference time domain (FDTD) methods [24], but being orders of magnitude faster for a large variety of structures. Moreover, spurious effects of numerical dispersion arising in FDTD are not seen in CAMFR.

4.3.2 MIT Photonic Bands

MIT photonic bands (MPB, [25]) is a free package released by MIT that computes full-vectorial 3D Bloch states, thus the eigenstates of the PhC slab. As CAMFR, it is a frequency domain software. The geometry is simulated in a finite element domain (FEM) layout, through the input interface for which the Scheme programming language is used. Having to simulate PhC slabs, which involves wave-guiding, this method is fast and reliable if compared to the standard FDTD method, which is based on time domain calculation: spurious effects of numerical dispersion arising in other techniques using FDTD are not seen with eigenfrequency expansion. MPB can be used to analyze the modes available in a certain dielectric, spanning over the entire irreducible Brillouin zone.

4.3.3 Geant4

Geant4 [26] is an open-source Monte Carlo simulator toolkit with a particle physics background. The main fields of application include high energy, nuclear and accelerator physics, as well as studies in medical and space science. It has been widely extended over the years to match the requirements of the community and today constitutes one of the most complete codes of its kind. This code was used for simulating gamma interactions, optical photon transport in the scintillator up to the intersection with the PhC slab and after the interaction with this surface, up to the photodetector. The steps that should be implemented while simulating the system are: the index of refraction of all the materials that could interact with the optical photons, as a function of the wavelength (crystal, surrounding medium, wrapping, optical coupling, photodetector); the crystal emission and absorption spectrum; the surface state of the crystal (σ_α parameter and reflection type selection; see Figure 4.8); the energy and direction of the incoming gamma rays, as well as the density of the scintillator (defines the stopping power); the reflectivity of the surrounding materials. Geant4 allows for an easy implementation of all these parameters. One drawback of using a Monte Carlo simulator is that optical photons are treated only as particles, and the program does not take into account photonic effects. See Section 4 for more details.

4.3.4 Combining Ray Tracing with RCWA Simulations

Once the scintillator is treated with PhC slabs, in order to simulate the complete system (crystal, PhC slab, and photodetector), a way to combine both ray-tracing information and photonic behavior was needed. Unfortunately, there is still no fast

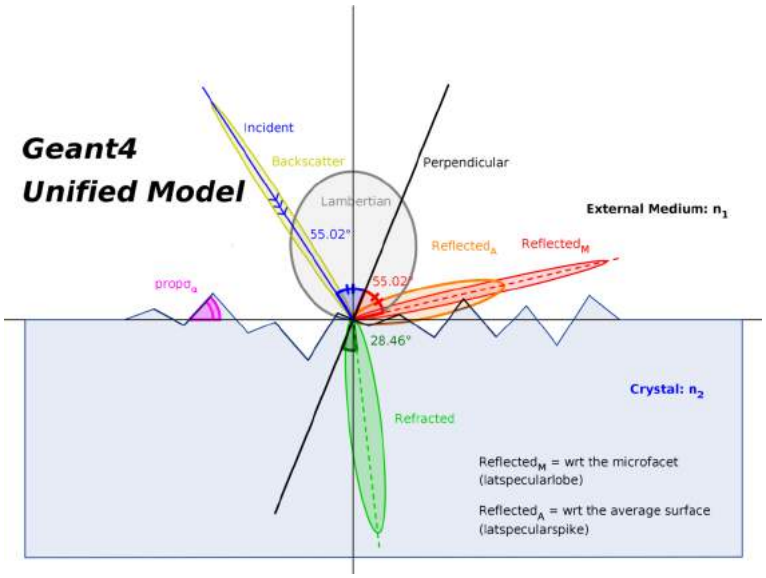

Figure 4.8: Representation of the UNIFIED model of Geant4, developed to describe optical interfaces between dielectric media with different refractive indices. One parameter that plays a central role is σ_α (pink angle). Every time an optical photon impinges on this surface, a random angle is picked from a Gaussian distribution: the sigma of this Gaussian is the σ_α. The surface, only for this specific photon, is no longer flat but tilted by this angle (micro-facet). The higher the σ_α, the higher the probability to have a big fluctuation of this modeled "roughness". The photon can be then reflected or refracted with respect to the new micro-facet (Geant4 parameter latspecularlobe, red lobe in the picture). Several other lobes are available in the UNIFIED model: Geant4 parameter latspecularspike, orange lobe, which describes the probability of reflection with respect to the original flat surface; Lambertian, grey lobe, which holds the probability of Lambertian diffusion; backscatter, light green lobe, is used to set the backscatter probability.

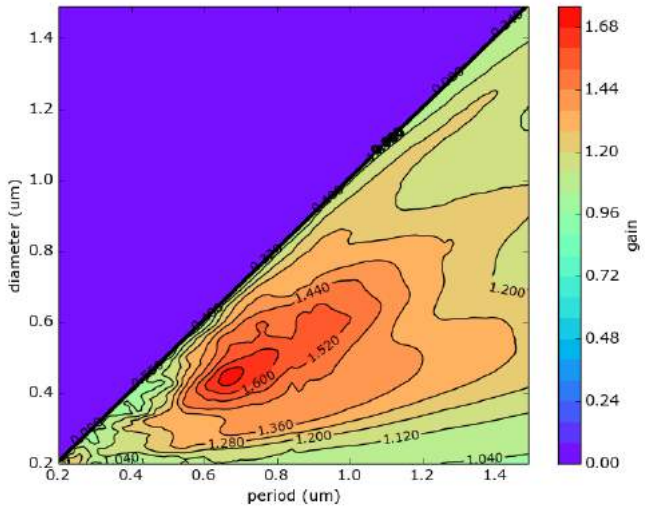

Figure 4.9: PhC slab optimization over the parameters period and diameter. The fixed parameters are: pillar shape, height = 300 nm, hexagonal placing, and air coupling [34].

and efficient method yet to implement an optimization with a single tool that merges these properties together. A possibility is offered by a combination of the separate tools CAMFR and Geant4, which can be used to optimize some of the system parameters to maximize the light extraction and energy resolution of the detector.
The angular distribution of the first incidence photons is initially generated by Geant4: only the first time a photon impinges on the readout face is counted since any other reflection will be affected by the presence of the PhC slab itself. The angular distribution is then used by CAMFR to optimize the pattern parameters, for instance, the period (P) and diameter (D) of the structures, and for a combination of transverse electric (TE) and transverse magnetic (TM) transmitted modes. Once the pattern optimized for the first incidence is determined, the transmission probability for each angle of incidence is given as an input to a Geant4 surface. The source code of Geant4 has to be modified to accept the output of CAMFR. Geant4 is now able to calculate the light yield (LY) gain for a given structure.
Below is a summary of the optimization steps required:

1. Simulation of the scintillator with a ray tracing program and calculation of the light angular distribution information. The number of gamma interactions to be used needs to be high enough to generate good enough statistics to produce a smooth distribution.
2. Run the PhC simulation tool to obtain the transmission of the light as a function of the impinging angle of the plane wave. Provide the angular distribution and calculate the transmission. Loop the simulation over different parameters in order to find the configuration that gives the higher light extraction efficiency.
3. Once the optimized configuration is found, implement the new transmission of the PhC surface into the scintillator + photodetector system. Run again the ray tracing simulation tool, now counting all the photons that enter the photodetector window, which is the value that can be compared with LY_out experimental data. A contour plot showing an optimization example of a photonic crystal pattern over a period and diameter is shown in Figure 4.9.

4.4 PhC Slab Production Methods

The progress in patterning techniques has been pushed by the micro- and nanoelectronics industry for decades. The first integrated circuit was printed in the 1960s using contact lithography. Afterwards, mostly optical projection lithography

was developed due to its high throughput. Furthermore, electron beam lithography techniques have been developed to provide the high resolution masks needed for optical lithography [35].
When the development of patterning techniques started, the patterns that could be produced were in the 10 µm scale. Nowadays, it is already possible to pattern structures smaller than 20 nm and with a high throughput [35].
Even though most of the processes in the nano-electronics industry are well developed and have a high throughput, the processes generally need adjustments when being used for imprinting scintillators. This can be either to solve problems intrinsic to the patterning process, such as the need for a conducting layer on a scintillator to be able to imprint with electron beam lithography, or practical issues with the equipment, such as samples that are much too high for the equipment that is developed for imprinting only several millimeters of thin silicon wafers. However, in principle, the techniques can be used for the purpose of producing nano-patterns on inorganic scintillators.
Nowadays, nano-patterning techniques are being developed for many different applications, introducing also more novel techniques such as patterning with scanning probes or by using self-assembly techniques.
While investigating nano-patterning techniques for the improvement of light extraction efficiency η_{coll}, the physical properties of the material that is to be imprinted play an important role.
Since the interaction of the pattern with the scintillation light is based on the electric potential created by the PhC slab, the extraction can be improved mostly by using materials that create a high electric potential, meaning a material with an as high as possible RI, as is explained in Section 4. Direct patterning of the scintillator itself is therefore usually not the best option, and preference is given to imprinting a so-called optical layer, consisting of a high RI material deposited on top of the scintillator. Examples of materials that can be used as high RI materials are Si_3N_4 and TiO_2. Another approach could be to create a photonic crystal pattern in a low RI material, for instance by directly patterning the scintillator, and afterwards, depositing a high RI material on top of the structure, for instance by using atomic layer deposition (ALD), to increase the effective RI of the pattern. Also in this case, Si_3N_4 and TiO_2 are good candidates as high RI materials. An example of using ALD to increase the effective RI of a pattern produced with polystyrene nanospheres, a technique explained in Section 4, is given in [37, 36].
Another characteristic is the optical transparency of the material. Since optical absorption of the material will decrease the amount of extracted light, it is preferred to use a material with a high optical transparency.
During this PhD work several patterning techniques were investigated to find the best match with the required physical properties of the PhC slab. In the following an overview of the knowledge acquired will be given together with some useful examples of produced PhC slabs.

4.4.1 Scanning Beam Lithography

Electron Beam Lithography

Electron beam (e-beam) lithography is a patterning process where no mask is needed. The machine, first used in 1960, had originally been developed from scanning electron microscopy [38].
The patterning is performed by exposing a layer of resist (deposited on top of the PhC slab material), which is an electron-sensitive medium in this case, with a focused electron beam. Depending on the chemicals used in the next step of the development, either the parts of the resist that are affected by the e-beam are washed or the parts that have not been exposed to the e-beam. Afterwards, the pattern is transferred to the final layer by using, for instance, reactive ion etching (RIE) [38].

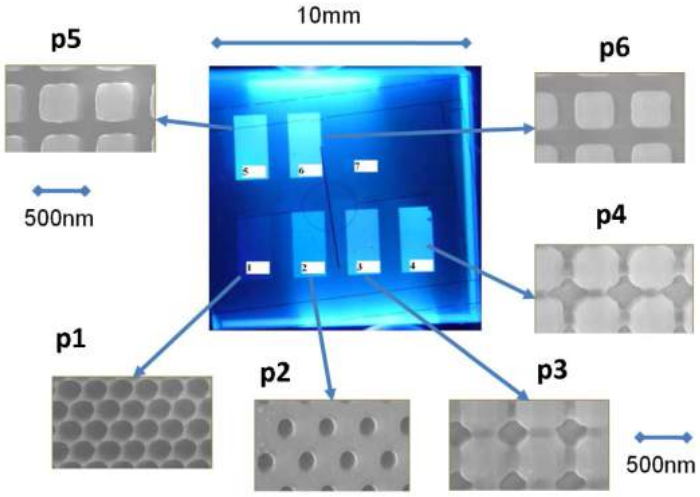

Figure 4.10: PhCs produced with e-beam lithography in Si_3N_4 on a scintillator [18].

The fact that e-beam lithography does not need a mask makes it a versatile technique. Furthermore, the resolution of this method is extremely high. Unlike optical lithography (see Section 4), in this case, the wavelength of the particles used for the pattering does not contribute significantly to the resolution. Depending on the resist and process parameters used, the accuracy can be higher than 10 nm [35].
Unfortunately, e-beam lithography is a patterning technique that is intrinsically very slow, making it extremely time consuming and expensive to use. The electrons are scattered by the space charge effect, and this effect is increased at higher currents, meaning that lower currents and therefore longer exposure times are needed for high-resolution patterning. Furthermore, the resist can only be exposed at the part where the e-beam is focused at that moment, and there is only one beam that scans the surface. This further limits the writing speed. In industry, the e-beam is therefore mainly used to produce masks for other lithography processes, which are then used many times. Attempts have been made to improve the patterning speed, by for instance introducing ways to have patterning with multiple beams from a single electron source. However, no real working example has been produced [35, 38, 40, 39]
As a result, the e-beam is a good technique to produce prototypes of photonic crystals on scintillators; however, it is not scalable to large surfaces. An example of photonic crystals produced with e-beam lithography is shown in Figure 4.10.

Ion-Beam Lithography

Also originating from the idea of scanning electron microscopy, ion-beam lithography is quite comparable to e-beam lithography, but instead of a beam of electrons, a beam of ions is used.
The benefit of using ions is that the resolution is not limited by the space charge effect. Therefore, the resolution can be higher compared to patterning with the e-beam, and the exposure time can be shorter. Furthermore, the resists used in ion-beam lithography are more sensitive, hence further reducing the required exposure times [41].
Ion-beams can also be used by directly patterning the desired layer of PhC slab, instead of using a resist. This means no additional steps and processes are necessary to obtain the pattern in the required layer [42]. This direct way of carving away the material is called milling and has historically been the main method used in ion-beam lithography [43].
Even though the exposure times in ion-beam lithography are lower compared to

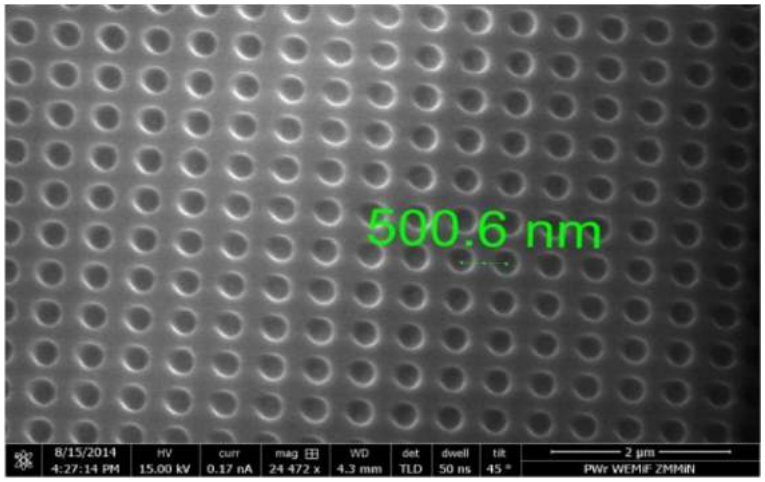

Figure 4.11: PhCs produced with focused ion-beam lithography, directly imprinted in the scintillator [42].

e-beam lithography for obtaining the same resolution, the patterning technique is still slow, therefore making it unsuitable for patterning large surfaces. Furthermore, the implantation of ions in the layer to be patterned can occur. Especially in the case of nanopatterns for improving light extraction, this can be a serious problem, since it can produce absorption in the material to be patterned [39].

An example of photonic crystals produced by direct milling of the scintillator is shown in Figure 4.11.

4.4.2 Optical Lithography

Optical lithography has been the main way to produce integrated circuits by the micro- and nano-electronics industry for decades. Therefore, it is well developed, in the sense of high resolution, but also high throughput.

Optical Projection Lithography

There are multiple techniques in optical lithography to perform the patterning. One of the basic principles is optical projection lithography. Here a mask, which is a copy of the final pattern, is used to project light of a certain wavelength on a photosensitive resist. After developing the resist, the pattern can again be transferred to the final layer through reactive ion etching. Figure 4.12 illustrates this imprinting technique.

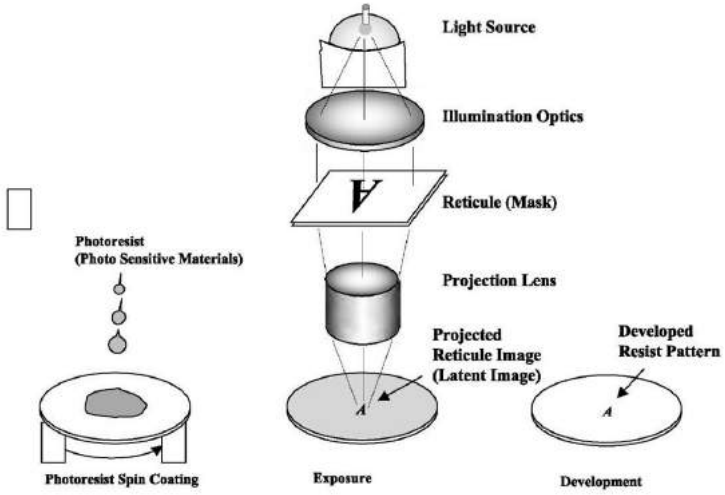

Figure 4.12: Schematic overview of optical projection lithography [44].

The resolution in optical lithography is mainly limited by the wavelength of the light and the numerical aperture of the system. Therefore, to increase the resolution, one tries to always go to shorter wavelengths and higher numerical apertures, while still maintaining a good depth of focus. Already in the 1990s, deep UV (DUV) patterning techniques were used in integrated circuit production, using wavelengths down to 193 nm. To be able to further increase the numerical aperture, immersion lithography has been developed, improving the resolution to about 40 nm. Very recently, techniques have been developed to use extreme UV (EUV) techniques, using a wavelength of 13.5 nm. With all the developments, it is nowadays possible to pattern structures with a resolution higher than 20 nm. The chemical development of the resist also has contributed to the continuous increase in resolution [35, 39, 43, 45].
Since the image of the mask is projected on the resist, a larger surface can be patterned all at once. This makes the technique much faster than for instance e-beam lithography, which was discussed in the previous Section 4. However, the production of the mask is expensive and time consuming since it has to be a high resolution mask that is usually produced with e-beam lithography. On the other hand, once the mask is produced, it can be used for a large amount of samples to be patterned. This can make the technique useful for large-scale production of patterned surfaces [39].

Optical Interference Lithography

In optical interference lithography, the final pattern is created by an interference pattern of multiple coherent beams, instead of using a complex mask. The interference pattern can be either created by a simple set of masks of gratings or without the use of a mask. This is illustrated in Figure 4.13. In this case, there is still the advantage of being able to imprint larger surfaces at a time, but it is not necessary to produce an expensive mask first. Furthermore, the optics used in interference lithography are much less expensive. The drawback of this technique however is that the possible patterns are limited to periodical patterns of lines or dots .
[39].

4.4.3 Nano-Imprint Lithography

Contrary to the patterning techniques discussed previously, nano-imprint lithography does not use radiation to imprint, but mechanical deformation by pressing a

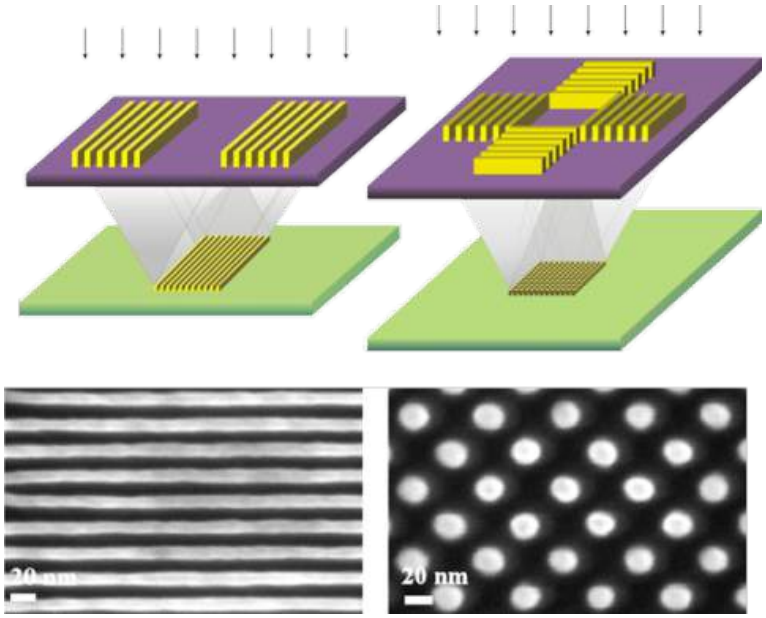

Figure 4.13: Schematic overview of optical projection lithography [46].

stamp into the material instead. Usually either heat or UV is used to cure the patterned material afterwards. Therefore, the main limitation for the resolution of the obtained material is the resolution of the stamp that is used. This is a benefit with respect to imprinting techniques based on radiation. Another advantage is the possibility to relatively easily produce 3D structures like pyramids or cones. Furthermore, the technique is fast, since a full surface of multiple centimeters can be imprinted at once. This makes the technique a scalable patterning process ([35, 39, 47]).

The imprinting can be used in two different ways. One possibility is to imprint a material and afterwards use it as a mask for etching, to transfer the pattern into the final material. An example of samples produced in this way is shown in Figure 4.14. It is also possible to directly stamp the pattern into the final material. If the pattern is used for light extraction enhancement of scintillators, either high refractive index polymers [48] or sol-gels [49] can be considered for direct imprinting. This means that an entire process step, transferring the pattern to the final material through etching, can be omitted [35]. Figure 4.15 shows a mask used for high refractive index polymer imprinting through UV-cured nano-imprinting.

The production of the mask or stamp, due to production time and costs, however, is probably the main drawback of this technique. The required stamp needs to have the same size as the surface that one wants to pattern, and the stamp needs to have at least the resolution of the final pattern. Furthermore, the mask cannot be used infinitely, since it will get damaged due to the contact with the substrate and at some point will have to be replaced. However, there are possibilities to make inexpensive replicas of a master stamp. Moreover, the patterning of large areas requires high power lasers [35, 39].

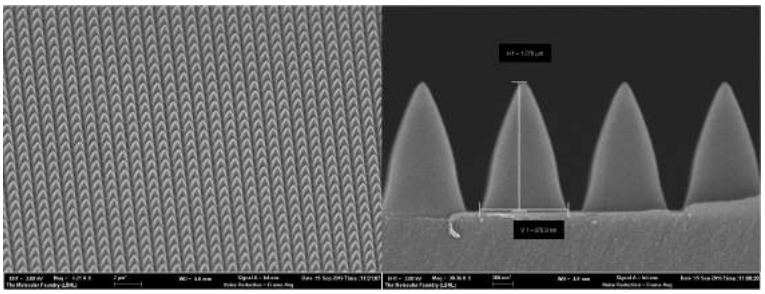

Figure 4.15: SEM image of the silicon mask for pyramidal pattern production [48].

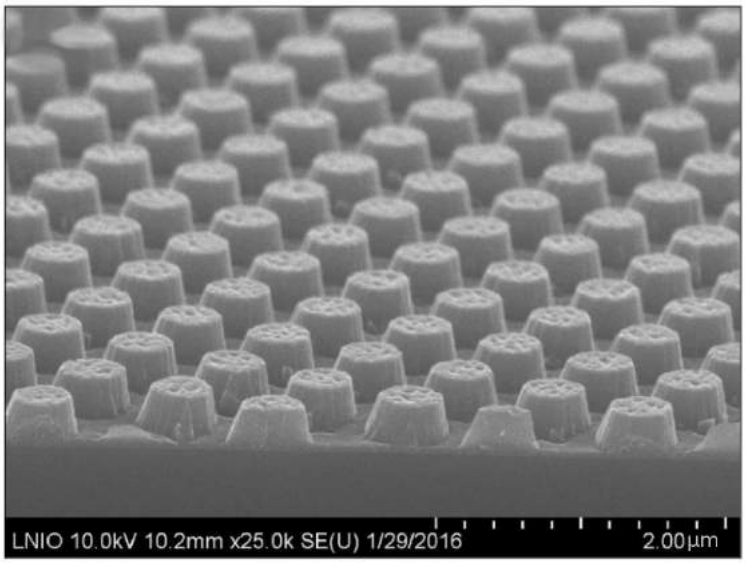

Figure 4.14: SEM picture of the TiO_2 PhC pattern [34].

4.4.4 Non-Conventional Lithography Methods

Nanolithography is a technique with much research and development. Therefore, the list of available or promising techniques, developed by numerous groups around the world, is large. We will quickly mention a few of them, but the list is certainly not exhaustive.

Self-Assembly

Self-assembly is an interesting field that investigates the spontaneous organization of nano-elements, either guided or non-guided. This is attractive in the sense that it gives rise to a relatively simple and cost-effective way to produce nano-structures. A technique to produce nano-structures that would be useful for light extraction enhancement in scintillators is colloidal lithography with polystyrene nano-spheres. First, a mono-layer of nano-spheres is deposited on the surface that needs to be patterned, usually through the Langmuir–Blodgett process [50]. This is a relatively simple method to obtain a mono-layer of nano-spheres that will arrange themselves in a hexagonal lattice. Afterwards, the layer is treated with a plasma, thereby shrinking the nano-spheres to the desired dimension [51, 52].
One approach is to deposit a layer on top of the nano-spheres, which afterwards will be used as a mask for an etching process. The nano-spheres are removed through

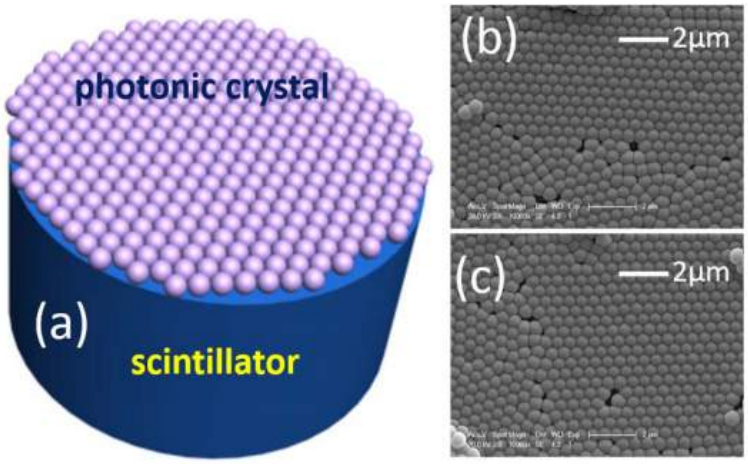

Figure 4.16: PhCs produced with self-assembly of polystyrene nanospheres and a deposited conformal layer of TiO_2. (**a**) Schematic illustration of the photonic crystal structures covered on the surface of scintillator. (**b**,**c**) SEM images of photonic crystal structures on the surface of LYSO Scintillators A and B, respectively [37].

lift-off, leaving behind a hard mask with hexagonally-placed holes, and an example is given in [51].

Another method is to use the nano-spheres directly as an etching mask, resulting in pillars in a hexagonal lattice. However, polystyrene nano-spheres are not very resistant to reactive ion etching (RIE), resulting in low aspect ratio structures. Therefore, the produced structure has to be treated to further grow the structures created, as is explained in [52], or nano-spheres of another material that is more resistant to etching techniques need to be used.

Another possibility is to directly use the deposited nano-spheres as photonic structures. For this option, nano-spheres made of a high refractive index material should be used, such as TiO_2. Alternatively, one can deposit a high refractive index material layer on top of the nano-spheres, such as TiO_2. An example is given in [37] and is shown in Figure 4.16.

The advantages of these techniques are that they are relatively fast and cost-effective, which makes it an attractive patterning option. However, it is clear that there is not much flexibility in the patterns that can be produced.

Another approach is to use anodization of a (layer of a) material, producing nanoporous material. This is a purely electrochemical process. The material is kept in an acidic solution while applying an electrical bias, resulting in self-ordered, nanometer-scale pores in the material. The processes of anodization of both aluminum oxide [54, 53] and titanium oxide [56, 55] are well studied. Since aluminum oxide does not have a high RI, RI = 1.76, for our application, it is useful to deposit a layer of, for instance, a higher RI material on top of the structure [53]. The challenge of the production process is to produce a homogeneous distribution of pores with diameters of about the same size.

This process is fast and low-cost, making it attractive for large surface patterning [53]. However, also with this method, there is little flexibility in the pattern design that can be produced.

An example of a PhC slab produced with nanoporous aluminum oxide is shown in Figure 4.17.

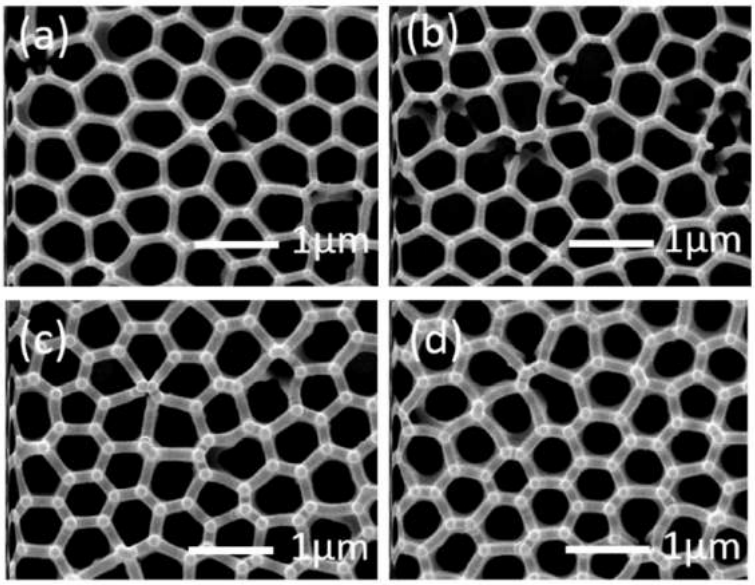

Figure 4.17: SEM images of (**a**) an anodized alumina oxide (AAO) layer; (**b**) an AAO + 10 nm Al_2O_3; (**c**) an AAO + 20 nm Al_2O_3; and (**d**) an AAO + 20 nm TiO_2 [53].

4.4.5 Scanning Probe Lithography

Scanning probe lithography is a technique where a probe is used to scan the surface and either add or carve away material on the surface. In this way, a nanopattern can be created with high resolution. Yet, like scanning beam lithography techniques, scanning probe lithography faces the challenge of throughput. The technique is limited by the time the probe needs to interact with the material it is patterning. As a result, it is not faster than for instance an e-beam. It is possible however to produce 3D structures with this technique. This would make the technique interesting for prototyping. An example of a commercially-available scanning probe lithography device is given here [57]. A difficulty in this case is to transfer the produced pattern in the resist used to an optical layer that is interesting for our application.

4.4.6 Multiphoton Lithography

Multiphoton lithography is a method where laser beams are used to directly imprint a photosensitive material. It is also possible to produce 3D structures. Usually, the produced structure needs to be coated with a high RI material, to be interesting for our application. An example of an industrially-available device is given in [58].

Bibliography

[1] Yablonovitch, E. Inhibited spontaneous emission in solid-state physics and electronics. *Phys. Rev. Lett.* **1987**, *58*, 2059–2062.

[2] Yablonovitch, E.; Gmitter, T.J. Photonic band structure: The face-cxentered-cubic case. *J. Opt. Soc. Am. A* **1990**, *7*, 1792–1800.

[3] Scalora, M.; Dowling, J.P.; Bowden, C.M.; Bloemer, M.J. The photonic band edge optical diode. *J. Appl. Phys.* **1994**, *76*, 2023–2026.

[4] Martiradonna, L.; Pisanello, F.; Stomeo, T.; Qualtieri, A.; Vecchio, G.; Sabella, S.; Cingolani, R.; De Vittorio, M. Pompa, P. Spectral taggin by inte-

grated photonic crystal resonators for highly sensitive and parallel detection in biochips. *J. Appl. Phys. Lett.* **2010**, *96*, 113702.

[5] Birks, T.A.; Knight, J.C.; Russel, P.S.J. Endlessly single-mode photonic crystal fiber. *Opt. Lett.* **1997**, *22*, 961–963.

[6] Knight, J.C.;Broeng, J.; Birks, T.A.; Russel, P.S.J. Photonic Band Gap Guidance in Optical Fibers. *Science* **1998**, *282*, 1476–1478.

[7] Englund, D.; Altug, H.; Fushman, I.; Vučković, J. Efficient terahertz room-temperature photonic crystal nanocavity laser. *Appl. Phy. Lett.* **2007**, *91*, doi:10.1063/1.2770767.

[8] Francardi, M.; Balet, L.; Gerardino, A.; Monat, C.; Zinoni, C.; Li, L.; Alloing, B.; Thomas, N.; Houdré, R.; Fiore, A. Quantum dot photonic crystal nanocavities at 1300 nm for telecom-wavelength single-photon sources. *Phys. Status Solidi* **2006**, *3*, 3693–3696.

[9] Celanovic, I.; O'Sullivan, F.; Jovanovic, N.; Qi, M.; Kassakian, J. 1D and 2D Photonic Crystals for Thermophotovoltaic Applications. *Photonic Cryst. Mater. Nanostruct.* **2004**, doi:10.1117/12.545539.

[10] Joannopoulos, J.D.; Winn, J.N. *Molding the Flow of Light*, 2nd ed.; Princeton University Press: Princeton, NJ, USA, 2008.

[11] Karachevtseva, L.A. Two-dimensional photonic crystals as perspective materials of modern nanoelectronics. *Semicond. Phys. Quantum Electron. Optoelectron.* **2004**, *7*, 430–435.

[12] Wiesmann, C.; Bergenek, K.; Linder, N.; Schwarz, U.T. Photonic crystal LEDs—Designing light extraction. *Laser Photonic* **2009**, 262–286, doi:10.1002/lpor.200810053.

[13] Boroditsky, M.; Krauss, T.F.; Coccioli, R.; Vrijen, R.; Bhat, R.; Yablonovitch, E. Light extraction from optically pumped light-emitting diode by thin-slab photonic crystals. *Appl. Phys. Lett.* **1999**, *75*, 1036.

[14] The Crystal Clear Group at CERN Is Part of the Crystal Clear Collaboration. Available online: `https://crystalclear.web.cern.ch/crystalclear/` (accessed on December 29, 2017).

[15] Kronberger, M.; Optimization of the Light Extraction from Heavy Inorganic Scintillator; Ph.D. Thesis, Vienna University of Technology, Wien, Austria, 2008.

[16] Knapitsch, A. Photonic Crystals: Enhancing the Light Output of Scintillation Based Detectors. Ph.D. Thesis, Vienna University of technology, Wien, Austria, 2012.

[17] Knapitsch, A.; Lecoq, P. Review on photonic crystal coatings for scintillators. *Int. J. Mod. Phys. A* **2014**, *29*, 639–643.

[18] Knapitsch, A.; Auffray, E.; Fabjan, C.W.; Leclercq, J.-L.; Letartre, X.; Mazurczyk, R.; Lecoq, P. Results of Photonic Crystal Enhanced Light Extraction on Heavy Inorganic Scintillators. *IEEE Trans. Nucl. Sci.* **2012**, *59*, 2334–2339.

[19] Lecoq, P. New crystal technologies for novel calorimeter concepts. *J. Phys. Conf. Ser.* **2009**, *160*, doi:10.1088/1742-6596/160/1/012016.

[20] Kittel, C. *Introduction to Solid State Physics*; John Wiley & Sons, Inc: New York, USA, 2005.

[21] Kasugai, H.; Nagamatsu, K.; Miyake, Y.; Honshio, A.; Kawashima, T.; Iida, K.; Iwaya, M.; Kamiyama, S.; Amano, H.; Akasaki, I.; et al. Light extraction process in moth-eye structure. *Phys. Status Solidi C* **2006**, *6*, 2165–2168.

[22] Moharam, M.G.; Pommet, D.A.; Grann, E.B.; Gaylord, T.K. Stable implementation of the rigorous coupled-wave analysis for surface-relief gratings: Enhanced transmittance matrix approach. *J. Opt. Soc. Am. A* **1995**, *12*, 1077–1086.

[23] Bienstmann, P. Rigorous and Efficient Modeling of Wavelength Scale Photonic Components. Ph.D. Thesis, Ghent University, Ghent, Belgium, 2001.

[24] Kim, J.; Hsieh, C.; Choi, H.J.; Gardener, J.; Singh, B.; Knapitsch, A.; Barbastathis, G.; Lecoq, P. Conical photonic crystals for enhancing light extraction efficiency from high refractive index materials. *Opt. Soc. Am.* **2015**, *23*, 22730–22739.

[25] Johnson, S.G.; Joannopoulos, J.D. Block-iterative frequency-domain methods for Maxwell's equations in a planewave basis. *Opt. Express* **2001**, *8*, 173–190.

[26] Agostinelli, S. Geant4—A simulation toolkit. *Nucl. Instrum. Methods Phys. Res. Sect. A* **2003**, *506*, 250–303.

[27] COMSOL Multiphysics® v. 5.2. COMSOL AB, Stockholm, Sweden. Availiable online: `www.comsol.com` . (accessed on 29 December 2017).

[28] Johnson, K.C. Grating Diffraction Calculator (GD-Calc)—Coupled-Wave Theory for Biperiodic Diffraction Gratings. 2008. Available online: `http://kjinnovation.com/GD-Calc.html` (accessed on 29 December 2017).

[29] Lumerical Inc. Available online: `http://www.lumerical.com/tcad-products/` (accessed on 29 December 2017).

[30] Liu, V.; Fan, S. S^4: A free electromagnetic solver for layered periodic structures *Comput. Phys. Commun.* **2012**, *108*, 2233–2244.

[31] Gentit, F.-X. Litrani: A General Purpose Monte-Carlo Program Simulating Light Propagation In Isotropic or Anisotropic Media. *Detect. Exp. Tech.* **2002**, *486*, 35–39.

[32] Zemax. Available online: `http://www.zemax.com/` (accessed on 29 December 2017).

[33] Cayouette, F.; Laurendeau, D.; Moisan, C. DETECT2000: An Improved Monte-Carlo Simulator for the Computer Aided Design of Photon Sensing Devices. *Appl. Photon. Technol. 5.* **2003**, doi:10.1117/12.474315.

[34] Zanettini, S.; Gâté, V.; Usureau, E.; Ruscica, J.; Hamouda, F; Nomenyo, K; Le Cunff, L.; Kadiri, H; Lerondel, G.; Salomoni, M.; et al. Improved Light Extraction Efficiency on 2 inches LYSO with Nanopatterned TiO_2 Photonic Crystals. IEEE Strasbourg 2016. Available online: `https://www.silsef.com/Documents.htm` (accessed on 29 December 2017) .

[35] Pease, R.F.; Chou, S.Y. Lithography and other patterning techniques for future electronics. *Proc. IEEE* **2008**, *96*, 248–270.

[36] Zhu, Z.; Liu, B.; Zhang, H.; Ren, W.; Cheng, C.; Wu, S.; Gu, M.; Chen, H. Improvement of light extraction of LYSO scintillator by using a combination of self-assembly of nanospheres and atomic layer deposition. *Opt. Soc. Am.* **2015**, *23*, 7085–7093.

[37] Liu, J; Liu, B.; Zhu, Z.; Chen, L.; Hu, J.; Xu, M.; Cheng, C.; Ouyang, X.; Zhang, Z; Ruan, J.; et al. Modified timing characteristic of a scintillation

detection system with photonic crystal structures. *Opt. lett.* **2017**, *42*, 987–990.

[38] Groves, T.R. 3-electron beam lithograph. In *Nanolithography*; Feldman, M., Ed.; Woodhead Publishing: Cambridge, UK, 2014; pp. 80–115.

[39] Gates, B.D.; Xu, Q.; Stewart, M.; Ryan, D.; Willson, G.C.; Whitesides, G.M. New approaches to nanofabrication: Molding, printing, and other techniques. *Chem. Rev.* **2005**, *105*, 1171–1196.

[40] Ito, T.; Okazaki, S. Pushing the limits of lithography. *Nature* **2000**, *406*, 1027–1031.

[41] Wanzenboeck, H.D.; Waid, S. Focused ion beam lithography. In *Recent Advances in Nanofabrication Techniques and Applications*; Cui, B., Ed.; InTech: London, UK, 2011.

[42] Modrzynski, P., Jr.; Gotszalk, T.; Knapitsch, A.; Kunicki, P.; Lecoq, P.; Moczala, M.; Papakonstantinou, I.; Auffray, E. Light extraction from scintillating crystals enhanced by photonic crystal structures patterned by focused ion beam. *IEEE Trans. Nucl. Sci.* **2016**, *63*, 644–648.

[43] Utlaut, M. 4-focused ion beams for nano-machining and imaging. In *Nanolithography*; Feldman, M., Ed.; Woodhead Publishing: Cambridge, UK, 2014; pp. 116-157.

[44] Nanolithography: Length-Scale Limitations Part 1 (Nanotechnology); Available online: `http://what-when-how.com/nanoscience-and-nanotechnology/nanolithography-length-scale-limitations-part-1-nanotechnology/`; (accessed on 29 December 2017).

[45] Rice, B.J.; 2-extreme ultraviolet (euv) lithography. In *Nanolithography*; Feldman, M., Ed.; Woodhead Publishing: Cambridge, UK, 2014; pp. 42–79.

[46] EUV Interference Lithography; Available online: `https://www.psi.ch/lmn/euv-interference-lithography`; (accessed on 29 December 2017).

[47] Resnick, D. 9-nanoimprint lithography. In *Nanolithography*; Feldman, M., Ed.; Woodhead Publishing: Cambridge, UK, 2014; pp. 315–347.

[48] Salomoni, M.; Pots, R.; Lecoq, P.; Auffray, E.; Gundacker, S.; Paganoni, M.; Singh, B.; Marshall, M.; Nagarkar, V.V. Photonic crystal slabs applied to inorganic scintillators. *IEEE Trans. Nucl. Sci.* **2017**, *12*, 15.

[49] Letailleur, A.; Nomenyo, K; Mc Murtry, S.; Barthel, E.; Søndergård, E.; Lérondel, G. High order symmetry interference lithography based nanoimprint. *J. Appl. Phys.* **2011**, *109*, 016104.

[50] Blodgett, K. Films built by depositing successive monomolecular layers on a solid surface. *J. Am. Chem. Soc.* **1935**, *57*, 107–1022.

[51] Knapitsch, A.; Auffray, E.; Barbastathis, G.; Chevalier, C.; Hsieh, C.H.; Kim, J.G.; Li, S.; Marshall, M.S.J.; Mazurczyk, R.; Modrzynski, P.; et al. Large scale production of photonic crystals on scintillators. *IEEE Trans. Nucl. Sci.* **2016**, *63*, 639–643.

[52] Domonkos, M.; Izak, T.; Stolcova, L.; Proska, J.; Kromka, A. Fabrication of periodically ordered diamond nanostructures by microsphere lithography. *Phys. Status Solidi* **2014**, *251*, 2587–2592.

[53] Zhang, J.; Liu, B.; Zhu, Z.; Wu, Q.; Cheng, C.; Liu, J.; Chen, L.; Ouyang, X.; Gu, M.; Xu, J.; et al. Enhanced light extraction of LYSO scintillator by

photonic crystal structures from a modified porous anodized aluminum oxide layer. *Nucl. Instrum. Methods Phys. Res. Sect. A* **2017**, *864*, 36–39.

[54] Zhu, Z.; Liu, B.; Cheng, C.; Zhang, H.; Wu, S.; Gu, M; Chen, H.; Chen, L.; Liu, J.; Ouyang, X. Improved light extraction of LYSO scintillator by the photonic structure from a layer of anodized aluminum oxide. *Nucl. Instrum. Methods Phys. Res. Sect. A* **2015**, *786*, 1–4.

[55] Yu, X.; Li, Y.; Ge, W.; Yang, Q.; Zhu, N; Kalantar-zadeh, K. Formation of nanoporous titanium oxide films on silicon substrates using an anodization process. *Nanotechnology* **2006**, *17*, 808–814.

[56] Yu, X.; Li, Y.; Wlodarski, W.; Kandasamy, S.; Kalantar-zadeh, K. Fabrication of nanostructured TiO2 by anodization: A comparison between electrolytes and substrates. *Sens. Actuators B Chem.* **2008**, *130*, 25–31.

[57] SwissLitho, A.G. Producer of the NanoFrazor. Available online: `https://swisslitho.com/` (accessed on 29 December 2017).

[58] Nanoscribe GmbH. Available online: `https://www.nanoscribe.de/en/` (accessed on 29 December 2017).

5

Inorganic scintillators treated with PhC

5.1 Introduction

The first part of this results chapter will show the results obtained on samples used to tune the production processes and the simulations tools, in order to test the potential of PhC applied to inorganic scintillator. The discussion will then move on real case study, specifically two main topics that differs only from the optical coupling point of view: one will consider an application with dry coupling (air) between the scintillator and the photo-detector, while the second will consider high refractive index coupling ($RI =\sim 1.5$). Both the case are critical from different points of view, challenging the technology being proposed and giving the possibility to evaluate the critical aspects.

5.2 Nanoimprinted PhC on cubes

The production technique selected for the first samples attempts was nano-imprinting, being a fast and relatively inexpensive method. We tested two different materials which were identified as promising: TiO_2 and Si_3N_4, both produced in collaboration with the Silsef company, experts in PhC production. Both are common materials, widely used to produce nanoscale devices, they are transparent in most of the scintillating crystals emission spectrum and with a high RI: $TiO_2 = 2.4$ and $Si_3N_4 = 2.1$. The first sample tested is a $1.5cm^3$ LYSO crystal to be measured naked: no wrapping and no optical coupling. This simple configuration was selected to reduce the free parameters of the system (wrapping reflectivity, the interface between wrapping and crystal, optical coupling non-homogeneity in the PhCs groove), having, therefore, greater control over simulations and results obtained. This sample was used to test Si_3N_4 as the active diffracting layer. Simulations were performed to guide the production process and are shown Figure 5.1. A maximum gain of 1.76 was expected for a squared placed pillar configuration.
The challenge of imprinting such a large area ($2.25cm^2$) was achieved with a mold of holes produced by interference lithography, with P = 750 nm and D = 500 nm. The Aluminum hard mask after the mold opening is shown in Figure 5.1,b. The sample was etched and the Aluminum residual removed, resulting in the nano-imprint shown in Figure 5.2.

The PhCs parameters measured by the SEM analysis are P = 720 nm, D = 450 nm and height = 310 nm. The simulated gain expected with this PhCs parameters is 1.68.
The LY measurements were performed with the set-up described in 2. The pre-pattern characterization showed a LY of 6614 ph/MeV with $E_{res} = 15.3\%$, to compare with the post-pattern LY values of 8279 ph/MeV with $E_{res} = 13.0\%$. The LY gain is 1.25 and the E_{res} gain is 0.85. The discrepancy between the observed values and the simulations could be explained by the presence of a Si_3N_4residual

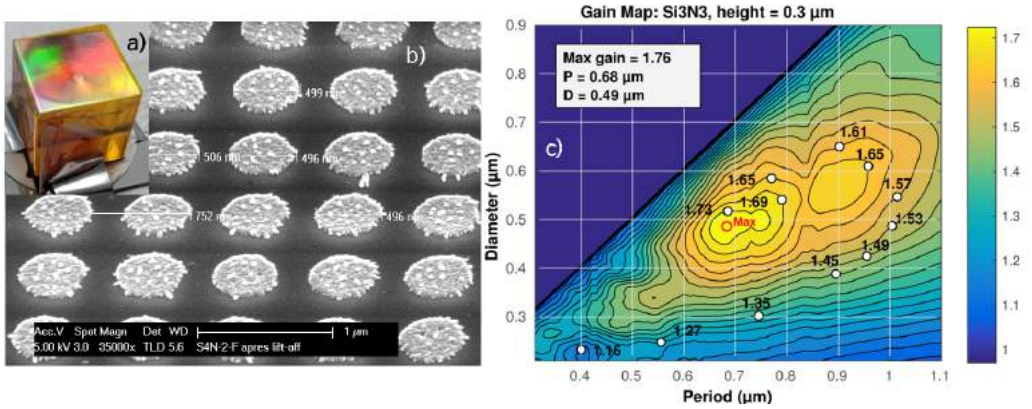

Figure 5.1: a) LYSO sample with imprinted readout face. b) hard mask Aluminum pillars lying above the Si_3N_4 layer, after mold opening. c) simulated optimization parameters for this crystal geometry(right). The maximum gain observed (first incidence configuration) was 1.76, for pillar in a square placed configuration (4.1) with P = 680 nm, D = 490 nm and height = 300 nm.

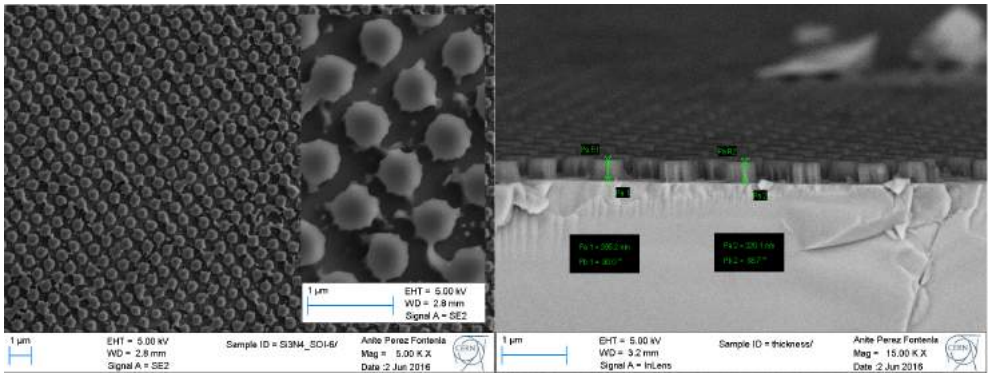

Figure 5.2: $Si3N4$ PhCs imaged by an SEM. On the left is a top view of the pillars while on the right a side view is shown. The pillars show some deviation from the cylindrical shape expected, probably related to the etching of the $Si3N4$.

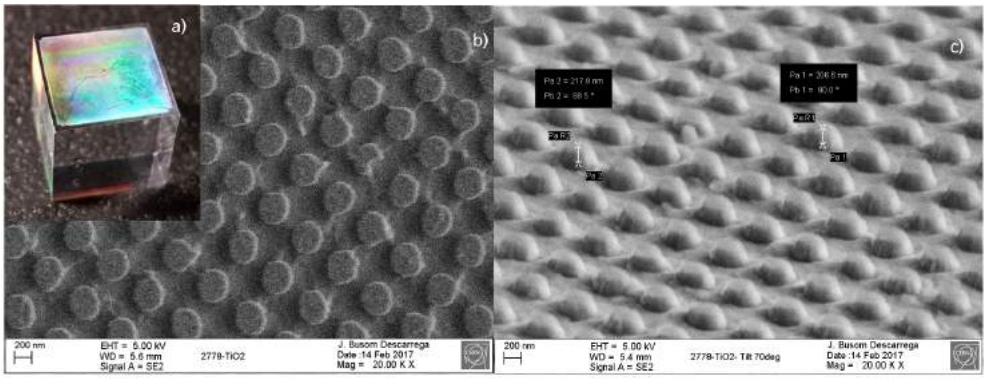

Figure 5.3: LSYO sample imprinted with TiO_2, $\#CPI2777$. a) shows the sample with the readout face facing upward and showing diffraction colors. b) SEM picture of the PhC, top view. c) SEM picture of the PhC, tilted view (70°).

layer between the pillar base and the LYSO surface, which could significantly modify the PhC structure, or by Al traces not removed by the etching step, which could absorb the LYSO scintillating light. Nevertheless, this result demonstrates the benefits of our approach to improving light extraction efficiency and consequently the E_{res} (eq. 1.4).
The samples selected for TiO_2 studies were 2 identical $1cm^3$ LYSO crystal, to be measured naked as for the Si_3N_4 sample. One sample was kept to compare the patterned crystal with a non-imprinted configuration (reference). The optimal simulated LY gain for TiO_2 square places pillars, for this crystal configuration, is 1.89 when P = 600 nm, D = 400 nm and height = 400 nm. The mold was produced with a P = 600 nm while the diameter can be tuned between 300 and 450 nm, changing the reactive ion etching time exposure during the final step of the imprinting.
The pattern imprinted on the readout face of one crystal is show in Figure 5.3. The imprinting is showing a strong border effect, related to the spin coating of the resist. The SEM analysis, performed on 3 images taken from 3 different readout face region, showed the following parameters: P = 580 nm, D = 390 nm, height 180 nm. The difference between the measured pillars height and the initial thickness of the deposited TiO_2 defines the thickness of the residual layer, therefore 220 nm.
Both CTR and LY measurements were selected for the TiO_2 pattern study. The CTR measurements were performed with a Hamamatsu SiPM of $6 \times 6mm^2$, $50\mu m$ SPAD size. The PMT set-up was modified to accept light only coming from an area of $6 \times 6mm^2$ using a mask, to allow a direct comparison between LY and CTR measurements. Results obtained with the PMT for the imprinted crystal and the reference are shown in Figure 5.4. The x-axis is shown in ADC channels, therefore not calibrated. The LY gain between the two configurations is 1.63 and the energy resolution gain is 0.79. The lower gain with respect to simulations is probably explained by the different parameters measured for the produced pattern. Two other configurations were tested, in order to study the influence of the PhC on the photon's path inside the crystal: PhC slab (PCS) facing away from the PMT and facing aside (Figure 5.5).

Table 5.1 summarizes the results obtained for LY and CTR in all the configurations. The CTR gain should follow the proportionality of equation 2.5, from which we should expect the CTR to go from 550 ps of the reference crystal to the 431 ps of the 3^{rd} configuration (Figure 5.5) of the patterned sample (facing the PMT). This value is compatible with the measured one (420 ps), considering the LY error of 2%. The configuration with the PhC facing backward with respect to the PMT is also showing gain comparable with the PhC facing the PMT. This is explained by the thick residual layer of the PhC, which enhance the reflective properties of the

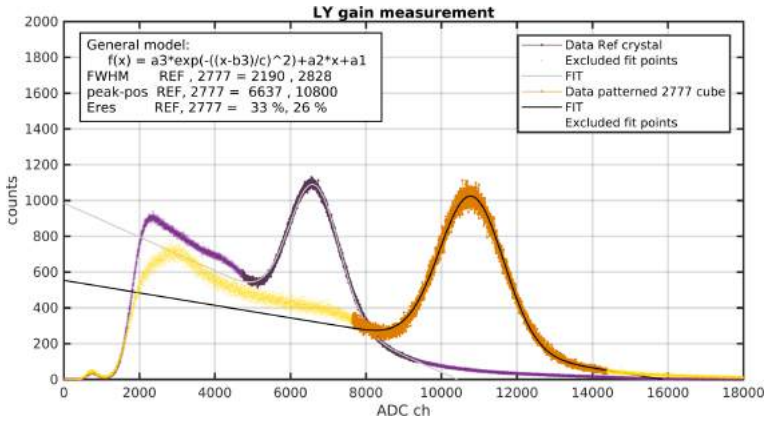

Figure 5.4: Spectrum comparison of the crystal imprinted with TiO_2 (orange curve) and the reference (purple curve). The data are fitted with the Gaussian model shown in the graph.

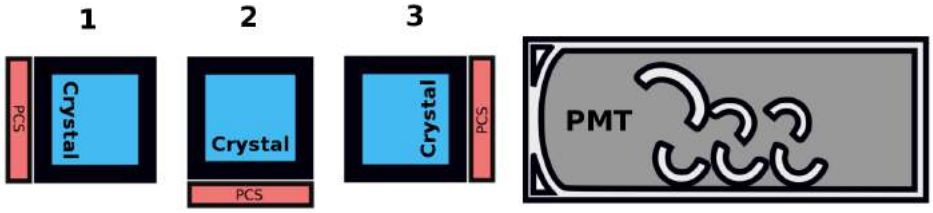

Figure 5.5: LY measurement configurations made with the PMT for the TiO_2 imprinted sample. Imprinted face facing opposite to the PMT (1), facing aside (2) and facing the PMT (3).

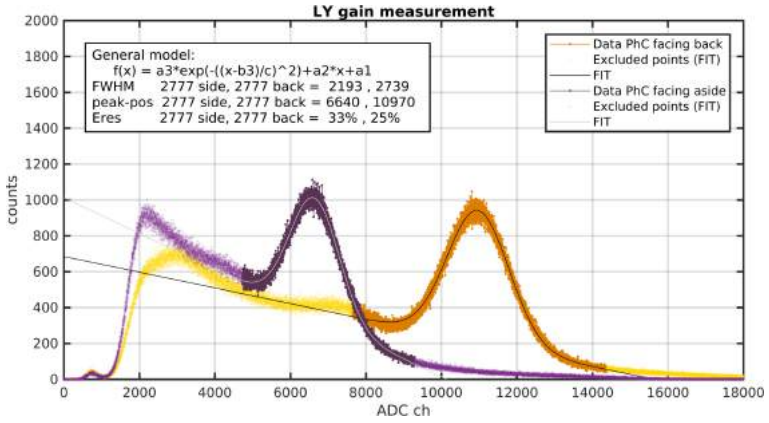

Figure 5.6: Spectrum comparison of the crystal imprinted with TiO_2, PhC facing aside (purple curve) and back (orange curve). The data are fitted with the Gaussian model shown in the graph.

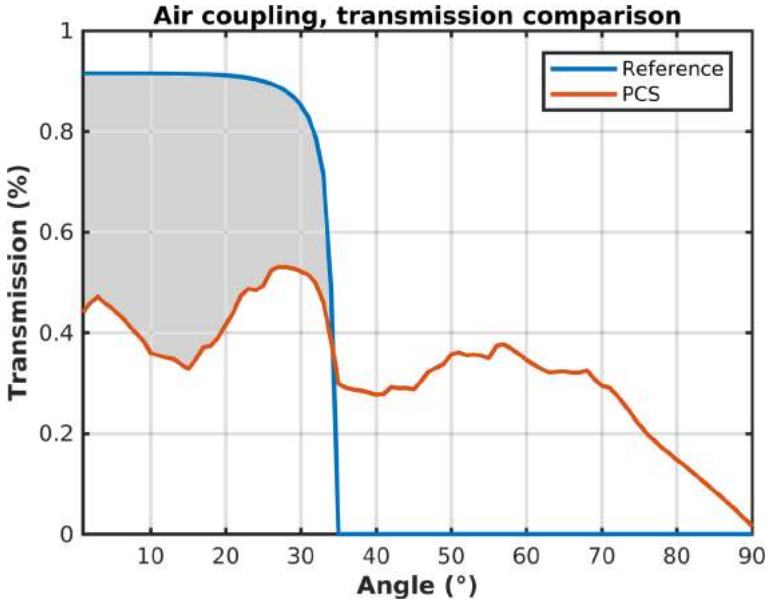

Figure 5.7: Simualtion of the PhC observed in Figure 5.3b,c. They grey area is the amount of photons reflected, which explains the LY gain observed reading out from the face opposite face to patterned face.

pattern, as explained in Figure 5.7.
As for the previous sample, this TiO_2 imprint was successful and show that the method proposed has the potential to enhance the light extracted from high refractive index scintillator. It was demonstrated that energy and time resolution improve accordingly, following eq. 1.4 and eq. 1.7. The production steps required to produce it are well understood for covering this readout surface dimensions with pillar-shaped features.

Table 5.1: CTR and LY measurements comparison for TiO_2 imprinted sample and reference crystal. The numbering of the patterned samples follow the explanation of Figure 5.5.

Sample	$LY(ph/MeV)$	E_{res}	CTR (ps)
patterned 1	10970	25%	410
patterned 2	6640	33%	500
patterned 3	10800	26%	420
reference	6637	33%	550

5.3 TurboPET project: PhC with dry coupling

The TurboPET project is a Eurostar funded project (#E8974) with the goal of upgrading a nuclear imaging dedicated breast PET system. This system integrates PhC at the interface between the scintillator and the photodetector for enhanced extraction of scintillation light.
The Eurostar programme request that within two years from the project completion the product of research should be ready for market introduction. In order to choose the most suitable system for a Eurostar project, several aspects had to be considered :

- impact of the technological achievement obtained, which for medical application translates (not only) in the possibility to perform clinical tests of the upgraded

Figure 5.8: TurboPET MAMMI system. a) Detectors ring dimensions of the plastic hole diameter (170 mm) and detector ring diameter (186 mm). b) shows the machine final layout and in c) the two detector rings together.

set up. A PET already CE and working is needed in order to do that. Clinical tests are the definitive goodness indicator used to compare with the rest of the market.
- potential gain obtainable with nano-structuration of the readout face.
- Technological limits: the dimension of the crystals, environment.
- Reproducibility, cost of the process, industrial scalability.
- Rapid commercialization as a follow up of the project.

The targeted application for the PhC implementation is the MAMMI, a dedicated breast PET for early mammary cancer detection and therapy treatment assessment, developed by the company ONCOVISION. The system is schematically represented in Figure 5.8: it is made of two separate rings of LYSO scintillators, dry coupled with position sensitive PMTs (PSPMTs). The crystals are of trapezoidal shape (Figure 5.9) and non-readout faces are depolished and black painted to allow a better reconstruction of the interaction point inside the scintillator volume. Each ring contains 12 crystals. The dry coupling configuration offers higher gain potential when PhC is applied: dry coupling means smaller critical angle compared to glue

coupling, and PhC additional diffracted modes are more likely to increase the extraction efficiency. Moreover, the use of two rings allows to nanopattern only one of the two and to compare the image acquired on the same patient at the same time. The minor technological difference of PhC application does not make the CE invalid, which leaves the door open to clinical tests without any further authorization. The dimension of the readout face being $5 \times 5cm^2$, the nanopattern was considered to be applicable for such an area using nanoimprinted lithography, as well as the final step towards industrial scalability.
The project was carried out in a wide consortium of collaborators, each of them responsible for a work package (WP*) and closely interconnected with the other WP group leaders.
Below is a short description of how the several WPs were organized.

- WP1: provide the simulation tool to evaluate the possible light extraction gain and estimate of the improvement in the MAMMI SNR. The WP leader is CERN.
- WP2: Quantify the gain and energy resolution improvement of the crystals for the several pattern parameters and suggest which of the different geometries and material should provide the best gain. The WP leader is the University of Technology of Troyes (UTT).
- WP3: Pattern a high index optical layer on LYSO, reproducibly and at low cost according to the patterns specifications. Furthermore, to develop a novel know-how of nano-imprint lithography (NIL) including direct embossing of the sol-gel layers. The WP leader is NAPA Technologies.
- WP4: Functional characterization of the scintillator crystals performances, such as light yield, energy, and spatial resolution. The WP leader is CERN.
- WP5: Integration of the nanopatterned ring in the TurboPET MAMMI scanner and tuning of the electronic to profit from the new performances. The WP leader is ONCOVISION
- WP6: Compare the two rings performances in a clinical setting for breast cancerous lesions and quantify the increase in sensitivity and resolution. The WP leader is the University Hospital of Vaudois (CHUV).
- WP7: Overall management of the project as to respect the initial planning. The WP is NAPA Technologies.

The following subsections will present details on the work packages where CERN was directly involved, i.e. WP2 and WP4, followed by an overall conclusion of the project outcomes.

5.3.1 Simulations [WP2]

The purpose of this work package was to provide the production experts (WP3) with expected light output gain for all the possible configuration of the pattern. The main parameters of the pattern were identified to be the feature shape (conical, spherical, cylindrical, cubical..), the shape parameters (e.g. for pillar shape: diameter, height, distance between different pillars (period)), the index of refraction and absorption of the material used as well as the feature placement (hexagonal or square placing). The scintillator crystal geometry and surface state can also influence the light output gain for a fixed pattern configuration, as it will be explained in more details below. This complex system required a multi-scale simulation approach, combining both ray tracing tool (GEANT4) and photonic simulations for diffraction(CAMFR), as explained in section 4.

Geant4: The crystal is a trapezoidal Lu_2YSiO_5 (LYSO) Cerium doped, with dimensions shown in Figure 5.9, depolished and black painted on the non-readout faces. The energy emission spectrum set for the LYSO is shown in Figure 5.10, with a peak around 420 nm, whereas the decay time and rise time of the scintillator have been set to 40 ns and 70 ps respectively. The intrinsic LY of the LYSO scintillator

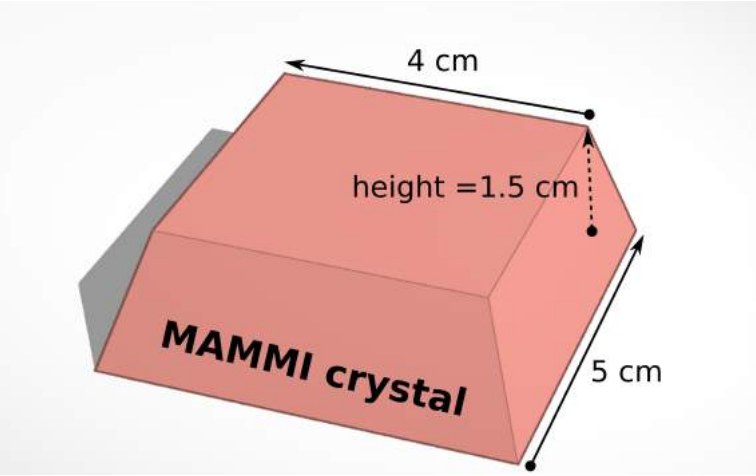

Figure 5.9: Energy dependency of the RI in an LYSO crystal.

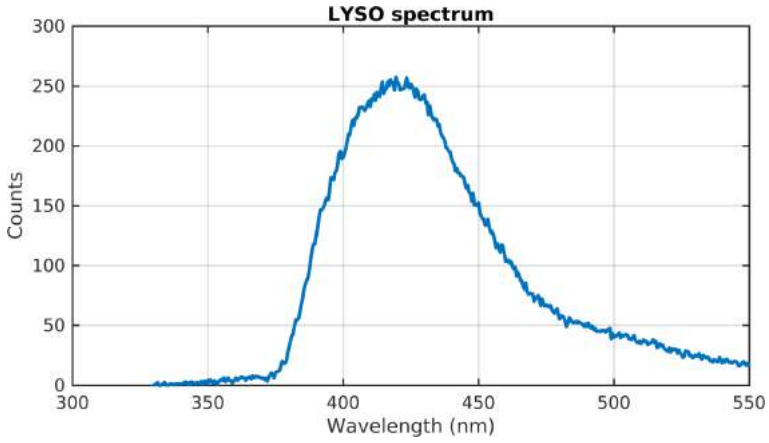

Figure 5.10: Emission spectrum of an LYSO crystal.

was set to 40000 ph/MeV [1], the absorption length was set as in Figure 5.11 and the RI as in Figure 5.12, according to previous measurements made by our group.

The black paint used to diminish multiple reflections, in favor of a better spatial resolution, is an acrylic spray paint, therefore modeled as a material with RI = 1.49 and measured transmission of 88% in the LYSO emission peak.
The Cs_{137} source was simulated as a point, isotropic source of 662 keV photons. The photodetector has the properties of the PMT used in the LY characterization bench, described in the WP4 section 5.
Two crystal configurations were tested in the LY bench in order to tune the simulated parameters. Completely naked and with black paint on the non-readout faces, which showed an LY of 9920 and 3770 ph/MeV respectively. These early-stage measurements were performed on a crystal (trapezoidal) with a height of 1 cm (ALBIRA crystal, PET scanner of an older generation) instead of 1.5 cm. The simulated values were tuned to the final values 9850 and 3595, which are compatible with the measurements considering the LY error of 2%. The choice of using smaller crystals did not influence the quality of the parameters chosen, as it was confirmed later on in the project.
The model was then used to extract the angular distribution that CAMFR needs in order to run an optimization of the PhC, shown in Figure 5.13.

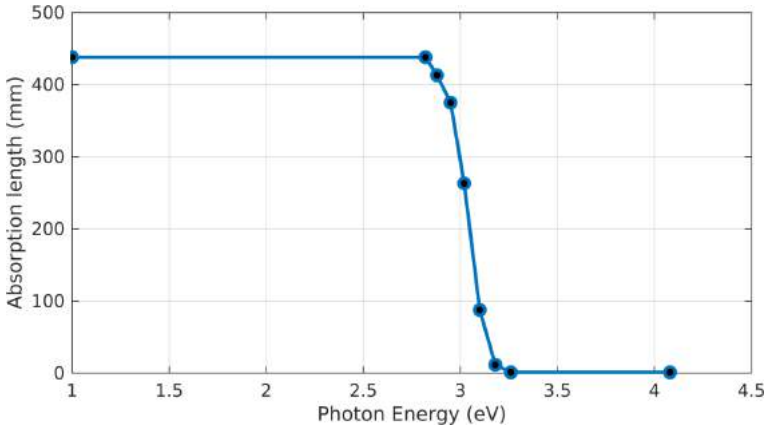

Figure 5.11: Absorption spectrum of an LYSO crystal.

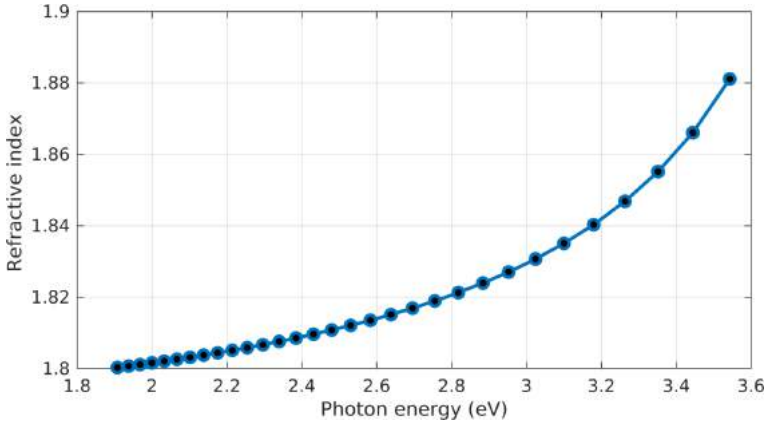

Figure 5.12: Energy dependency of the RI in an LYSO crystal.

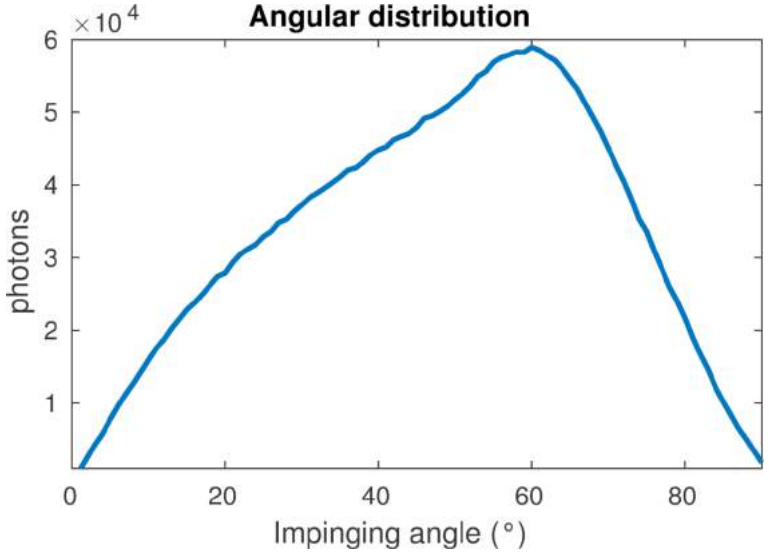

Figure 5.13: Geant4 output for a MAMMI crystal with black painted non-readout faces. The curve shows the angular distribution of the first incidence scintillation photons, which will be the input of CAMFR.

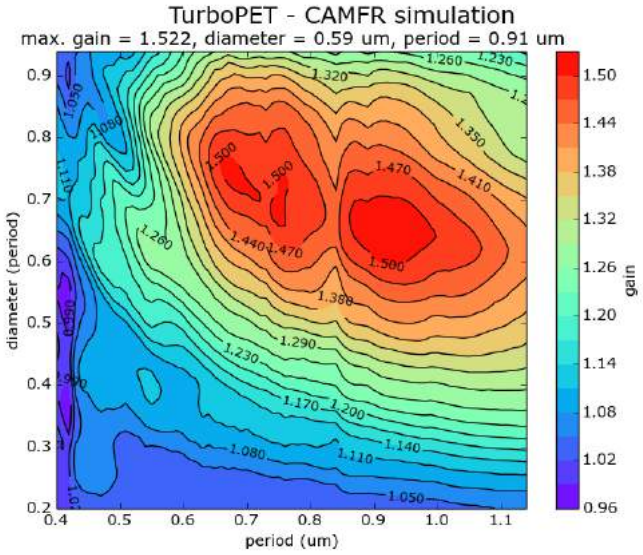

Figure 5.14: CAMFR output for the optimization of Si_3N_4 pillars patterned on MAMMI. The fixed parameters are pillars height = 300 nm, RI = 2.1, squarely placed. The diameter is expressed as proportional to the period.

CAMFR simulations: This part of WP2 was dedicated to the development of the PhC simulation. The purpose was to calculate the transmission probability when an electromagnetic wave is impinging on a plain or nanostructured surface, depending on the angle of incidence, wavelength, and RI of substrate material/coupling.
The rigorous coupling wave analysis (RCWA) tool CAMFR (Cavity modeling framework) was used. The substrate RI was set to the constant value of 1.82, the nanostructured layer was instead dependent on the material that the production WP3 was able to deliver with sufficient precision and reproducibility. These materials are Si_3N_4 (RI=2.1) and TiO_2 (RI=2.4). The imaginary part of the RI was set to 0, which is consistent with the very low absorption of both the materials in the LYSO emission region.
These two materials were first tested for a geometry already explored in the preliminary nanoimprinting studies (see 5), pillars in square lattice configuration (Figure 4.1), whereas the crystal configuration is the one that will be implemented in the ready-to-use PET machine, therefore black painted without optical coupling. The optimization output for Si_3N_4 is shown in Figure 5.14. A maximum of 1.52 is found for P = 910 nm and D = 590 nm.
Two different geometries were tested for TiO_2 as diffracting material. Together with the standard square placed pillars, circular holes in a square placed configuration were simulated, giving the results shown in Figure 5.15

A maximum of 1.71 is found for pillars geometry with P = 670 nm and D = 450 nm. For holes geometry the maximum gain obtainable is 1.4, with P = 670 nm and D = 450 nm. Pillars configuration has the potential to bring higher LY compared to holes and will be the only produced geometry between the two.
Another production technique was explored during the project, making use of Sol-Gel technology to grow TiO_2 cones. The mold in this case was produced by self assembly (SA) method, with a fixed period of $1\mu m$ and hexagonally placed features (micro sphere always self assemble in an hexagonal lattice). Simulations were run to investigate the parameter space of aspect ratio and RI of the TiO_2 cones. Two known geometries were already possible to produce, the first with RI = 1.8 (non perfect crystalline structure due to low annealing temperature), D = 600 nm and a height H = 1 μm; the second with RI = 2.4, D = 300 nm and H = 600 nm. The

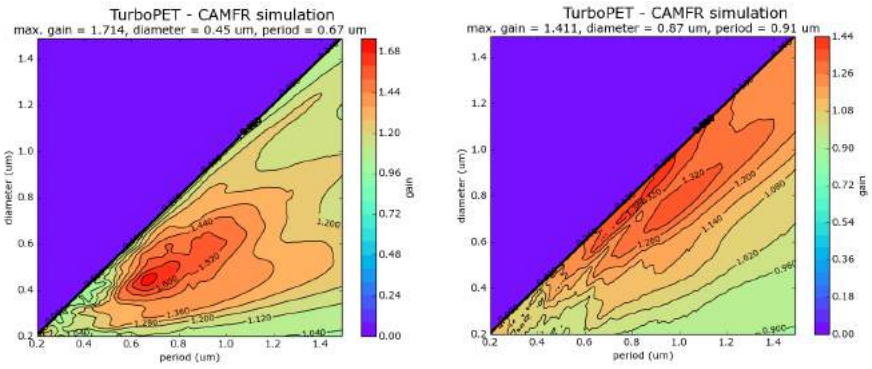

Figure 5.15: CAMFR output for the optimizatios of TiO_2 pillars patterned on MAMMI (left), and holes in TiO_2. The fixed parameters are pillars/holes height = 300 nm, RI = 2.4, square placed.

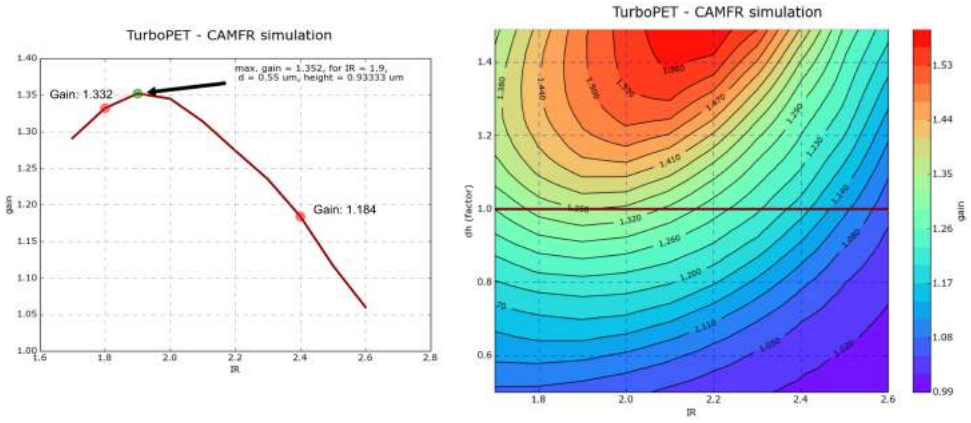

Figure 5.16: Correlation between RI and gain (left). Additional simulation with δh variation from linearity (right). The left simulation is presented again on the right for$\delta h = 1$.

hypothesis was that while reaching the good annealing temperature of the TiO_2, the cones shrink in dimension linearly with respect to this two extremes. The simulations investigated the LY gain for geometries with the following parameters:

$$\begin{aligned} P &= 1\mu m \\ D &= (1.8 - RI) \cdot (0.50 + 0.60) \\ H &= (1.8 - RI) \cdot (0.67 + 1.00) \end{aligned}$$

The maximum for this 1-D optimization was found for a RI = 1.9, which mean D = 550 nm and height = 930 nm, as shown in Figure 5.16, left. The simulation was also modified to accept a variation δh from the ideal linear expression:

$$\begin{aligned} P &= 1\mu m \\ D &= \delta h \cdot (1.8 - RI) \cdot (0.50 + 0.60) \\ H &= \delta h \cdot (1.8 - RI) \cdot (0.67 + 1.00) \end{aligned}$$

A new maximum was found for δh=1.49, RI = 2.2, which mean D = 302 nm and height = 603 nm, as shown in Figure 5.16, right. The maximum is limited to the δh upper bound, which suggest higher gain outside of the parameters space investigated.

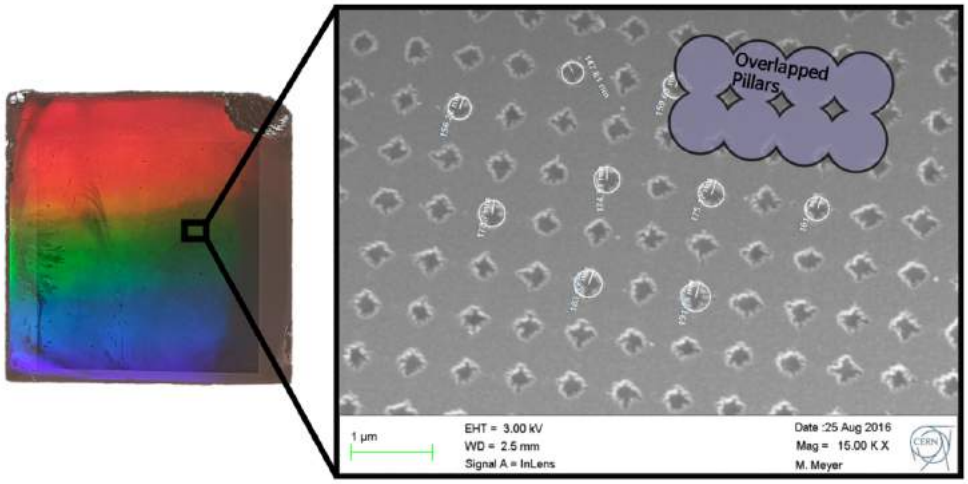

Figure 5.17: Sample Albira 1 patterned with PhC. On the left, a picture of the readout face is shown, damages are observed on the edges. On the right, an SEM picture of the PhC. The diameter was large enough to obtain holes instead of pillars.

5.3.2 Characterization [WP4]

The main goal of work package WP4 was to characterize the properties of the scintillators and to quantify the gain obtained applying PhC to the readout face. To do that, first, an experimental set up had to be developed. The Light yield bench developed is a light-tight box, cooled at 18°C and equipped with the same PMT described in section 2, R10755 with a photo-cathode window of 8.5 cm diameter. For LYSO, this set up has a QE of 24.26% and an accuracy of 2%. The use of plastic masks and holders allows a precise placing of the MAMMI crystals with respect to the PMT, bringing the systematic errors to values negligible with respect to the intrinsic 2% of the PMT. A reference cubic LYSO is used to keep track of the long-term drift of the setup. The digitization is made with a Caen DT5720.
The 12 MAMMI crystals that are needed to complete one ring of the PET scanner were characterized before patterning in the LY bench. All the values presented are the average of 3 independent measurements. The light yield measurements for the 12 crystals gives an average of 3160 ph/MeV with a E_{res} of 22.7%. All the crystals are enclosed in the ±10% for both LY and $Eres$.
Additional tests were performed on ALBIRA a crystal with a shape similar to the MAMMI trapezoid (thickness of 1.2 cm instead of 1.5 cm), in order to tune the patterning parameters. Two samples were tested for the studies on the nano-imprinted TiO_2 pillars production, named Albira 1 (#34LYSO85-4) and Albira 2 (#34LYSO85-3). The damages observed in both the crystals are due to a shipping before the pre-pattern characterization, therefore no bias was introduced between the two comparative LY measurements. As already explained in section 5, the diameter of the pillars is influenced by the reactive ion etching parameters and a fine-tuning of the set up was therefore needed. Figure 5.17 shows the pattern obtained for Albira 1. Being the diameter of pillars bigger than the period, the pillars merged into a single structure, leaving only the holes in between them. The results of the LY measurements are shown in Figure 5.18. A light yield gain is observed but not followed by any E_{res} gain. This is probably due to the strong inhomogeneities observed in the pattern: depending on where the interaction takes place in the crystal, the optical photons reach a region of the readout with different extraction efficiency, therefore broadening the photopeak FWHM.
Figure 5.19 shows the pattern obtained for Albira 2. A light yield gain of 1.34 is observed (Figure 5.20) and the E_{res} is following the opposite trend, with a degrada-

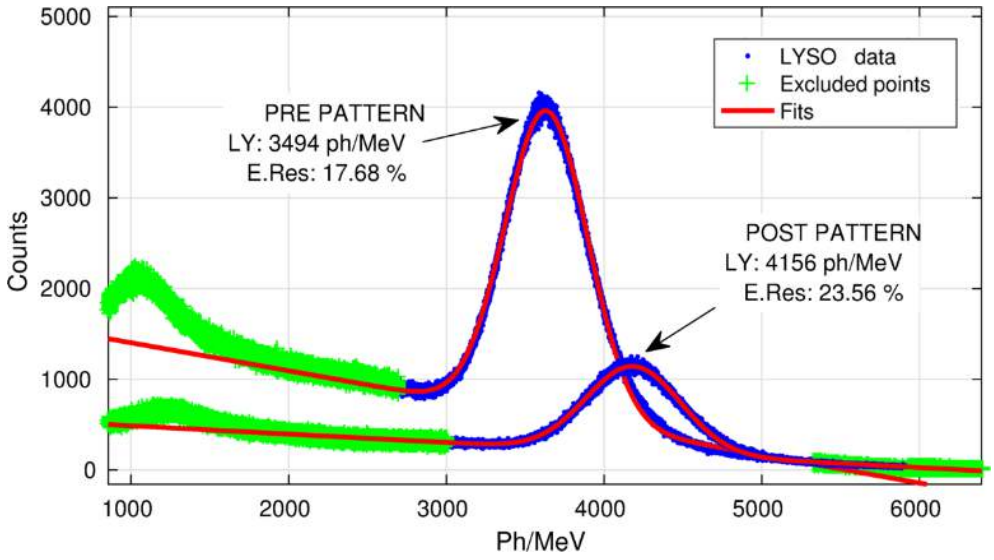

Figure 5.18: LY measurements of the plain surface crystal and patterned one. The LY_{gain} is 1.19 with an E_{res} degraded by 1.33.

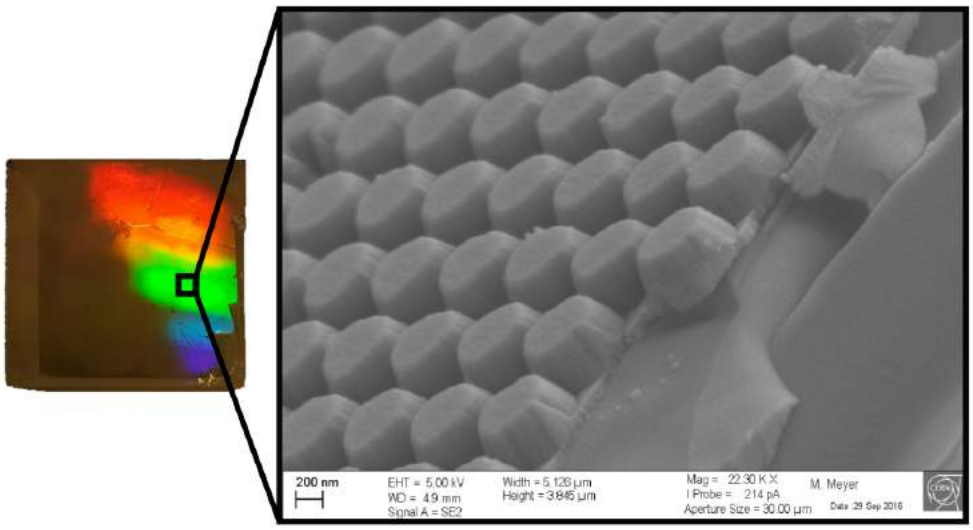

Figure 5.19: Sample Albira 2 patterned with PhC. On the left, a picture of the readout face is shown, damages are observed on the edges. On the right, an SEM picture of the PhC. The pillars diameter is smaller than the period and the geometry is well defined.

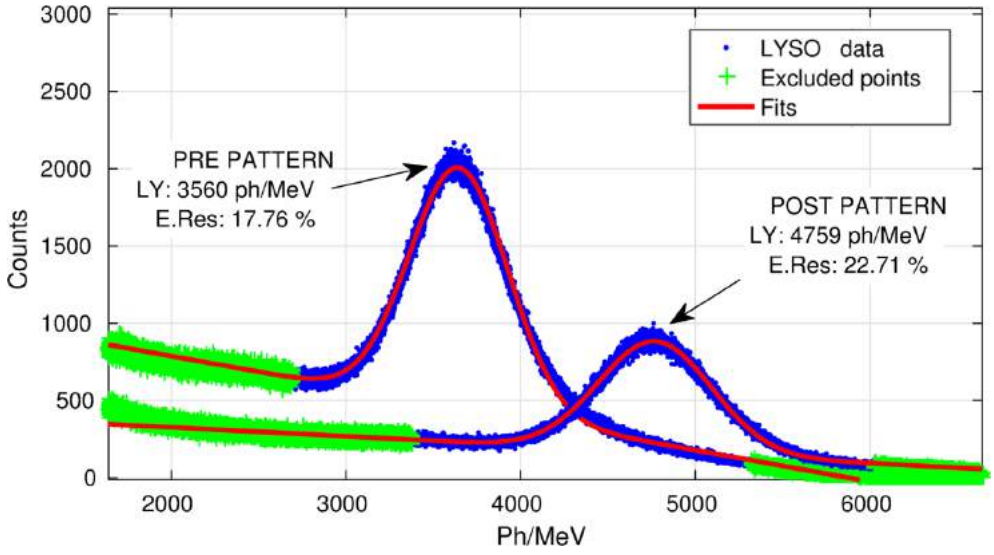

Figure 5.20: LY measurements of the plain surface crystal and patterned one. the LY gain is 1.34, higher compared with the results obtained for Albira 1. The E_{res} is degraded compared with the pre-pattern characterization.

tion of 1.28. The LY gain expected checking in the optimization map (Figure 5.15, left) for the measured diameter (600 nm) is 1.4.

Nano-imprinting PhC production showed good flexibility and feature quality but for covering large readout area, such as the MAMMI $5 \times 5cm^2$, needs further improvement. Non-homogeneities arise probably from RIE plasma, which is not suited for big volume samples. The consequent degradation of E_{res} is much stronger than the benefit coming from LY gain (eq. 1.4).

Test sample measured for the Sol-Gel production method is shown in Figure 5.21. The sample was a MAMMI shaped crystal, not belonging to the 12 MAMMI batch of the scanner ring. The surface was successfully patterned and the PhCs homogeneously distributed. The measured height of the pillars is 600 nm, with a diameter (measured at the base) of 300 nm and hexagonally placed. The TiO_2 cones are not periodically placed on the long-range (Figure 5.22), due to a not perfect self-assembling during the mold production. This will not influence the diffractive effect of the pattern since EM waves do not travel in the layer for more than a few wavelengths. The period measured with the SEM is 900 nm and TiO_2 ellipsometer measurements performed to investigate the quality of the layer showed an RI = 2.2. The simulated LY gain for such a structure is 1.31.

Measurements of the prepattern configuration showed a LY of 2857 ph/MeV with $E_{res} = 29.5\%$, post pattern resulted in 3600 ph/MeV and $E_{res} = 25.6\%$. Therefore, the Sol-Gel sample produced an LY gain of 1.26 ± 0.03, compatible with the simulated performances, and a E_{res} gain of 0.87.

In conclusion, WP4 successfully characterized the scintillation properties for both the pre-pattern and post pattern samples. It identified two potential production technique (routes). A first nano-imprinting route, affected by etching issues, leading to non-reproducible processes and generating strong non-homogeneities across the readout face, therefore degrading the energy resolution. Secondly, Sol-gel technology, limited by production issues. Having high RI cones with a good fill factor (higher diameters cones) is not possible because of the shrinking during annealing, and the diffraction potential of produced sample results small. It is nevertheless a reproducible and homogeneous patterning process.

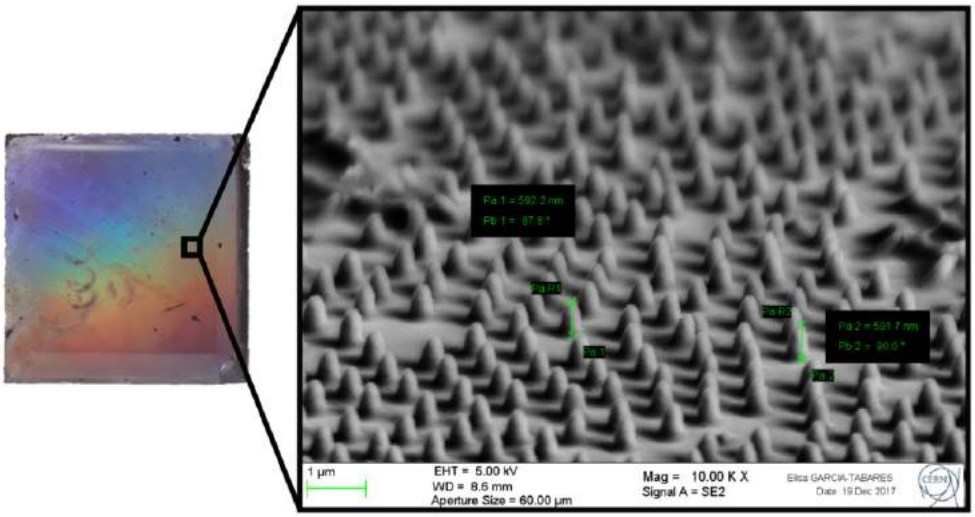

Figure 5.21: MAMMI crystal patterned with TiO_2 PhCs. On the left a picture of the patterned read-out face, on the right, an SEM image of the nano-cones distribute around the surface. The SEM image was recorded at an angle of 80° from the face normal.

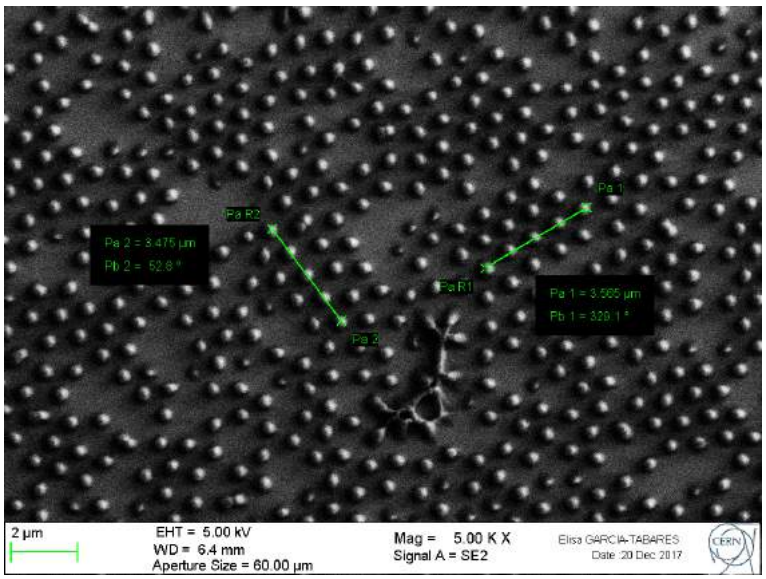

Figure 5.22: SEM image of the PhCs patterned on the readout face of a test MAMMI crystal.

5.3.3 TurboPET outcomes

A first ring patterned with PhCs was produced using the more reliable of the two production processes, the Sol-Gel route. 12 LYSO MAMMI crystals were patterned with an SA mold of $1\mu m$ P and short-range periodicity. The TiO_2 hexagonally placed cones generated an average LY gain of 1.16 (minimum 1.07, maximum 1.24) and a E_{res} gain of 0.8 (minimum 0.86, maximum O.77). The crystals were embedded in the scanner and an SNR gain of 6% was observed. Additional studies are undergoing in order to pattern the second ring with improved PhC pattern.
Taking into account the SNR contrast enhancement of 6% observed with the patterned ring, the feasibility of a clinical test was evaluated. The critical value is the number of patients needed to statistically confirm the difference in the reconstructed image quality. Let's define $Img_{turobPET}$ as the group of lesions scan coming from the patients imaged with the patterned ring and Img_{plain} the same but for the plain ring. If the ratio of within-group variation to between-groups variation is significantly high, then it can be concluded that the group means are significantly different from each other. It is possible to measure this using a test statistic Fisher distributed with $(k-1, N-k)$ degrees of freedom. Defining:

$$\underbrace{\sum_i \sum_j (y_{ij} - \overline{y_{.j}})^2}_{\text{Overall sum of squares = OSS}} = \underbrace{\sum_j n_j (\overline{y_{.j}} - \overline{y_{..}})^2}_{\text{Between groups = BG}} + \underbrace{\sum_i \sum_j (y_{ij} - \overline{y_{.j}})^2}_{\text{Within group = WG}} \tag{5.1}$$

$$F_{stat} = \frac{BG/(k-1)}{WG/(N-k)} \sim F_{k-1,N-k} \ . \tag{5.2}$$

If the p-value for this Fisher statistic is smaller than the significance level, then the test rejects the null hypothesis that all group means are equal and concludes that the mean value of $Img_{turobPET}$ is different from the one of Img_{plain}. Let's define the power of such rejection (Pow_{rej}) as the parameter quantifying the chance that the null hypothesis will be correctly rejected if some alternative hypothesis is really true. Setting the desired power, we can find out the number N of patients needed to reach that power.
For a $Pow_{rej} = 0.8$ and a significance level of 0.05, the number of patients to detect a difference of 6% between the two groups is > 1000. Taking into account that, on average, only 1 over 4 patients will provide lesions measurable by both rings, this would multiply these number by 4. The feasibility of such a clinical test was rejected from WP6, considered the 6-month duration limit of the test.

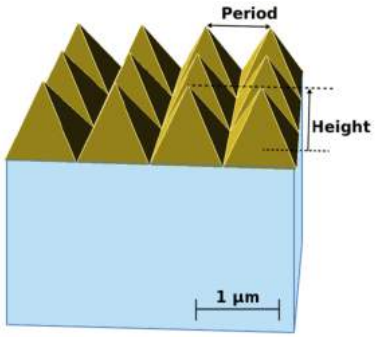

Figure 5.23: Representation of the pyramidal configuration used for the PhC optimization.

5.4 PhC with optical coupling: DNDO project

The most widely used configuration of scintillator detectors makes use of an optical coupling layer between the crystal and the photodetector. This minimizes the losses due to Snell's law reducing the critical angle between the interface, therefore maximizing extraction efficiency. Even with this optimized configuration, the losses are not negligible. This section will present the work done to optimize the extraction efficiency of this optical coupling configuration making use of photonic crystal. A new nanoimprinting production has been used, which make use of lower RI polymers hardened by using UV light exposure.
This work capitalizes on the collaboration with Radiation Monitoring Device Inc. (RMD). It has been funded by the DNDO BAA Contract # HSHQDC-13-C-B0040 and being published in [9].

5.4.1 Simulations

Simulations were performed for a $1cm^3$ LYSO scintillator, optically coupled using a grease of RI = 1.5 and wrapped in Teflon. The crystal was first simulated with Geant4 to obtain the angular distribution of the first incidence photons, which was then used as an input for the photonic crystal optimization in CAMFR, for the reason explained in the previous paragraph. The PhC simulations were run for a pyramidal configuration: conical structures might give a higher potential gain but production constraints make this choice the more feasible. A CAMFR optimization was run over period and height of the pyramids, as illustrated in Figure 5.23. Consecutive pyramids always touch at the base, which means that the base of the pyramids is equal to the period.
The result of this optimization is shown in Figure 5.24. A maximum gain of 1.298 is found for $height = 1\mu m, period = 2.7\mu m$. This simulation assumes a 200nm layer high refractive index material (TiO_2, RI = 2.4) deposited on top of the pattern polymer(RI = 1.825, CP2, see Table 5.2), to increase the diffraction efficiency (4). More details about this thin layer deposition will be discussed in the next sections.

This contour map is the starting point for the imprinting process of several $LYSO$, $GYGAG : Ce$ and SrI_2. Only one molt was produced for the imprinting step, optimized for LYSO, while the results on the other samples were obtained as a tentative trial using a non-optimized mold.

5.4.2 Production

The production process has to fulfill several requirements, such as reproducibility, the capability of patterning big area uniformly, limited budget, properties of the pat-

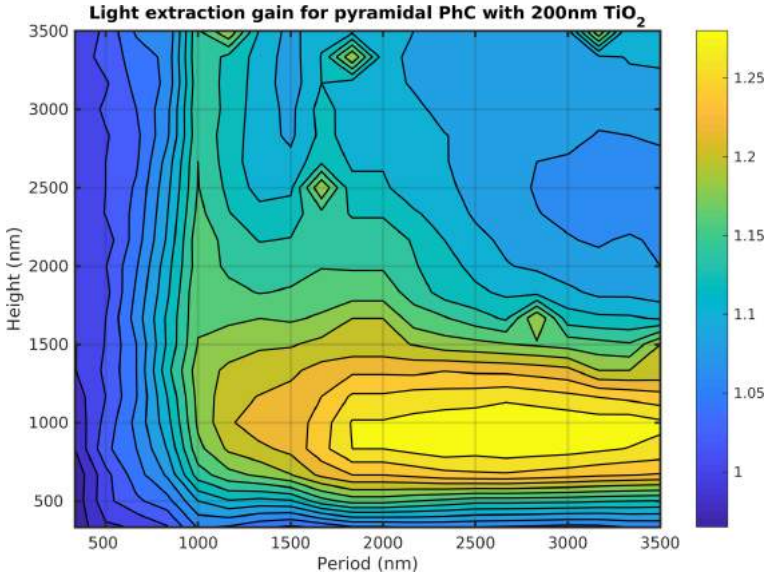

Figure 5.24: Optimization performed with CAMFR for pyramidal PhC. The optimization uses the LY as goodness indicator. The polymer used for this imprint has an RI = 1.82 at 400 nm. The maximum gain observed is 1.298. The gain reported here is related only to the photons touching the readout face for the first time (4), which are the most relevant when dealing with the time resolution of the detector (this is done to reduce the computational load). The PhC here presented is furthermore covered with 200 nm of high refractive index material (TiO_2), to increase the diffraction efficiency.

tern (feature precision $\pm 10nm$, transparency, temperature resistant, scratch resistant, high refractive index) and available facilities. Nano-imprinting is a well-suited technique for many of the aspects listed. This process uses stamp or mold or master in order to physically deform a polymer. Specifically, the technique selected use an additional step during the deformation phase to harden the polymer using UV light or high temperatures, before to release the stamp: this step is called UV/thermal curing. It requires the stamp to be transparent in the case of UV light, which is beneficial for reproducibility and costs. The silicon template mold, created using laser interference lithography, will be used to create replicas made of quartz, which is transparent in the UV region of the spectrum. The patterning of the PhC slabs will only happen through the replicas, leaving the more expansive template intact. A schematic representation of the PhC patterning process is shown in Figure 5.25. The template silicon stamp of $10mm \times 10mm, 15mm \times 15mm, and 25mm \times 25mm$ was produced in collaboration with the Lawrence Berkeley National Laboratory,

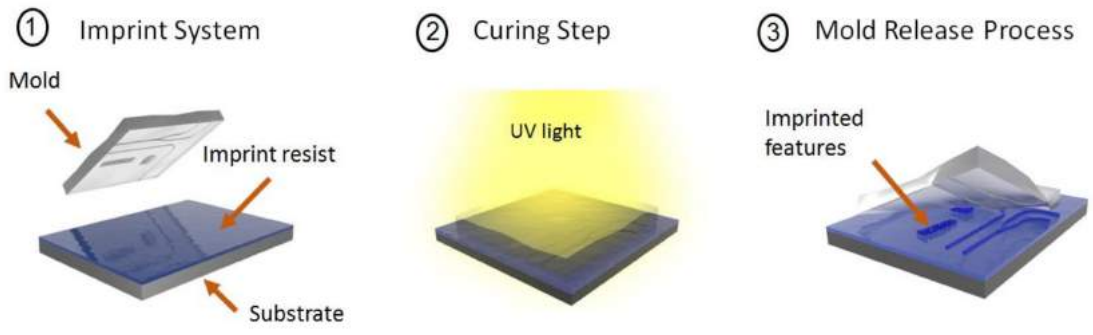

Figure 5.25: Schematic of the nanoimprinting process used for fabricating the PhCs.

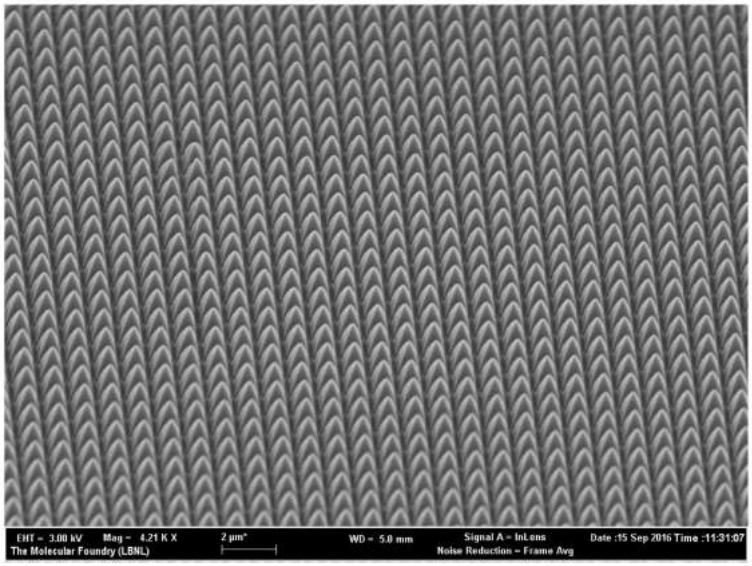

Figure 5.26: Scanning electron microscope (SEM) image of the silicon template used for nanoimprinting in the high index of refraction polymers.

using a laser interference lithography and fabricated using standard semiconductor processing techniques. The templates features are shown in Figures 5.26, 5.27. Even if the parameters of the pattern does not match the structures suggested by simulations, these templates were selected for imprinting tests thanks to its feature quality. Nano-imprinting UV/thermal curing production technique needed the development of optically transparent, high refractive index polymers in which the nanostructures can be imprinted. Thanks to the collaboration of aBeam Technologies we created custom high RI polymers which are optically transparent in the crystals emission spectra, and either UV-curable or thermally-curable.
The polymer developed during this project are schematically represented in Table 5.2.

Table 5.2: Custom developed high RI polymer specifications:

Polymer	Refractive index	Curing method
CP2	1.825	UV
CP4	1.785	UV
CP5	1.875	Thermal
CP5a	1.930	Thermal

Table 5.3: Parameters of the various imprinted samples:

Sample	Refractive index	Peak emission (nm)	Sample size
$LYSO:Ce$	1.82	420	$1cm^3$
$GYGAG:Ce$	1.785	540	$1cm$ diam., $0.5cm$ thick
$SrI_2:Eu$	1.82	435	$1cm^3$
Fused silica	1.466	Not applicable	$3cm$ diam., $0.2cm$ thick

The wavelength dependency of CP2, CP4, and CP5 RIs is shown in Figure 5.28, on the right, together with the measured transmission, on the left.

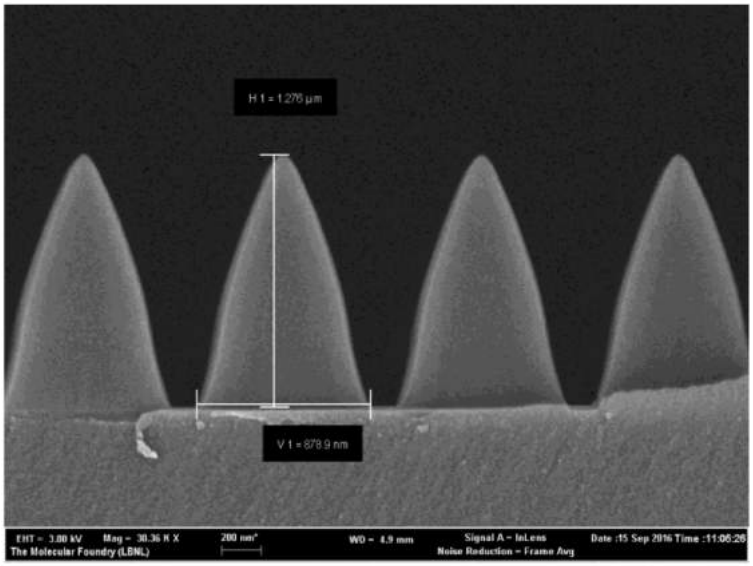

Figure 5.27: SEM image of the feature imprinted in the silicon template used as stamp for the PhCs fabrication. The nano-pyramids have a base diameter of 880 nm, and a height of 1275 nm, as indicated by the horizontal and vertical scale bars, respectively.

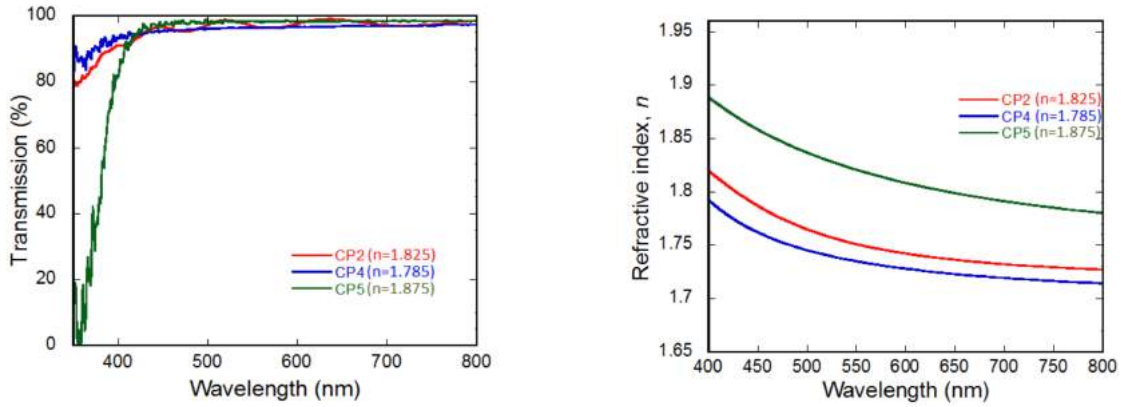

Figure 5.28: Refractive index profiles of CP2, CP4, and CP5 polymers measured with an ellipsometer (right) and transmission measurements (left), measured using a Cary 5000 UV-Vis-NIR spectrophotometer.

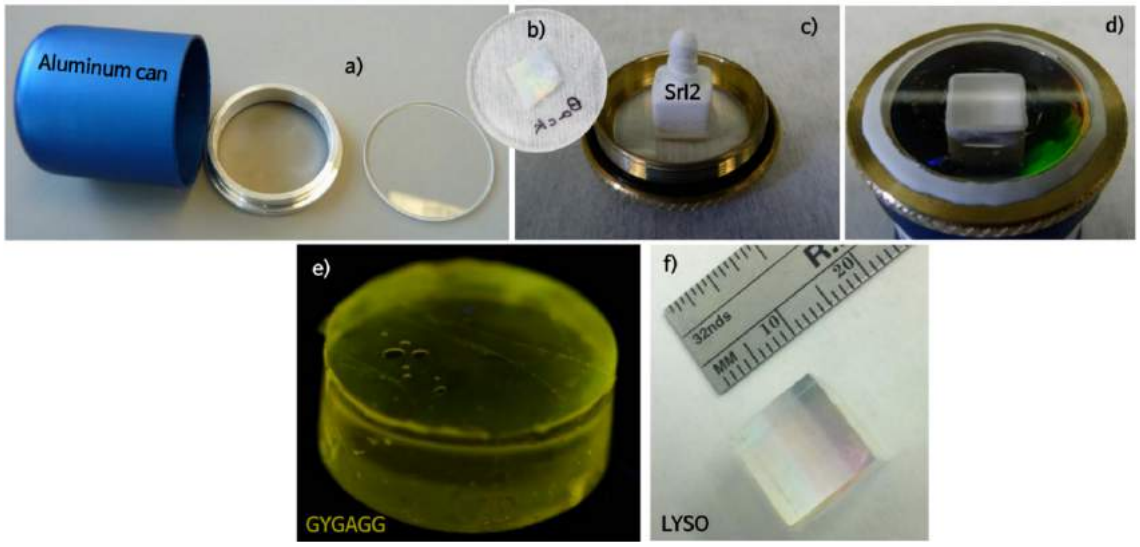

Figure 5.29: Sample imprinted with the pyramidal PhCs. The top images shows the process for encapsulating the SrI_2 with nan-imprinted window can. a) Aluminum can with non imprinted window and b) window after imprinting. c) SrI_2 glued on the imprinted part of the window and d) the crystal safely enclosed in the can. e) and f) shows imprinted $GYGAGG$ and $LYSO$ crystals respectively.

5.4.3 Imprinted samples

The specifications of the various imprinted samples, including the scintillators and the fused silica window used in the experiments, are listed in Table 5.3. The nano-imprinting was carried out directly on cylindrical $GYGAG : Ce$ ceramic, cubic $LYSO : Ce$ scintillators, and on the 30 mm diameter exit window of the package used for the extremely hygroscopic $SrI_2 : Eu$ cylindrical scintillator.
Photographs of these nano-imprinted samples are shown in Figure 5.29. It should be pointed out that it was not possible to obtain any SEM to verify the imprinted PhC structures because of the following two reasons. (1) To obtain SEM images, a thin conducting layer of gold needs to be deposited on the imprinted polymer, otherwise, because of the non-conducting nature of the imprinted polymer layer, there is an electrostatic charge build-up, making it difficult to obtain SEM images. However, depositing the gold layer on the PhC would alter the properties of the PhC structures. This rules out depositing gold before testing the imprinted nano-structures. (2) During testing of the scintillator with the imprinted nano-structure, optical coupling fluid IML 150 is used between the nanostructure and the PMT window. Gold cannot be deposited on the imprinted structure after doing light extraction measurements because of the presence of the IML 150. Therefore, identical size samples were first used to optimize the imprinting parameters, and then those parameters were used for imprinting on the actual samples.

Once the pattern is imprinted on the sample, 200 nm of TiO_2 (or an equivalent high RI material transparent in the LYSO emission region) should be deposited on top of the pyramids, in order to fully exploit the diffraction efficiency. This was never successfully completed due to incompatibility between the standard TiO_2 deposition processes and the polymer used for the PhCs. Several technological steps were considered and tested. Atomic Layer Deposition (ALD) is a slow, highly conformal technique, which could produce a high-quality layer with a precision down

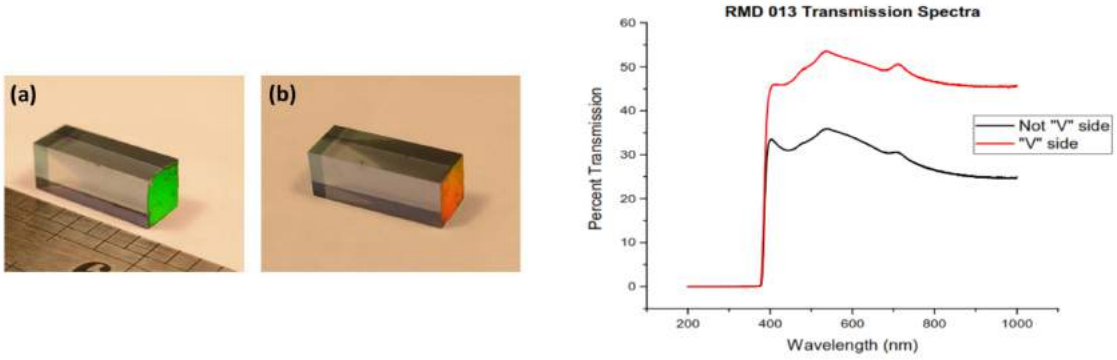

Figure 5.30: ALD representation.

to $\sim$ 1 nm level. For TiO_2 production, temperatures up to 600°C are used, whereas a polymer like CP2 cannot stand temperatures above 200°C: it will burn and loose the imprinted shape. Figure 5.30, on the left, shows the result of 50 nm deposition on an LYSO imprinted sample. The process temperature was lowered below the melting point of the polymer. The dark 'V' area on the non-readout faces is the absorption of the visible light from the layer: lower temperature creates a lack of oxygen in the TiO_2 lattice. A transmission measurement was performed on the darker area and compared with the clearer region, reported in the right part of Figure 5.30. To avoid this, a deep analysis is needed to find new ALD parameters, which is now undergoing, in parallel with the investigation of other materials (CeO2, HfO2).
Another solution could be offered by means of sputtering deposition, not conformal but which offered the possibility to deposit $Ti0_2$ at a lower temperature. This option is also currently investigation. A preliminary analysis suggests that the non-conformality could be too strong, leading to smoothed and unpredictable coverage of the pyramids, with compromised diffracting properties.

5.4.4 Results

The LY measurements were performed using a Hamamatsu R6233-100 PMT at RMD. For each of the sample, 6 layers of $\sim 75\mu m$ Teflon tape were used as a Lambertian reflector for the non-readout faces. For the LYSO and GYGAG crystals, the readout face was optically coupled to the PMT borosilicate window using an Index Matching Liquid 150 (IML 150) from Norland Products, Inc., (Cranbury, NJ), with RI = 1.52. For the SrI_2, due to its hygroscopicity, it was not possible to imprint directly the scintillator surface. We, therefore, imprinted the glass cover of the aluminum can made of fused silica and with an RI = 1.466, and used the IML 150 to couple the window to the crystal. The same was done for the closed can and the PMT window. The measurements were performed using either a ^{137}Cs and ^{57}Co radioactive sources.
The result of the measurements for all the samples are shown in table 3. The values are shown in ADC channels: since the relevant data is the gain between untreated configuration and patterned one, no calibration was needed. A reference crystal was used to keep track of the long-term bench fluctuations: $gain = ADC_{post}/ADC_{pre} * ref_{pre}/ref_{post}$. In our case, the post pattern values are already compensated for the reference fluctuation.
The LYSO sample was imprinted with CP2. The LY measurements exciting with 57 Co shows a gain in the photopeak position of 1.2 and an energy resolution of 0.85 (the gain convention is described in the methods chapter). The GYGAG sample was imprinted using two different polymers, CP2 and CP5, and excited using a cs137 source. Both the imprinted polymers shows enhancements in the

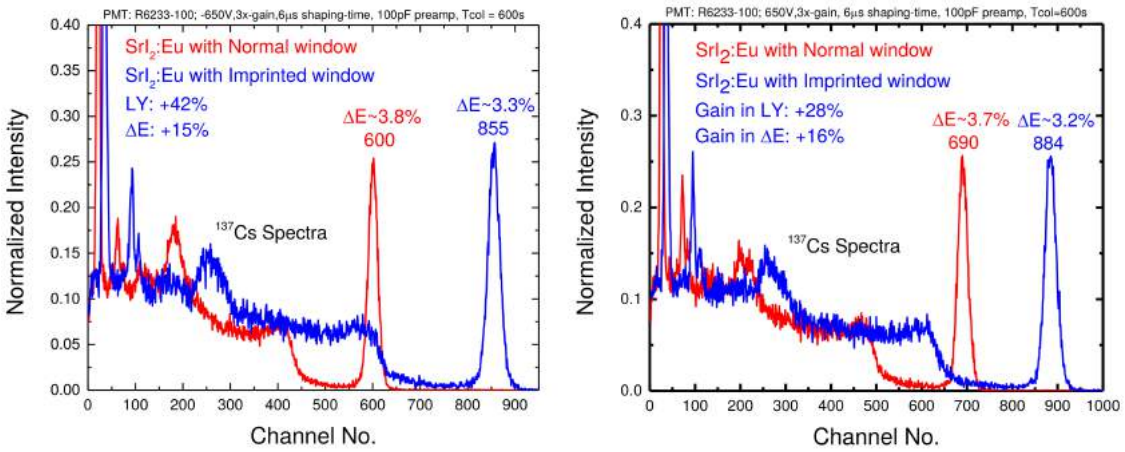

Figure 5.31: SrI 2 :Eu light output and energy resolution measured through a regular window (shown in red) and a window with PhC imprinted in CP2 (left) and CP5 (right) polymers (RI=1.875) (shown in blue)

light yield and the energy resolution. The polymer with higher RI exhibits greater increases in the light yield and energy resolution. This can be easily explained by the higher the RI: it means a higher number of electrons that interact with the incoming electromagnetic wave, therefore higher the potential effect that is achievable with a PhC. Nanoimprinting in CP2 resulted in a 1.41 enhancement in the light yield and a 0.96 improvement in the energy resolution in the GYGAG sample. When the same GYGAG sample was reused with imprinting done in CP5, the corresponding gains in the light yield and energy resolution were 1.51 and 0.92, respectively.
The energy resolution of 8% at 662 keV obtained for the non-imprinted GYGAG:Ce sample used in these experiments is worse than the energy resolution of 5% at662 keV reported in the literature [10][11]. This could be due to non-perfect surface state condition (rough polishing, edges defects), which is known to be a source of degraded the energy resolution.
Last, $SrI_2 : Eu$ was tested. The ^{137}Cs spectrum was first acquired using the non-imprinted quartz window, which was coupled to the PMT using the same IML 150 coupling fluid used on the inner surface between the window and the scintillator. Then the non-imprinted quartz window was replaced by a quartz window on which the PhCs were nanoimprinted on the inner surface. The SrI_2 sample was again grease-coupled to the nanoimprinted window in the package, and the ^{137}Cs spectrum was again acquired after grease-coupling the outer non-imprinted surface of the quartz window to the PMT. The ^{137}Cs spectrum of the SrI_2 sample with the non-imprinted and the imprinted windows are shown in Figure 5.31. For one of the SrI_2 samples, where the PhCs were imprinted in the CP5 polymer with n = 1.875, the PhCs enhanced the light yield by 1.43 and the energy resolution by 0.87. In another sample, where the PhCs were also imprinted in CP5 polymer, the light yield enhanced by 1.28, whereas the energy resolution improved by 0.86. One reason for a lower efficiency of CP5, in this case, could be the absorption in the crystal emission region, which has a peak at 435 nm, close to the cut-off of the polymer (420 nm).
These samples need to be further treated with a thin layer of TiO_2 to fully exploit the diffraction efficiency of the pattern.

5.4.5 Perspective

The idea of introducing photonic crystals to increase the performance of scintillating crystals used in ionizing radiation detection had been first introduced in 2008 [15]. The first goal was to overcome the problem of light extraction and light coupling

inefficiencies from the crystal to the photodetector because of the high refractive index mismatch between the crystal (generally high) and the out-coupling medium (generally low). The technology to produce these photonic crystals has been so far mostly inspired by well-known lithography techniques.
Until now, the main emphasis has been on improving the timing performance of time-of-flight (TOF) PET scanners by increasing the light extraction efficiency and reducing the time jitter induced by photon bouncing in L(Y)SO crystals. However, other scintillation mechanisms are of high interest for fast timing, such as cross-luminescence in crystals like BaF_2. The fact that cross-luminescence takes place in the UV part of the spectrum (170 nm and 220 nm for BaF_2) introduces specific constraints on the photodetector and the coupling medium between the crystal and the photodetector. A new generation of UV-sensitive silicon photo-multipliers (SiPM) is being developed by several manufacturers, which reactivates the need for an efficient optical coupling with the crystal in the UV range. Specially-designed PhCs could optimize the transfer efficiency from the scintillator to the SiPM through the air (certainly more transparent than any optical grease in this wavelength range) and open the way to efficient and compact single UV photon counting devices.
The design of the PhCs has been based so far on relatively simple geometries, such as a regular distribution of pillars or holes in a high refractive index substrate. The study of more complex structures has been so far only superficially explored. It concerns, in particular, the combination of wavelength and sub-wavelength structures to provide an adiabatic impedance matching between the crystal and the out-coupling medium through a gradient index medium (GRIN). Several possibilities have been mentioned and need a thorough investigation, such as multiple layers with different levels of structuration, conical structures or a combination of both [24].
Although not exploited so far, the PhCs, if properly designed, can shape the light distribution in addition to the improvement in light extraction efficiency. This effect can be useful if one wants to collimate the light from a scintillator onto a photodetector. Such a collimation could help with optimizing the detection efficiency by avoiding grazing angles on the photodetector. One can also consider multifunctional metamaterials, emitting at different wavelengths for different types of particles converting in the detector. As the collimation effect is wavelength dependent, one could design PhCs to redirect the different components to a set of dedicated photodetectors. This approach has been proposed to unfold the hadronic, electromagnetic and neutron components in a hadronic shower and to improve the energy resolution of hadron calorimeters in particle physics experiments [19].
As not only the coupling face of the scintillator to the photodetector but also the lateral faces play an important role in the light transport from the ionizing radiation interaction point to the photodetector, some photonic approaches can be applied to the lateral faces, as well, to optimize the light distribution of the photons impinging on the PhC on the output face of the crystal and to further enhance the light extraction efficiency. As an example, the diffusive wrapping, traditionally used in scintillator crystals, could be replaced with photonic nano-antennas (PNAs, [8]) operating under the principle of localized surface plasmon resonances excited on the surface of thin metallic films. Such plasmonic nano-antennas could be designed to deflect the isotropically-emitted scintillation photons into a narrow beam being directed towards the photosensor area with minimum dispersion. Alternatively, we can think of the metallic elements in the array as polarizable radiating dipoles. The field emitted by each element polarizes the rest of the elements in the array, generating a collective resonant field radiated by the entire structure.
Another interesting possibility is to design ionization radiation detectors based on heterostructures, where the light production and the light transport would be decoupled. This approach could present a serious advantage when working in a high radiation environment, such as at high luminosity collider particle physics experiments or nuclear plants. The light transport is severely compromised in these cases by the radiation damage of the scintillator, through the production of color centers

and related absorption bands. A detector design, allowing hollow core photonic fibers able to collect the light as close as possible to the ionizing radiation conversion points in the scintillator, would alleviate this problem, as the energy of the electromagnetic wave would propagate in the hollow core of the photonic fiber, i.e., air, which is ultimately radiation hard. For such detector designs, photonic crystals deposited at the surface of the photonic fibers would enhance the light coupling with the scintillator and the overall performance of the detector.
As mentioned previously, the application of photonic crystal technology to scintillator-based radiation detectors is still in its infancy, and only rather standard nanolithography or direct embossing approaches have been considered so far. Scaling-up inexpensive production methods is a major concern for the deployment of this promising technology. The impressive development of nanotechnologies offers a vibrant ecosystem and fascinating perspectives for scalable and inexpensive production methods. Of particular interest are the direct embossing of high refractive index polymers, colloidal approaches, and bottom-up self-assembly techniques.

5.5 Conclusions

The push for better performing scintillator-based ionizing radiation detectors, particularly in terms of energy and time resolution, has shed light on the potential of photonic crystals to overcome the severe limitation of light extraction efficiency because of the refractive index mismatch between the scintillation crystal and the surrounding medium. After discussing how the performances of the best existing scintillators need to be further enhanced to answer the requirements of a new generation of ionizing radiation detectors, this work detailed the theoretical background supporting the role of photonic crystal slabs in breaking the Snell's law barrier and enhancing the light extraction efficiency from a high index crystal. The complex simulation toolkit developed for this purpose was described and explains how light ray tracing software needs to be combined with a number of specific coupled wave analysis modules working at the wavelength and sub-wavelength scale to provide a full description of the fate of an optical photon, once generated by the scintillation process.
An important part of this thesis was devoted to a description of photonic crystal production methods. A large effort is being made by several groups to explore different methods for a reliable, scalable and cost-effective production of photonic crystal slabs. Several examples are then given of the sample produced using different production methods, but all showing promising results. The photonic crystal research area is a vibrant and exciting domain, offering a huge potential, as only a small part of it has been explored so far.

Bibliography

[1] Turtos M. R.; Gundacker S.; Pizzichemi M.; Ghezzi A.; Pauwels K.; Auffray E.; Lecoq P.; Paganoni M.; Measurement of LYSO Intrinsic Light Yield Using Electron Excitation. *IEEE Trans. Nucl. Sci.* **2016**, 475-479.

[2] Gundacker, S.; Auffray, E.; Frisch, B.; Jarron, P.; Knapitsch, A.; Meyer, T.; Pizzichemi, M.; Lecoq, P.; Time of flight positron emission tomography towards 100ps resolution with L(Y)SO: An experimental and theoretical analysis. *J. Instrum.* **2013**, *8*, doi:10.1088/1748-0221/8/07/P07014.

[3] Anghinolfi, F.; Jarron, P.; Krummenacher, F.; Usenko, E.; Williams, M.C.S. NINO: An Ultrafast Low-Power Front-End Amplifier Discriminator for the Time-of-Flight Detector in the ALICE Experiment. *IEEE Trans. Nucl. Sci.* **2004**, *51*, 1974–1978.

[4] Improving the light yield and timing resolution of scintillator-based detectors for positron emission tomography. Available online: `https://edoc.hu-berlin.de/handle/18452/17900`; (accessed on 29 December 2017) .

[5] Zhu, Z.; Wu, S.; Xue, C.; Zhao, J.; Wang, L. ; Wu, Y.; Liu, B.; Cheng, C.; Gu, M.; Chen, H.; et al. Enhanced light extraction of scintillator using large-area photonic crystal structures fabricated by soft-X-ray interference lithography. *Appl. Phys. Lett.* **2015**, *106*, doi:10.1063/1.4922699.

[6] Siefke, T.; Kroker, S.; Pfeiffer, K.; Puffky, O.; Dietrich, K.; Franta, D.; Ohlídal, I.; Szeghalmi, A.; Kley, E.B.; Tünnermann, A. Materials pushing the application limits of wire grid polarizers further into the deep ultraviolet spectral range. *Adv. Opt. Mater.* **2016**, *4*, 1780–1786.

[7] Chang, C.; Dominguez-Caballero, J.A.; Choi, H.J.; Barbastathis, G. Nanostructured gradient-index antireflection diffractive optics. *Opt. Lett.* **2011**, *36*, 2354–2356.

[8] Giannini, V.; Fernández-Domínguez, A; Heck, S.; Maier, S. Plasmonic nanoantennas: Fundamentals and their use in controlling the radiative properties of nanoemitters. *Chem. Rev.* **2011**,

[9] B. Singh et al., "Enhanced Scintillation Light Extraction Using Nanoimprinted Photonic Crystals," in IEEE Transactions on Nuclear Science, vol. 65, no. 4, pp. 1059-1065, April 2018. doi: 10.1109/TNS.2018.2811646.

[10] N. J. Cherepy et al., "Development of Transparent Ceramic Ce-Doped Gadolinium Garnet Gamma Spectrometers," in IEEE Transactions on Nuclear Science, vol. 60, no. 3, pp. 2330-2335, June 2013. doi: 10.1109/TNS.2013.2261826

[11] N.J. Cherepy, Z.M. Seeley, S.A. Payne, E.L. Swanberg, P.R. Beck, D.J. Schneberk, G. Stone, R. Perry, B. Wihl, S.E. Fisher, S.L. Hunter, P.A. Thelin, R.R. Thompson, N.M. Harvey, T. Stefanik, J. Kindem, “Transparent Ceramic Scintillators for Gamma Spectroscopy and MeV Imaging,” SPIE Optical Engineering+ Applications, 95930P-95930P-7 (2015).

6

Fast scintillation materials

6.1 Introduction

This chapter will focus on reducing coincidence time resolution (CTR) by using scintillators with fast rise and decay time. Generating such a prompt response could provide radiation detectors with the boosted properties required by future applications in ToF-PET and HEP. CTR values of 117 ± 3 ps [1] have been achieved for 20 mm long LSO:Ce Ca co-doped crystals under 511 keV γ-rays excitation, which in ToF-PET translates into a background rejection area down to the centimeters scale. The breakthrough will follow CTR values of 10 ps instead, leading to an annihilation point reconstruction close to the intrinsic limit of the decay production, determined by the positron range.
Two aspects have to be accounted for while seeking for fast timing in scintillator detectors. The first is the number of scintillation photons emitted that actually contribute to the time tag of the event, the "prompt signal" collected at the photo-detector in the first few hundreds of ps. The second is the single photon time resolution (SPTR) of the photo-detector, which is the lower bound for how precisely fast scintillation photons can be recorded. Figure 6.1 shows Cràmer-Rao CTR lower bound calculations as a function of SPTR and number of prompt photons recorded by the photo-detector. The time profile of LSO:Ce scintillation was used to account for rise time ($\tau_r = 70ps$) and decay time ($\tau_d = 40ns$) of the crystal. Two geometries were investigated, with different light transfer efficiencies (LTEs): (a) 3 mm and (b) 20 mm lengths. As a practical example, to achieve a CTR value of 10 ps FWHM a prompt signal of the order of 100 photons has to be efficiently recorded by a SiPM with an SPTR of $\sigma = 10$ ps for a 3mm long LSO:Ce. This chapter will discuss how light production mechanisms can be improved in order to reach such prompt photons level. While SPTR of 10 ps is already available for stand-alone single-photon avalanche diode (SPAD), a fast response generating the few hundreds of prompt

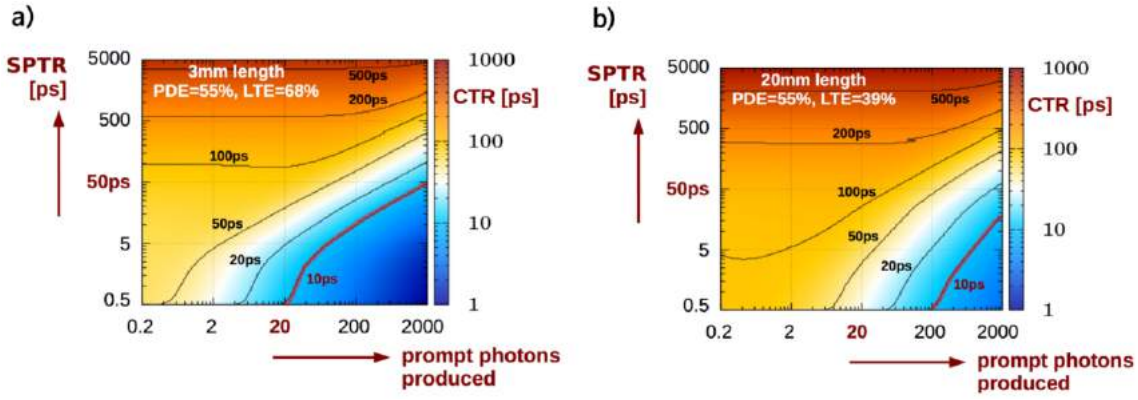

Figure 6.1: Cramèr-Rao lower bound calculations for CTR using an LSO:Ce scintillator of (a) 3 mm and (b) 20 mm length as a function of SPTR and number of prompt photons.

photon needed is not yet found in the scientific community.
What will be presented here is a new approach to produce ultrafast emission dynamics making use of colloidal semiconductor nanocrystals (NCs). Several groups worked intensively during the last decade to overcome problems such as strong carrier confinement, high surface to volume ratio (fragile structures) and small Stokes shifts, which used to degrade the performance of scintillators. Auger recombination, generated by carrier confinement, has been mitigated with 2D nanoplatelets (NPLs) [2],[3], and heterostructured core/shell NCs [4]. CdSe/CdS core/shell and particularly core/giant shell QDs (GS QDs) have improved photostability due to reduced charge transfer surface traps. Large Stokes shifts in GS QDs can reduce reabsorption by separating emission from CdSe QD core to absorption from CdS shell [4] [5].

6.2 NCs theory

Semiconductor nanocrystals (NCs) are crystalline nano-particles which maintain the crystalline structure of the bulk material. Due to the small size of these quantum dots, their physical properties change significantly compared to a macroscopic bulk crystal. Bulk semiconductors are characterized by a composition-dependent band gap energy, while quantum confinement effect generates size-dependent optical and electronic properties in NCs. This effect is stronger for particle size smaller than the Bohr exciton diameter (aB), which can vary from 1 nm to more than 100 nm depending on the material. Semiconductor NCs with dimensions smaller than (aB) demonstrate tunable absorption and fluorescence spectra with discrete electronic transitions. This can have strong effects on carrier dynamical behaviors [6], [7], [8] [9], as well as resulting in spectral shifts of multiexciton emission bands[13]. High Efficient photogeneration of multiexcitons by single photons excitation (carrier multiplication or CM) was also observed, due to enhanced carrier-carrier interactions. This section will give an overview of the theory supporting such NCs properties.

6.2.1 Nanoscale confinement

The starting point for giving a theoretical base to nanoscale confinement effects is to consider an atomic particle with mass m and mechanical energy E in an environment characterized by a potential energy function $U(x)$ such as the one defined below:

$$U(x) = \begin{cases} 0 & for \quad 0 < x < a \\ \infty & \text{everywhere else.} \end{cases} \tag{6.1}$$

The Schrödinger equation for the particle wave function is:

$$\frac{-\hbar^2}{2m}\frac{d^2\psi}{dx^2} + U(x)\psi = E\psi \tag{6.2}$$

and introducing the infinite potential well, the wave equation reduces to:

$$\psi(x) = 0 \quad for \quad U(x) = \infty \qquad (a) \tag{6.3}$$

$$\frac{-\hbar^2}{2m}\frac{d^2\psi}{dx^2} = E\psi \quad for \quad U(x) = 0. \qquad (b) \tag{6.4}$$

The wave function is non zero only inside the well: defining $k = \sqrt{\frac{2mE}{\hbar^2}} > 0$, equation 6.3 becomes:

$$\frac{d^2\psi}{dx^2} = -k^2\psi \tag{6.5}$$

so that the general solution can be expressed as oscillatory functions:

$$\psi(x) = Asin(kx) + Bcos(kx). \tag{6.6}$$

The continuity condition at the boundaries x = a and x= 0 will lead to the set of solutions expressed below:

$$\begin{aligned} & \psi(a) = \psi(0) = 0 \\ \text{which leads to :} \quad & \psi(0) = 0 \rightarrow B = 0 \\ \text{and} \quad & \psi(a) = 0 \rightarrow Asin(ka) = 0 \rightarrow k = n\pi/a \ ; \end{aligned}$$

The solution:

$$\psi_n(x) = \begin{cases} A_n sin(\frac{n\pi x}{a}) & for \quad 0 < x < a \\ 0 \quad \text{everywhere else.} \end{cases}$$

Normalizing the eigenfunctions according to the values of A_n of equation 6.7:

$$\int_{-\infty}^{\infty} |\psi_n|^2 \, dx = |A_n|^2 \int_0^a sin^2(\frac{n\pi x}{a}) dx = \frac{|A_n|^2 \, a}{2} = 1 \tag{6.7}$$

$$|A_n| = \frac{2}{a}, \quad \forall \ n \ . \tag{6.8}$$

The energy eigenfunctions of the infinite square well are a discrete series of sine functions labeled by n. Therefore, a quantum particle inside an infinite square well can only take quantized (discrete) values of E:

$$using \quad k_n = n\pi/a \quad in \quad k = \sqrt{\frac{2mE}{\hbar^2}} \rightarrow E_n = \frac{n^2\pi^2\hbar^2}{2ma^2} \tag{6.9}$$

$$for \quad n = 1, 2, 3, .. \tag{6.10}$$

The separation between the discretized energetic levels follows a $1/a^2$ relation. Smaller the nano-particle, higher the forbidden energies between bands and higher the band gap between conduction and valence band. This will result in a scintillation light shifted towards the blue (higher energies), as shown in Figure 6.2.
One of the main implications of discretization of electronic bands is the suppression of the phonon-assisted relaxation of electrons during the thermalization process: the difference between energy levels is usually larger than the thermal energy of the crystal (mean energy $\sim 25meV$). This favors two other processes which are normally negligible in normal bulk semiconductors: carrier multiplication (CM) and Auger recombination (AR). These processes are responsible for most of the non-radiative transitions within nanocrystals under high energy excitation.

AR usually plays a major role in the NCs carrier dynamics: the constraints imposed upon AR by momentum conservation in the bulk are expected to be relaxed in nanocrystals [16]. Carriers contained within NCs discretized energy levels (see Figure 6.3) are expected to conserve total carrier energy and angular momentum but not translational momentum [17]. AR should occur without an energetic barrier and the re-excited carrier can easily access an energy-conserving state with an appropriate momentum value [18]. This difference from bulk semiconductors has several implications. The lack of a barrier to AR in NCs means that (i) low-energy e-h pairs are available for Auger recombination whereas in the bulk they are not due to missing momentum (compare Figure 6.3(a) and (c)), (ii) temperature does not influence the Auger recombination rates, (iii) the nanocrystal's size (which defines

Figure 6.2: Picture of four different QDs solutions with different emission wavelengths. The QDs dimension is increasing from left to right. On the left side, a representation of the dimension trend and on the right the bang gap dependency on the dimension is depicted. Smaller the NP diameter, higher the band gap and smaller will be the emitted wavelength.

Coulomb coupling) and wave function overlap determine AR rates rather than the energy gap, and (iv) the inverse-AR process of impact ionization may also be barrierless.
The channels available for Auger recombination in semiconductors are shown in Figure 6.4. 1) shows an electron recombining with a hole with energy level difference absorbed by another electron. 2) involves a phonon whose phase-space helps to relax conditions in the energy and momentum of the recombining particles. 3) shows a localized state involved in the process and 4) describes an internal transition in a donor-acceptor pair. The rate for the direct Auger effect is closely related to the electron-electron scattering rate with the only difference that one of the electrons have its final state in another band. The recombination rate will be given by the familiar equation of first-order perturbation theory:

$$W = \int_f \frac{2\pi}{\hbar} |M|^2 \, \delta(E_f - E_i) dS_f \tag{6.11}$$

with f and i final and initial states respectively, the integral is over all final states S_f. M is the matrix element of the transition. Calculating M, the recombination rate will be proportional to the density of electron-hole pairs created in the material: higher the density of states, faster the Auger recombination will be. Due to the high carrier density exhibited in nanocrystals $\sim 10^{19} e - h \ cm^3$, with an average of 1 e-h pair per crystallite, Auger recombination is one of the main non-radiative processes. This has been experimentally proven by [19] where CdSe quantum dots of different sizes were used to study confinement-induced modifications in Auger-type interactions during the transformation from bulk crystalline to atomic regimes.
AR is detrimental for scintillation because is a non-radiative process. Other processes compete with AR, such as Carrier Multiplication (CM) takes place. Strong carrier-carrier interactions open new relaxation channels for excess energy not dissipated via electron-phonon scattering, transferring it to another valence band electron during a collision-like event. If the initial energy is enough, a gamma absorption

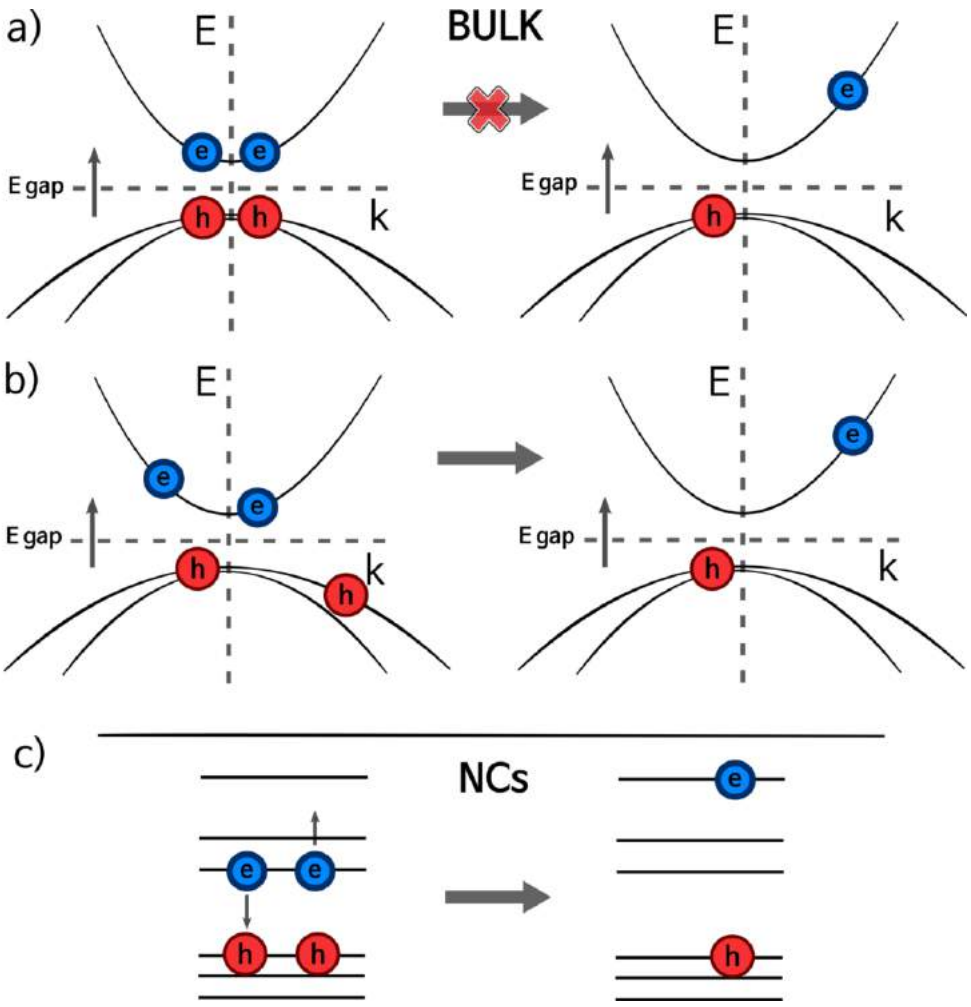

Figure 6.3: Main differences between Auger recombination processes in bulk and nano-semiconductors. (a) Low energy carriers in a bulk semiconductor with energy gap E_g can not undergo Auger recombination (AR) due to requirements that energy (E) and momentum (p) are conserved simultaneously. (b) Higher energy carriers can undergo AR in a bulk semiconductor. (c) Low-energy carriers in a semiconductor NC can undergo AR due to the discrete character of the energy levels, which results in relaxation of translational momentum conservation.

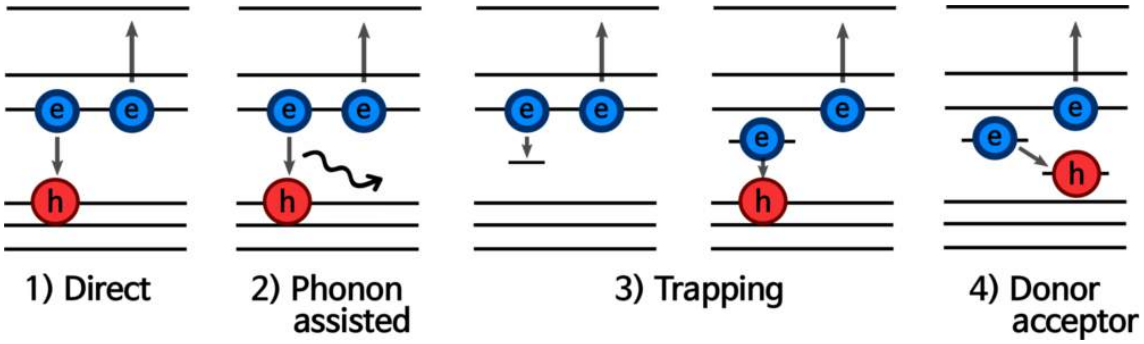

Figure 6.4: Channels for Auger processes. 4 more are available in the case that the hole carries away the energy.

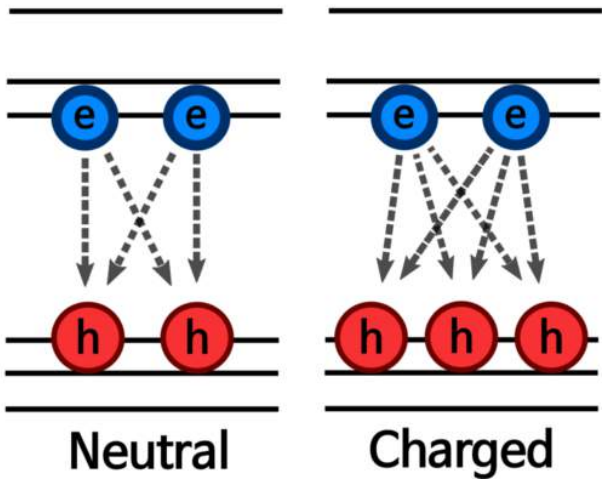

Figure 6.5: Channels for CM. ON the left the case for biexciton with neutral NCs, on the right the case when charged nano particles are involved.

ends up with the creation of two or more electron-hole pairs instead of one: this process is known as carrier multiplication and finds plenty of application in the photo-voltaic technology to increase the power conversion efficiency of solar cells.
It is clear how scintillation could benefit from CM during the relaxation dynamic. A quantitative method to discriminate between the positive CM to the negative AR compares the emission time of the NCs in both single-excitonic (X) and biexcitonic (XX) regime. Using different excitation energy can be used as a method to tune the density of states in the scintillator. Single-excitonic decay time is usually determined under low excitation density whereas incrementing the excitation density will usually generate biexcitons or more AR channels. When high density of state is expected and decay rate enhancement of two orders of magnitude is observed, it is usually related to AR. A spectral shift in the emission wavelength due to the binding energy between multiexcitons and moderate decay rate enhancement are expected for CM.
Decay rate difference in CM generating XX can be explained just using the number of channels available when two electrons in the conduction band interact with two holes in the valence band (Figure 6.5). A factor 4 is characteristic for biexcitonic excitation in neutral quantum dots where the confinement is 3D. When the excitation density increases, the probability of having a charged e-h pair increases and this can lead to an additional shortening in the decay rate. A factor of 6 between single-excitonic and biexcitonic recombination decay times is characteristic of a charged biexciton population.

Being able to identify the processes that are taking place during the recombination mechanism allows tuning those parameters that are known to be influencing the carrier dynamics, such as the geometry of the NC and multiple shells configuration, in order to obtain the desired properties. To conclude, a factor of 100 between biexcitonic and single-excitonic emission is usually accepted as a signal of prominent Auger recombination in the dynamic of the multiexcitonic population while CM is typically related to multiexcitonic enhancement of 4-6 time the origin decay rate. Whenever in NCs compound Auger recombination is recognized a favored process, a part of the electronic charge excited by ionizing radiation is lost and this means loss of information.

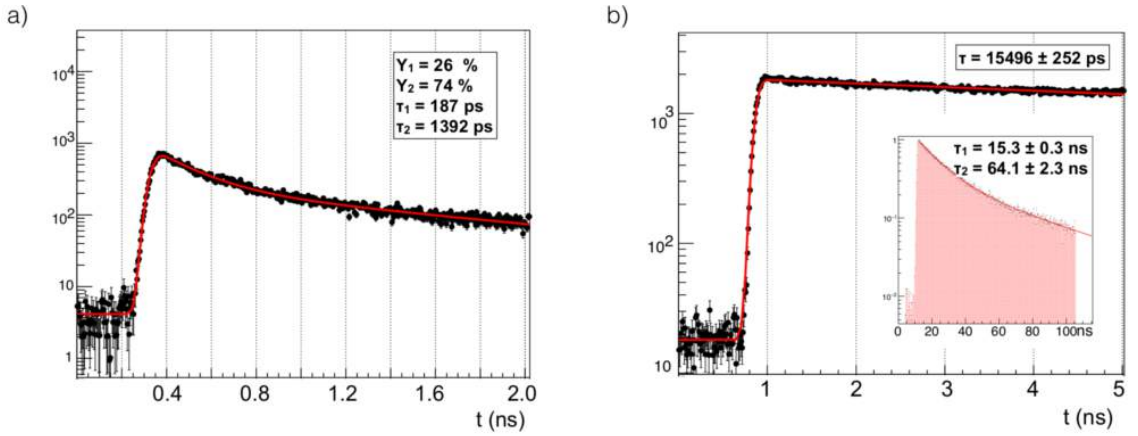

Figure 6.6: Nanocrystals timing performance under pulsed laser excitation. (a) CdSe NPLs. (b)CdSe/CdS GS QDs. The insert in (b) shows the laser excited GS QDs in the 100 ns range.

6.3 NC scintillation properties characterization

Close-packed NC thin films were prepared by sequential drops from toluene solutions onto 100 μm glass coverslips. The CdSe NPL film thickness was roughly 11 μm, determined from the solution concentration, volume deposited, and film area. A comparison between X-rays and laser excitation was performed to verify the presence of bi/multi-exciton state. The acquisition set up was build in order to perform such a comparison with minimal fluctuation in the extracted light collection efficiency (2). Sweeping range, optical slits aperture, and laser settings were chosen to be the same for both the excitation sources, to guarantee the same laser IRF for both sets of measurements. Small sweeping time gates gives better time resolution. A 2 ns gate was therefore chosen to investigate the fast component of the CdSe NPLs emission. GS QDs were instead measured with 5 ns gate because of the slower emission rate.

6.3.1 Laser excitation

An NCs film was deposited on a glass substrate and excited with a 372 nm picosecond laser used to trigger X-rays (see chapter2). Figure 6.6 shows the timing performances of laser-excited NPLs and QDs. The emission from NPLs is consistent with laser excitation studies performed using similar materials in reference [10] and therefore attributed to excitonic emission. The measurements of GS QDs photoluminescence within a 100 ns gate shows two decay components, with lifetimes of 15 ns and 64 ns. These slow and fast components are consistent with the exciton and biexciton emission demonstrated in [2].

6.3.2 X-ray excitation

CdSe nanoplatelets

The streak image in Figure 6.7(a) shows the time-resolved emission spectrum centered at about 530 nm of CdSe NPLs under X-ray excitation. Figure 6.7(c) shows that this spectrum is red-shifted compared to low-intensity laser excitation, which is consistent with biexciton (XX) or multiexciton (MX) emission. Further evidence of XX/MX emission is provided by comparing the X-ray and laser excited emission rates in Figure 6.7(d): the decay time of 520 ps observed for a low-intensity laser is significantly slower than the fast XX/MX emission obtained with 40 keV X-rays.

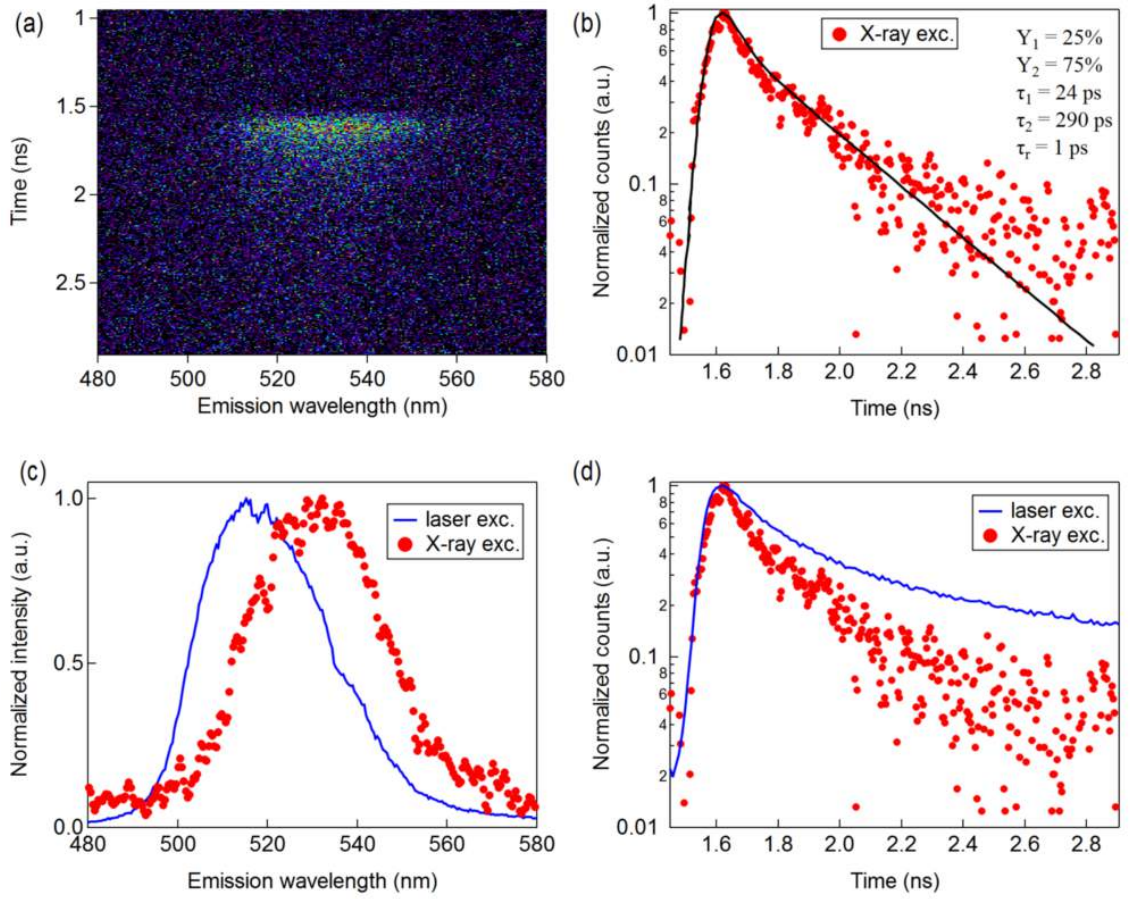

Figure 6.7: X-ray excitation of a CdSe NPL film on glass. (a) Streak image showing the X-ray excited CdSe NPL time-resolved emission spectrum. (b) Spectral integration of the full signal shown in panel (a). (c) X-ray excited spectrum compared to the spectrum obtained under low-intensity laser excitation. Spectra were obtained by temporal integration of the respective streak camera images. A $500\mu m$ spectrometer entrance slit was used in both cases. (d) Comparison of the X-ray and laser excited PL time dynamics. Together, (c) and (d) indicate significant biexciton or multiexciton emission under X-ray excitation.

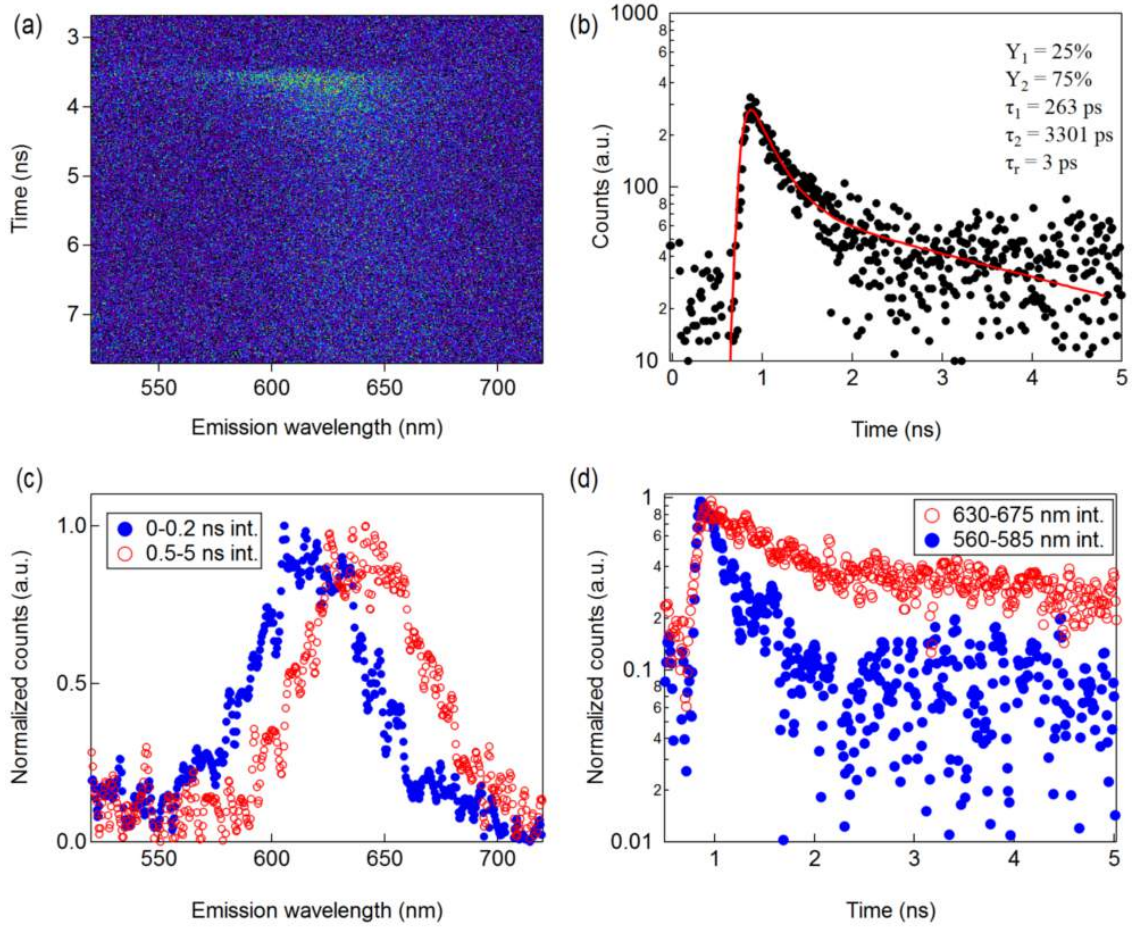

Figure 6.8: X-ray excitation of CdSe/CdS GS QDs film. (a) Streak image showing the GS QDs time-resolved emission spectrum. (b) Spectral integration of the full signal shown in panel (a). (c) Early time (0–0.2 ns) and later time (0.5–5 ns) spectra reveals a blue-shifted spectrum at early times. (d) Spectral integration of narrower slices on the red and blue side of GS QDs emission peak in panel (a). Together, (c) and (d) point toward multiexciton generation under X-ray excitation.

CdSe/CdS giant shell quantum dots

As mentioned above, GS QDs have several features that make them a promising material class for radiation detection. Importantly, the large CdS shell reduces carrier losses due to interaction by passivating traps on the CdSe surface. This results in both high quantum yields and enhanced photostability compared to core-only or thin shell QDs. An undesirable consequence of the CdS shell for the present work is a reduced oscillator strength due to electron delocalization in the CdS shell and hole confinement in the CdSe core. This results in the radiative lifetime increasing with shell thickness [10], and longer lifetimes than CdSe NPLs. Similar to the CdSe NPLs above, the results shown in Figure 6.8 demonstrate faster emission dynamics under X-ray excitation than under low-intensity laser excitation. Possible sources of these faster dynamics can be excited state [37] and MX recombination, both of which are characteristically blue shifted for QDs. Auger recombination in the XX population could also play a role in shortening the lifetime.
The streak image obtained for GS QDs (Figure 6.8(a)) shows faster dynamics occurring on the blue side of the emission spectrum (Figure 6.8(d). The 82 meV blue shift observed in the first could be an evidence of higher order MX generation [14].

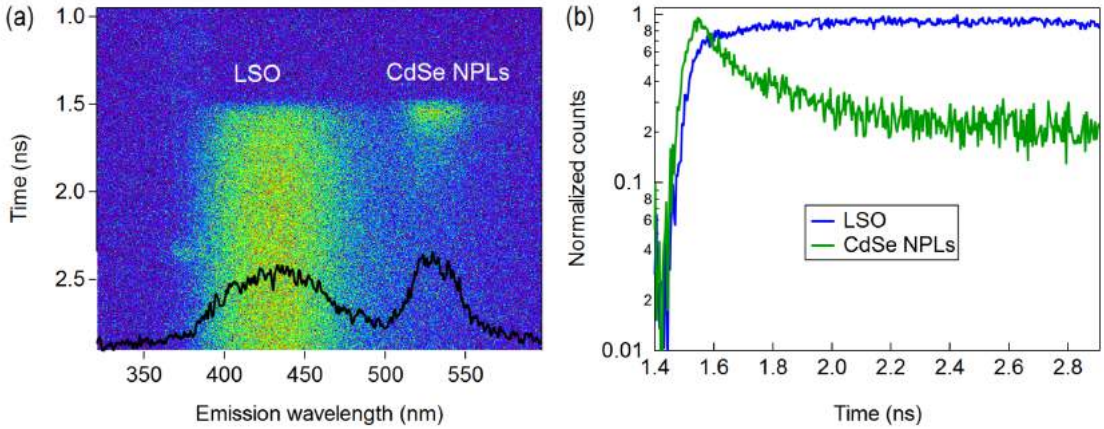

Figure 6.9: X-ray excitation of CdSe NPLs film deposited on a $2 \times 6 \times 8 mm^3$ LSO:Ce scintillating crystal. (a) Spectrally resolved streak image sweeping at 2 ns. (b) Spectral integration of the streak image to yield the decay traces for LSO:Ce and CdSe NPLs. The black line in (a) denotes the time-integrated profile.

6.4 Metamaterial LYSO+NC

It was demonstrated in the previous section that NCs can produce scintillation pulses with very fast rise and decay time. Such a feature cannot be fully exploited by precise timing systems because of the low density and small thickness of NCs materials: the number of gamma rays interacting with the material is low and mostly undergoing Compton effect. For a source of given activity and energy, the number of photons coming from the NCs will be significantly lower than the one coming from the LYSO, therefore the gain obtained from lowering τ_r, τ_d will be degraded. Hereby we investigated the use of CdSe NPL films and GS QD films deposited on the surface of LSO:Ce and LuAG:Ce, respectively. These heterostructures have two different purposes: determining the LY of the NCs by comparing the light output of the two materials and increase the stopping power of the deposition. For dimension of the bulk scintillators small enough (electron mean free path order), the photo-electric events generated in a crystal could share part of the highly energetic electrons created with the NCs layer, effectively increasing the stopping power. Additionally, LYSO generates a high number of slow photons, used for particle discrimination and defining the energy resolution of the system, key parameters for PET and calorimetry applications.

6.4.1 NPLs deposited on LSO:Ce

NPL CdSe NCs were drop cast on one of the larger faces of a $2 \times 6 \times 8 mm^3$ LSO:Ce crystal. X-rays directly excite the NPLs film and the energy that has not been deposited in the NCs then reaches the scintillator along the 2 mm long axis. Light imaged from a $500 \times 100 \mu m^2$ spot is shown in Figure 6.9(a), where ultrafast CdSe NPL emission is seen between 505–550 nm, spectrally shifted from the LSO:Ce photoluminescence (420 nm). The sweeping range was set to 2 ns, which allows us to resolve the first NPL decay component and directly compare to the intrinsic dynamics of NPLs presented in the previous section. A long tail which follows the LSO:Ce decay time characteristics is also present due to LSO:Ce blue light absorbed and re-emitted as green light from the CdSe NPLs. However, the majority of the CdSe NPL emission occurs during the LSO:Ce rise time.

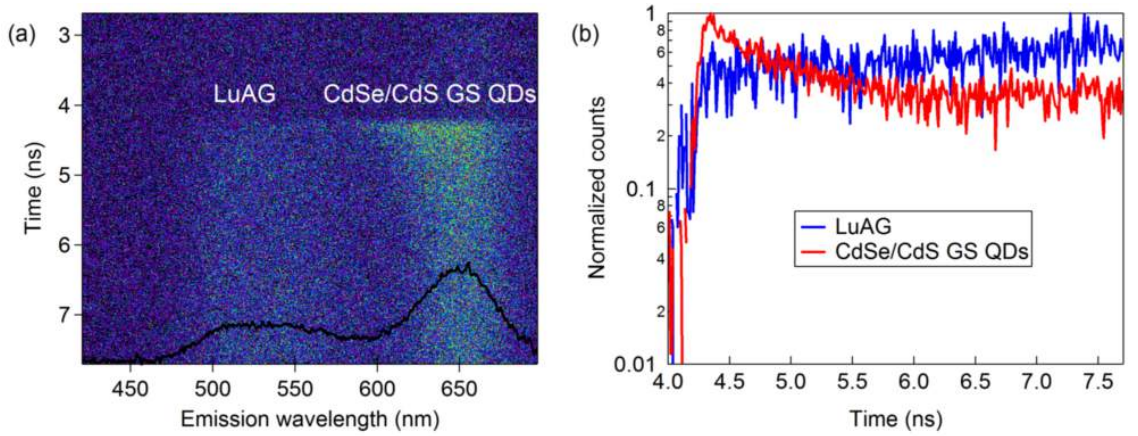

Figure 6.10: X-ray excitation of CdSe/CdS GS QDs film deposited on $1 \times 5 \times 5mm^3$ mm 3 LuAG:Ce scintillating crystal. (a) Spectrally resolved streak image sweeping at 5 ns. (b) Timing performance of LuAG:Ce and GS QDs emission. The black line in (a) denotes the time-integrated profile.

6.4.2 GS QDs deposited on LuAG:Ce

CdSe/CdS GS QDs were drop cast on one of the larger faces of a $1 \times 5 \times 5mm^3$ LuAG:Ce crystal. The film was placed in front of the X-ray tube window and the sample was measured in transmission mode through the 1 mm long axis. The experimental procedure was the same used for NPL on LSO:Ce: light collected from a $500 \times 100\mu m^2$ spot and both scintillation (LuAG:Ce) and ultrafast (QDs) emission are produced, which is shown in Figure 6.10(a). There is a very fast component that occurs during the 500 ps rise time of the LuAG:Ce scintillation and a long tail which can be due to either the slow component seen in CdSe/CdS GS QDs [10], or absorption of LuAG:Ce light which is re-emitted with the typical LuAG:Ce decay characteristics.

6.4.3 Light yield studies

LY estimation was performed for both the crystals using the measurements performed on the heterostructures. Using the well studied LY of the LSO:Ce and LuAG:Ce, we can compare the number of photons collected from both the materials in the same acquisition, which is the integral of the two curves in Figure 6.9(b), for NPLs on LSO, and Figure 6.10, for GS QDs on LuAG. Supposing that the two emission has the same LTE towards the streak camera, a correction is needed in order to compensate for the different energy deposition in NCs and bulk scintillator from X-ray excitation. Geant4 was used to simulate the ratio E_depLSO/E_depNCs, with the NCs layer being 10 μm thick and flat over the entire LSO:Ce face. αNPLs $= 0.1$ is the ratio between the integral of the green and blue curve in Figure 6.9(b), while αGSQD $= 1$ for the curves integral ratio in Figure 6.10. The factors $Y_{200} = 0.61$ and $Y_{300} = 0.23$ are taking into account the amount of photons emitted from the NCs and reabsorbed by the bulk scintillator, from 0 to 200 ps (NPLs) and 300 ps (GS QD) respectively. Considering the LSO intrinsic light yield as 40 000 ph/MeV, the number of photons emitted in the first 1.5 ns is $LY_{LSO} = 1500ph/MeV$. LuAG has an intrinsic light yield of 23 000 ph/MeV [11] which, considering $\tau_(rise) = 535ps$, $\tau_(rise)$ and a double decay component of$\tau_(decay1) = 70ns(44\%)$ and $\tau_(decay2) = 1063ns(56\%)$, has to be reduced to 500 ph/MeV in the acquisition window used. Using the estimated value of $10\mu m$ for the NCs deposition thickness, light yields of 2,500 and 22,000 photons/MeV were calculated for CdSe NPLs and CdSe/CdS GS QDs, respectively.

6.5 Discussion

Both NPLs and GS QD have components in the lower sub-ns region. Under X-ray excitation, these fast components have larger relative amplitudes than under low-intensity laser excitation. Let's define an effective decay time τ_{eff} as the weighted average of the decay components:

$$\tau_{eff} = \frac{\sum_i A_i \tau_i}{\sum_i A_i} \tag{6.12}$$

where A_i are the amplitude of each decay component τ_i. NPLs shows a $\tau_{eff} = 520ps$ with laser excitation and 77 ps with X-ray excitation, with an enhancement of 6.7. [12] shows that, in case of Auger recombination, this enhancement should be ~ 100, which suggests the fast NPLs emission not being dominated by such a phenomena under X-ray excitation.

6.6 Conclusions

NCs were demonstrated to have scintillating properties that could lead to a breakthrough in the field of ionizing particle detectors. Suppressed nonradiative Auger recombination and high Stokes shift were achieved. Both NPLs and GS QDs are a promising approach to fast timing and provide a feasible path toward sub-20 ps time resolution. Future lines of research will be directed toward NCs embedded in a host matrix as proposed in [15], in order to increase the stopping power and the energy transfer efficiency.

Bibliography

[1] S. Gundacker, F. Acerbi, E. Auffray, A. Ferri, A. Gola, M.V. Nemallapudi, G. Paternoster, C. Piemonte, and P. Lecoq. State of the art timing in TOF-PET detectors with LuAG, GAGG, and L(Y)SO scintillators of various sizes coupled to FBK-SiPMs. Journal of Instrumentation, (2016).

[2] J.Q. Grim et al., "Continuous-wave biexciton lasing at room temperature using solution-processed quantum wells", Nature Nanotechnol., 9, 2014, 891.

[3] L.T. Kunneman et al., "Bimolecular auger recombination of electron-hole pairs in two-dimensional cdse and cdse/cdzns core/shell nanoplatelets", J. Phys. Chem. Lett. 4, 2013, 3574.

[4] F.G. Santamaría et al., "Suppressed auger recombination in giant nanocrystals boosts optical gain performance", Nano Lett. 9, 2009, 3482.

[5] F. Meinardi et al., "Large-area luminescent solar concentrators based on stokes-shift-engineered nanocrystals in a mass-polymerized pmma matrix", Nature Phot. 8, 2014, 392.

[6] A. L. Efros, V. A. Kharchenko, and M. Rosen, "Breaking the phonon bottleneck in nanometer quantum dots: role of auger-like processes," Solid State Commun., vol. 93, p. 28184, 1995. 168BIBLIOGRAPHY

[7] V. I. Klimov and D. W. McBranch, "Femtosecond 1p-to-1s electron relaxation in strongly-confined semiconductor nanocrystals," Phys. Rev. Lett, vol. 80, p. 402831, 1998.

[8] P. Guyot-Sionnest, M. Shim, C. Matranga, and M. Hines, "Intraband relaxation in CdSe quantum dots," Phys. Rev. Lett, vol. 60, p. 218184, 1999. Cited on 38

[9] R. D. Schaller and V. I. Klimov, “High efficiency carrier multiplication in PbSe nanocrystals: implications for solar-energy conversion,” Phys. Rev. Lett., vol. 92, p. 186601, 2004.

[10] S. Christodoulou et al., "Synthesis of highly luminescent wurtzite cdse/cds giant-shell nanocrystals using a fast continuous injection route", J. Mater. Chem., C 2, 2014, 3439.

[11] S. Gundacker and et al., "State-of-the-art timing in tof-pet detectors with luag, gagg and l(y)so scintillators of various sites coupled to fbk-sipms.", JINST, 2016, 11, P08008.

[12] C. Dang et al., "Red, green and blue lasing enabled by single-exciton gain in colloidal quantum dot films", Nature Nanotechol., 7, 2012, 335.

[13] M. Achermann, J. A. Hollingsworth, and V. I. Klimov, “Multiexcitons confined within a subexcitonic volume: spectroscopic and dynamical signatures of neutral and charged biexcitons in ultrasmall semiconductor nanocrystals,” Phys Rev. B, vol. 68, p. 245302, 2003.

[14] H. Htoon et al., "Highly emissive multiexcitons in steady-state photoluminescence of individual giant cdse/cds core-shell nanocrystals", Nano Lett., 10, 2010, 2401.

[15] H. Burešová et al., "Preparation and luminescence properties of zno:ga polystyrene composite scintillator", Opt. Express, 24, 2016, 15289.

[16] L.-W. Wang, M. Califano, A. Zunger, and A. Franceschetti, “Pseudopotential theory of Auger processes in CdSe quantum dots,” Phys. Rev. Lett., 91, p. 056404, 2003. [Online]. Available: http://link.aps.org/doi/10.1103/PhysRevLett.91.056404

[17] D. J. Norris, A. Sacra, C. B. Murray, and M. G. Bawendi, “Measurement of the size dependent hole spectrum in CdSe quantum dots,” Phys. Rev. Lett., 72, pp. 2612–2615, Apr 1994. [Online]. Available: http://link.aps.org/doi/10.1103/PhysRevLett.72.2612

[18] V. Kharchenko and M. Rosen, “Auger relaxation processes in semiconductor nanocrystals and quantum wells,” Journal of Luminescence, 70, pp. 158 – 169, 1996. [Online]. Available: http://www.sciencedirect.com/science/article/pii/002223139600052X

[19] V. I. Klimov, A. A. Mikhailovsky, D. W. McBranch, C. A. Leatherdale, and M. G. Bawendi, “Quantization of multiparticle auger rates in semiconductor quantum dots.”, Science, 287, pp. 1011–13, 2010.

7
Conclusions

During this Ph.D., state of the art scintillating materials has been intensively studied with several constraints found regarding their light emission, optical properties, and chemical stability. Different characterization benches were developed specifically for the measurements presented and extensive work has been dedicated to fine tune the simulations framework describing scintillator, photo-detector, and PhC. The method refined using this useful tools was validated on several samples and will be the starting point for future analysis.
Classical approaches to boost inorganic scintillator detection were found to be already at a good trade-off between performances and costs, in most of the applications. During these preliminary studies, some other interesting observations were made. Scintillators performances were measured to be sensitive to the geometry of the crystal, specifically higher aspect ratio (height/read-out face) results in a worsen energy resolution and lower light yield. Lower aspect ratio suffers from lower sensitivity, which makes them not the best choice for fast measurements. New scintillating material $R\&D$ offers high potential improvements but is demanding in terms of optimization time and equipment. The many parameters governing material quality and scintillating properties put this research line beyond the scope of a Ph.D. in physics. Nevertheless, preliminary tests were performed in collaboration with the University of Prague showed how a new halide such as Cs_2HfCl_6 offers powerful scintillating properties with a high level of homogeneity without the major drawback of hygroscopicity. Last, optical coupling was found to be optimal for RI equal to the lower RI optical media in the detection chain. In the specific case of SiPM, this is the glass protective layer above the Silicon surface. Several unsuccessful tests were performed on a modified version of SiPM without the glass layer, affected by the presence of an additional passivating layer of few micron thicknesses and lower RI. Further work will be pursued on this research line, with further modified SiPM without passivating layer.
To boost scintillation detection a shift in paradigm was needed, moving away from classical ray tracing concepts and basic scintillation mechanism. This Ph.D. work explored the use of diffraction and quantum dots to break the limit of critical angle and classical band gap recombination, respectively.
PhC were used to create diffraction on the readout face of inorganic scintillators, which showed promising results from the point of view the crystal's time and energy resolution. The potential gain will always be limited by the overall performances of the original scintillation process since the energy resolution will be worse than the statistical component of the intrinsic LY: PhC increases only the collection efficiency. Nevertheless, a maximum LY gain of 1.63 and energy resolution gain of 0.79 was obtained for a non wrapped and optically coupled crystal, while in a configuration where optical agent between the photodetector and the crystal was required and with optimized Teflon wrapping, an LY gain of 1.43 and energy resolution gain of 0.87 were demonstrated.
During this thesis, the PhC technology was tested on a medical imaging system, with limited benefits demonstrated. This was mainly due to the difficulties in finding a suitable production process for large area patterning and to the modification needed from the reconstruction side to cope with the modified angular distribution

of the extracted photons. Nonetheless, future work with a more profound level of integration and ameliorated knowledge of the technology could lead to the high-performance gain with more reproducible production.
NCs are instead brand new materials that could bring a real break-through in the field of ionizing particle detectors. Both NPLs and GS QDs were found to be promising material to approach fast timing toward sub-20 ps coincidence time resolution. The decay time of CdSe NPLs under X-ray excitation was measured to be as low as 24 ps for the fast component and 290 ps for the slow component. The decay time of GS QDs under X-ray excitation was measured to be higher, 263 ps and 3301 ps for the slow and fast component respectively, but showing the higher intensity of the signal due to the higher density of active material, which place it closer to the application end.
Future lines of research will be directed toward NCs embedded in a host matrix as proposed in [15], in order to increase the stopping power and the energy transfer efficiency.